# Oxygen Ordering and Superconductivity in the High Tc Superconductor YBa2Cu306+x

**Poulsen, Henning Friis**

*Publication date:*
1991

*Document Version*
Publisher's PDF, also known as Version of record

RISØ

Risø-R-608(EN)

# Oxygen Ordering and Superconductivity in the High $T_c$ Superconductor $YBa_2Cu_3O_{6+x}$

Henning Friis Poulsen

Risø National Laboratory, Roskilde, Denmark
December 1991

# Oxygen Ordering and Superconductivity in the High $T_c$ Superconductor $YBa_2Cu_3O_{6+x}$

Risø-R-608(EN)

**Henning Friis Poulsen**

**Risø National Laboratory, Roskilde, Denmark**
**December 1991**

This report is submitted in partial fulfilment of the requirements for a Ph.D. degree at the University of Copenhagen. The supervisors were Dr. N.H. Andersen and Dr. M. Nielsen at Risø National Laboratory and Dr. P. Hedegård at the University of Copenhagen.

ISBN 87-550-1787-8
ISSN 0106-2840

Grafisk Service · Risø · 1992

## 0.1 Abstract

This report contains the result of an experimental and theoretical investigation of the oxygen ordering process in the High $T_c$ superconductor $YBa_2Cu_3O_{6+x}$. It falls in two parts.

Firstly, a series of 350 simultaneous structural and thermodynamic measurements are performed as function of temperature and oxygen stoichiometry on an equilibrated powder sample. Neutron scattering on a powder diffractometer is used in connection with *in situ* monitoring in a gas-volumetric equipment of the oxygen in-diffusion. Information on the variations of the structural phases, the twin domain sizes, the elastic forces, the chemical potential of oxygen as well as diffusion is provided. Using Monte Carlo simulations we find that a simple two-dimensional lattice gas model of the oxygen ordering process, the ASYNNNI model, gives an excellent description of the vast majority of these data. Adopted values for the interaction parameters in the model are $V_1 = -4180$ K, $V_2 = 2510$ K and $V_3 = -360$ K. The internal strain is shown to increase linearly with oxygen concentration in the ordered Ortho-I phase. During slow cooling the size of the twin domains are found to freeze shortly after passing the order/disorder phase transition, with average values that depend on the pertinent structural phase. Based on this information a discussion of the influence of the elastic forces on the low temperature ordering process is given. The in-diffusion process is at high and intermediate temperatures governed by the bulk kinetics, with resulting Arrhenius behaviour. We provide evidence that nearest neighbor hopping is the relevant oxygen hopping range, leading to metastability and freezing at low temperatures.

Secondly, a systematic study of the relationship between the static and dynamic variations of the superconducting transition temperature, $T_c$, and the corresponding variations of the low temperature oxygen ordering process is performed. Statistics from Monte Carlo simulations based on the ASYNNNI model are combined with experimental data from the literature. Applying the available data at $x = 0.41$, the dynamics of both the oxygen ordering and $T_c$ are found to be governed by algebraic growth laws, with $T_c$ growing in proportion to the area of the Ortho-II domains. The combined static and dynamic analysis make it evident that within a charge transfer model, a linear $T_c$ versus charge transfer relationship can only be rationalized if the description is based on extended coherent ordered domains and if the dynamic co-existence between the Ortho-I and the Ortho-II type of domains inherent to the ASYNNNI model is taken into account. A minimal model is proposed, where the total charge transfer is found as a weighted sum over the areas of the Ortho-I and the Ortho-II domains, and the minimal size of the two types of domains is given by a doubling of their unit cells in both directions. Good agreement with the experimental set of data is achieved.

## 0.2 Dansk resume

Denne rapport indeholder resultatet af en eksperimentel og teoretisk undersøgelse af ilt ordningsprocessen i den keramiske superleder $YBa_2Cu_3O_{6+x}$. Rapporten falder i to dele.

For det første er der gennemført en serie på 350 sæt af strukturelle og termodynamiske målinger som funktion af temperatur og iltstøkiometri på et equilibreret pulver sample. Et pulver neutron-diffraktometer er anvendt med *in situ* registrering af den makroskopiske iltoptagelse via et gasvolumetrisk udstyr. Der opnås information om variationen af de strukturelle faser, størrelserne på tvillingedomæner, de elastiske kræfter, det kemiske potential af ilt samt om diffusionsegenskaberne af materialet. Udfra Monte Carlo simuleringer finder vi, at en simpel todimensional gittergas model for ordningsprocessen, ASYNNNI modellen, giver en udmærket beskrivelse af langt hovedparten af disse data. Udfra et fit findes vekselvirkningsparametrene i modellen til $V_1 = -4180$ K, $V_2 = 2510$ K og $V_3 = -360$ K. Deformationen af materialet vises at vokse lineært med ilt koncentrationen i den ordnede Ortho-I fase. Under langsom nedkøling indefryses størrelsen af tvillinge-domænerne kort efter passagen af orden/uordens faseovergangen med en gennemsnitsværdi der afhænger af hvilken ordnet fase der er tale om. Udfra disse oplysninger diskuteres indflydelsen af de elastiske kræfter på ilt ordningsprocessen ved lave temperaturer. Optagelsen af ilt er ved høje og mellemliggende temperaturer bestemt af bulk diffusiviteten, med Arrhenius opførsel til følge. Nærmeste nabo-hop vises at være den relevante mekanisme for mikro-kinetikken. Lav temperatur opførslen er følgelig præget af meta-stabilitet og indefrysninger.

For det andet er der gennemført et systematisk studie af sammenhængen mellem de statiske og de dynamiske variationer af den superledende overgangstemperatur, $T_c$, og de tilsvarende variationer af ilt ordningsprocessen ved lave temperaturer. Statistik fra Monte Carlo simuleringer af ASYNNNI modellen er kombineret med brug af eksperimentelle data fra litteraturen. For de kendte data ved $x = 0.41$, finder vi at både iltkinetikken og $T_c$ data'ene opfylder algebraiske vækstlove, med $T_c$ voksende proportionalt med arealet af Ortho-II domænerne. Den kombinerede statiske og dynamiske analyse gør det klart, at en lineær model for sammenhængen mellem ladningsoverførsel og $T_c$ kun er forenelig med ASYNNNI modellen, såfremt beskrivelsen baseres på koherænte ordnede domæner, og den indbyggede dynamiske sameksistens mellem Ortho-I og Ortho-II type domæner tages i betragtning. Der opstilles en fænomenologisk minimal-model, hvor ladningsoverførslen findes som en vægtet sum af arealerne af Ortho-I og Ortho-II domænerne, og den minimale størrelse af disse to typer af iltdomæner er givet ved en fordobling af de respektive enhedsceller i begge retninger. En god overenstemmelse med de eksperimentele data opnås.

# Contents

# 1 Introduction

The unexpected discovery of superconductivity in copper-oxide Perovskites in 1986 [1] has lead to an unprecedented burst in scientific activity within condensed matter physics. At present, the superconducting pairing mechanism remains elusive and the normal state properties of these materials have sent the theoreticians searching for a general formalism to describe the physics of strongly correlated electrons. From an experimental point of view there are several reasons that a high priority should be given to detailed structural studies, especially on the nano-scale properties. Firstly, there is the intriguing possibility of a direct coupling to the crystalline lattice. Here, evidence from pressure, thermal conductivity, ultrasound, NQR-measurements and femto-second spectroscopy points towards lattice anomalies around the superconducting transition temperature $T_c$ (see e.g. the review by Ranninger [2]). It should be mentioned that such observations - apart from being not universally accepted - do not preclude that the pairing mechanism may be partly or predominantly caused by strong electron correlations, which without any doubt are present. Secondly, the superconducting properties have been found to depend in a crucial way on the introduction of structural defects and the arrangements of such defects. Also the internal strain, which may be elucidated by structural probes, is of importance. Finally, structural measurements remain the best source of information on the electrostatics of the materials, most notably on the number of electronic holes in the $CuO_2$ layers, the commmon structural feature of all the compounds believed to be the source of the superconductivity. $T_c$ is widely believed to depend drastically on this number.

The most intensely studied of the copper-oxides is the layered compound $YBa_2Cu_3O_{6+x}$, which comprises a $CuO_2$ bilayer, and a $CuO_x$ layer which exhibits a large ability for intercalating oxygens (the parameter $x$ can be varied between 0 and 1). In many ways this compound constitutes a unique material for investigating the relationship between structure and electronic properties. Thus, the low temperature structural phase diagram is richer than for the other compounds, and at the same time the $T_c = T_c(x)$ behaviour exhibits additional features in terms of what is known as the plateau-behaviour. Perhaps more important, in the present case we have direct experimental evidence, that $T_c$ is correlated not only with the average oxygen stoichiometry - the value of $x$ - but with the configuration of oxygens in the $CuO_x$ plane [3], [4]. Thus, samples with identical average oxygen concentrations but different local configurations may deviate by as much as 30 K in transition temperature. This observation makes it relevant to correlate the electronic properties not only with information on the average structural properties, but also with the thermodynamics of the oxygen ordering process in the material.

The oxygen ordering process in $YBa_2Cu_3O_{6+x}$ is further known to give rise to a rich structural phase diagram, which to a very good approximation is two dimensional in nature. The description of the thermodynamics of this process is an interesting example of low dimensional physics, which deserves attention in its own right.

The object of the work presented in this report is to investigate the ordering process of oxygens in $YBa_2Cu_3O_{6+x}$ and relate the resulting instantaneous oxygen configurations to the superconducting properties of the material. A close combination of experimental studies (neutron diffraction and thermodynamic measurements) and theoretical studies, mostly Monte Carlo simulations, is intended.

The outline is as follows: in chapter 2 most of the background material is contained. This includes a listing of the basic properties of $YBa_2Cu_3O_{6+x}$ aimed at the reader unfamiliar with this subject. Next a review of the experimental and theoretical work on the structural phase diagram is given. Emphasis has been put

on a presentation of the details of a simple anisotropic lattice gas model of the oxygen ordering known as the ASYNNNI model. The review is not intended to be complete. Next a short introduction to Monte Carlo simulation technique in general is presented, with examples relevant to the case of the ASYNNNI lattice gas model. Finally a very short review of the physics of growth processes is included - relevant for simulations presented in chapter 4.

Chapter 3 contains our work on the structural phase diagram and the thermodynamics of oxygen ordering. First the experimental technique (neutron diffraction combined with gas-volumetric measurements) is introduced and the experimental results on equilibrium as well as dynamic properties presented. Next, these results are discussed in relation to the ASYNNNI model using Monte Carlo simulations. A few additional experimental results from the literature are included in order to achieve more general conclusions. Also, some theoretical work on how to treat the internal strain degrees of freedom is presented and related to our experiments.

Chapter 4 contains a discussion of the relation between structure, strain, charge transfer and superconductivity in $YBa_2Cu_3O_{6+x}$. First some relevant experiments are discussed and the concept of a linear charge transfer model introduced. Next, a systematic Monte Carlo simulation study of the equilibrium features of the ASYNNNI model allows us to set strong constraints on the nature of a linear charge transfer model. In the following section a corresponding simulation study of the dynamic features of the ASYNNNI model is performed. Based on a reanalysis of experimental data from the literature a rather fundamental relation between the time-evolution of structural and superconducting properties is revealed. Finally, in the discussion part we demonstrate how the static and dynamic information merge to give a coherent picture of the charge transfer process.

Standard notation is used throughout. The one exception is the critical temperature for the structural phase transition between tetragonal and orthorhombic symmetry, which we denote $T_\phi$, in order to distinguish it from the superconducting critical temperature, $T_c$.

The thesis is based on research work reported in the scientific papers listed below.

1. *The Structural Phase Diagram and Oxygen Equilibrium Partial Pressure of $YBa_2Cu_3O_{6+x}$ Studied by Neutron Powder Diffraction and Gas Volumetry.* N.H. Andersen, B. Lebech and H.F. Poulsen. Physica C 172 (1991), 31-42.

2. *Twin Domain Size and Bulk Oxygen In-diffusion Kinetics of $YBa_2Cu_3O_{6+x}$ Studied by Neutron Powder Diffraction and Gas Volumetry.* H.F. Poulsen, N. H. Andersen and B. Lebech, Physica C 173 (1991), 387-398.

3. *Dynamical Scaling of Oxygen Ordering in $YBa_2Cu_3O_{6+x}$.* H.F. Poulsen, N. H. Andersen, J.V. Andersen, H. Bohr and O.G. Mouritsen, Phys. Rev. Lett. 66 (1991), 465-468.

4. *Relation between Superconducting Transition Temperature and Oxygen Ordering in $YBa_2Cu_3O_{6+x}$.* H.F. Poulsen, N.H. Andersen, J.V. Andersen, H. Bohr and O.G. Mouritsen, Nature 349 (1991), 594-596.

5. *Lattice Gas Simulation of Oxygen Ordering in $YBa_2Cu_3O_{6+x}$ showing Dynamical Scaling.* H.F. Poulsen, N. H. Andersen, J.V. Andersen, H Bohr and O.G. Mouritsen, Modern Physics Lett. B 5 (1991), 827-832.

6. *Structural Phase Diagram and Equilibrium Oxygen Partial Pressure of $YBa_2Cu_3O_{6+x}$.* N.H. Andersen, B. Lebech and H.F. Poulsen, J. Less-Common Metals 164-165 (1990), 124-131.

7. ***Study of Structural Phase Diagram, Oxygen Bulk In-Diffusion, and Equilibrium Partial Pressure of*** $YBa_2Cu_3O_{6+x}$. N.H. Andersen, B. Lebech and H.F. Poulsen, Proc. of the 3rd International Symposium on Superconductivity (ISS '90) November 6-9 1990, Sendai, Springer-Verlag Tokyo 1991. 124-131.

8. ***Oxidation Kinetics in Oxygen Deficient*** $YBa_2Cu_3O_{6+x}$ ***Studied by Neutron Powder Diffraction***. J. Als-Nielsen, N.H. Andersen, C. Broholm, K.N. Clausen, B. Lebech, M. Nielsen and H.F. Poulsen. IEEE Transactions on Magnetics 25 (1989), 2254-2261.

9. ***Computer Simulation of Phase Separation and Ordering in Low-dimensional Systems***. O.G. Mouritsen, P.J. Shah, J.V. Andersen, H.F. Poulsen and H. Bohr, Phys. Scr. (in press).

10. ***Antiferromagnetism and Metallic Conductivity in*** $Nb_{12}O_{29}$. R.J. Cava, B. Batlogg, J.J. Krajewski, P. Gammel, H.F. Poulsen, W.F. Peck and L.W. Rupp Jr., Nature 350 (1991), 598-600.

11. ***Electronic and Magnetic Properties of*** $Nb_2O_{5-x}$ ***Crystallographic Shear Structures***. R.J. Cava, B. Batlogg, J.J. Krajewski, P. Gammel, H.F. Poulsen, W.F. Peck and L.W. Rupp Jr., Phys. Rev. B 44, 13 (1991) 6973-6981.

12. ***Oxygen Ordering and Superconductivity in Co-substituted*** $YBa_2Cu_3O_{6+x}$. J.V. Andersen, H.F. Poulsen, N. H. Andersen, and O.G. Mouritsen. Preprint.

13. ***Monte Carlo Simulations of the Ortho-II Structure Factor of the Oxygen Ordering Process in*** $YBa_2Cu_3O_{6+x}$. J.V. Andersen, H.F. Poulsen, N. H. Andersen, and O.G. Mouritsen, Preprint.

# 2 Background

## 2.1 Basic Properties

The copper oxide superconductors may structurally be characterized as layered Perovskites, with a stacking sequence consisting of $CuO_2$ planes alternating with rock-salt layers that have intrinsic defects. The structure of $YBa_2Cu_3O_{6+x}$ (YBCO) is shown in Fig. 1. A bilayer consisting of two $CuO_2$ planes separated by yttrium atoms is stacked on top of a block comprising a sequence of $BaO$, $CuO_x$ and $BaO$ layers. The copper site in the bilayers has a rather unusual fivefold coordination, with nearest neighbors positioned in a square pyramid. The standard way of indexing the various sites, due to Jorgensen et al. [5], is indicated at the figure. The oxygen site O(4) positioned at the apex of this pyramid is known as the apical oxygen. Likewise, the $CuO_x$ mirror-plane containing the O(1), O(5) and Cu(1) sites, shown arbitrarily at the base of the unit cell, is known as the basal plane.

One major difference between YBCO and nearly all other copper oxide superconductors is the way the defects are introduced. Normally, this is done by substituting cations when synthesizing the material, e.g. in $La_{2-x}Sr_xCuO_4$, where $Sr^{2+}$ ions substitute $La^{3+}$. In the case of YBCO, vacancies on the oxygen O(1) and O(5) sites constitute the defects. The corresponding variation in oxygen stoichiometry is rather large: $0 < x < 1$. During synthesis the O(1) and O(5) sites are depleted, and oxygen has to be intercalated by an oxidation process afterwards. In equilibrium, at high temperatures and for low oxygen partial pressures in the environment $x \approx 0$, while for low temperatures and high partial pressures $x \approx 1$.

Varying the temperature T and the partial pressure P of oxygen in the environment one can map out the stable structural phases as function of $x$ and T. The resulting structural phase diagram, has turned out to be very rich and rewarding to study. The main feature is the existence of a tetragonal phase at high temperatures and low $x$-values, and a series of orthorhombic phases at low temperatures and high $x$-values. A schematic representation of the variation with $x$ and T of the transition temperature $T_\phi$ for the transition between the two symmetry groups is shown in Fig. 2. Studying the phase diagram has proven to be experimentally demanding, due to slow kinetics of the oxidation process at low temperatures, where some of the most interesting phenomena take place.

YBCO exhibits dramatic variations in its electric and magnetic properties as function of oxygen concentration. For $x \lesssim 0.3$ the material is an antiferromagnetic semiconductor, with a Neel temperature of 415 K for $x = 0$. At higher oxygen concentrations the material becomes metallic, and superconducting for low temperatures. The superconducting transition temperature, $T_c$, rises with increasing oxygen concentration, reaching a maximum of 93 K at $x = 1$, but exhibits important additional features in terms of what is known as the plateau-behaviour. Thus $T_c$ is approximately constant for $0.85 < x < 1.0$ ($T_c \approx 90$ K), followed by a smooth decrease to another constant value between $x = 0.65$ and $x = 0.45$ ($T_c \approx 60$ K), and a final decrease to 0K in the vicinity of the tetragonal to orthorhombic phase transition. The (rather diffuse) transition between the semiconducting and the metallic regime is known as the metal/insulator transition. A schematic representation of the electronic properties as function of temperature and oxygen stoichiometry $x$ is shown in Fig. 2.

The electronic properties of both the superconducting and the normal metallic state in the copper oxide superconductors are highly unusual. Thus, the resistivity is linear in the temperature while the Hall coefficient exhibits an anomalous temperature dependency with changes in its sign and slope depending on the direction of the external field [6]. Among the exotic properties of the superconducting state

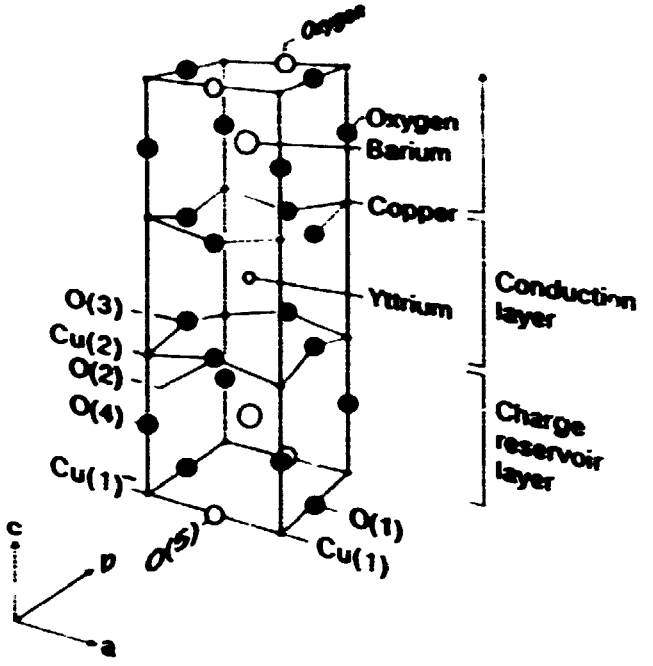


*Figure 1. The $YBa_2Cu_3O_{6+x}$ unit cell. The layered Perovskite structure with consecutive layers of $CuO_x - BaO - CuO_2 - Y - CuO_2 - BaO$ is displayed. The oxygen content in the O(1)-O(5) lattice is variable: $0 < x < 1$. Within the framework of charge transfer models, the superconducting pairs are basically confined to the $CuO_2$ planes, while the rest of the structure serves as a charge reservoir.*

are unprecedented high critical temperatures and very small coherence lengths. At present no consensus has been reached, concerning the theoretical description of these phenomena. Among other things, it is still debated whether the superconducting pairing mechanism is due to strong electron correlation effects and/or the lattice plays a crucial part.

It is known from spectroscopy that superconductivity occurs predominantly in the $CuO_2$ planes of the copper oxides. These are intrinsic insulators. Thus, a natural model that arises from the common structural features of the copper oxides is that the role of the rock-salt layers is to provide carriers for the $CuO_2$ bilayers. Based on this hypothesis, it is instructive to view the YBCO unit cell as consisting of conduction layers (the $CuO_2$ layers) and charge reservoir layers, cf. Fig. 1. The cations Y and Ba can be treated as classical 3+ and 2+ ions, respectively. Speaking in terms of formal valences, the only variable valences are then the Cu(1) and Cu(2) valences. Thus, from charge conservation, knowing one we can infer the other. In the language of formal valences it is therefore meaningful to talk of charge being transferred from the reservoir to the conduction layer. In the present case, increasing the oxygen content, different structural phases appears with different local configurations for the Cu(1) copper. It is now natural to try to establish a model that relates the local configuration of Cu(1) (the thermodynamics of the oxygen ordering) to an effective transfer of charge to the $CuO_2$ planes. Such models has come to be known as charge-transfer models [7].

Using formal valences is probably a misconception, because it conceals the effect of the apical oxygen. However, it is still relevant to ask the question if - as a first order approximation - we may decouple structure (thermodynamics of oxygen ordering) from e.g. superconductivity by claiming that the thermodynamics

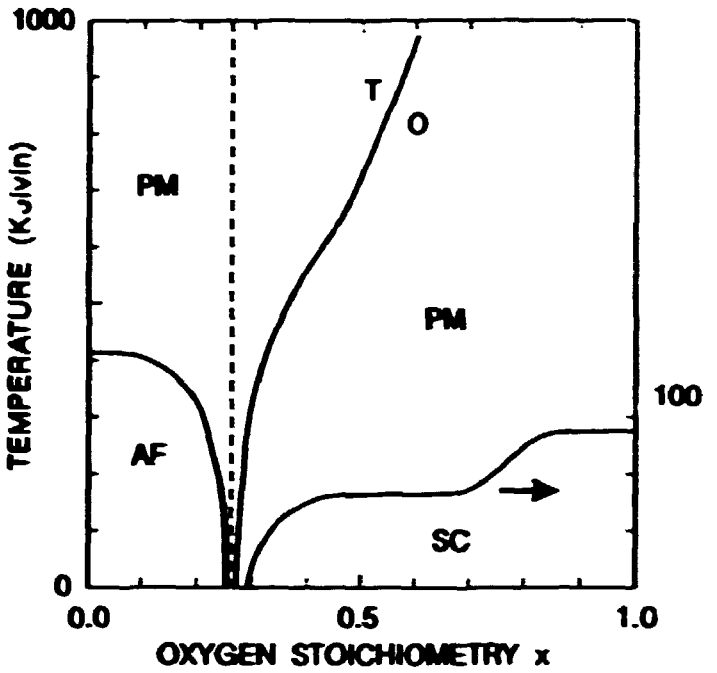


*Figure 2. Schematic representation of the variations in structural symmetry and electromagnetic properties as function of temperature and oxygen stoichiometry x. (AF), (PM) and (SC) refer to antiferromagnetic, paramagnetic and superconducting behaviour, respectively. The dotted line marks the transition between semiconducting (low x-values) and metallic behaviour (high x-values) of the resistivity. The symbols (T) and (O) for tetragonal and orthorhombic symmetry, respectively, are placed next to the structural phase transition line. The metal-insulator transition is poorly defined, and the low temperature relation between structural and electronic states are still debated. To make the superconducting state clearly visible the superconducting transition temperature $T_c$ has been multiplied by 3 throughout.*

only determines the amount of charge transferred to the $CuO_2$ planes, and the superconducting properties in turn are simply determined by the charge in the $CuO_2$ planes and features intrinsic to these planes. There are many reasons why such a picture could fail, most notably the charge reservoir layer might participate directly in the pairing mechanism in case of e.g. a coupling to the lattice. Moreover, the structure might be speculated to give rise to some special symmetry or internal strain needed for an in-plane coupling mechanism to take place.

Finally, the layered structure of the material should be noticed. Huge anisotropies are found in resistivity data, where the in-plane conduction has a metallic character, while conduction along the c-axis gives rise to semiconducting like behaviour. Likewise, the superconducting coherence length is highly dependent on direction, with a coherence length along the c-axis that is comparable to or below the repeat distance of the unit cell in that direction. Structurally, Rothman et al. [8] report that the in-plane components and the c-axis component of the oxygen diffusivity tensor differ by six orders of magnitude. Also, as will be argued in this thesis the distance between two consecutive basal planes is too large for any inter-plane oxygen-oxygen Coulombic repulsion to be of importance. For all practical purposes this means that the thermodynamics of the oxygen ordering process is a 2-D phenomenon (the three dimensional registry of some of the ordered phases are due solely to the interplay of the internal strain). The combination of this structural

anisotropy with the similar anisotropy in the electronic properties makes YBCO an interesting candidate for studies of physics in lower dimensions.

## 2.2 Review of the Structural Phase Diagram: Experimental

The structural properties of $YBa_2Cu_3O_{6+x}$ are to a first approximation determined by the wide range in oxygen stoichiometry $0 < x < 1$, that can be achieved in a reversible manner by varying the temperature T and the partial pressure P of oxygen in the environment. Early on it was found by Jorgensen and coworkers [5] in a powder neutron diffraction study, that the oxygen non-stoichiometry is associated with the oxygen O(1) and O(5) sites. Slight deviations from the ideal site occupancy of 1 were also found for the apical oxygen site, O(4). However, structurally refining this site is known to be troublesome, possibly due to the existence of a split site, and the reported values of the site occupancies, $n = n(O(4))$, are consistent with 1 except from the interval $0.28 < x < 0.45$ with a possible minimum of $n = 0.95(2)$ at $x \approx 0.28$ [9]. Accordingly, we will neglect this effect in the following[1]. The oxygen concentration also determines the stability range of the perovskite structure. Under high pressures the material is unstable towards formation of the superconducting perovskites $YBa_2Cu_{3.5}O_{7+x}$ and $YBa_2Cu_4O_8$ [10]. Likewise, the structure decomposes below a critical pressure, that is approximately $10^{-3}$ atm at 800 °C and $10^{-7}$ atm at 550 °C [11].

The compound exhibits two structural phases at high temperatures: a tetragonal phase for small $x$-values and an orthorhombic one for large $x$-values [12]. The corresponding space groups are $Pmmm$ and $P4/mmm$, respectively [5]. The orthorhombic phase is also known as the Ortho-I phase. At the stoichiometric composition for the Ortho-I phase $x = 1.0$, the oxygen configuration in the basal plane consists of oxygen chains parallel to the b-axis situated on the O(1) sites, while all the O(5) sites are depleted. As oxygens from the O(1) sites are removed - lowering the $x$-value - the degree of ordering is also reduced with a finite number of oxygens moving to the O(5) sites. Eventually, when the remaining oxygen atoms become equally distributed between the two sites, the structure transforms from orthorhombic to tetragonal. This generally accepted idea of an order/disorder transformation was originally motivated by the experimental study by Jorgensen et al. [5].

The phase transformation is accompanied by the creation of twin domains in the orthorhombic phase. Thus the transition may be initiated by entropic forces, but in the final stages of the process the elastic forces are predominant, creating a regular tweed pattern of domains tilted 90° towards each other. The dynamical description of the formation of the twin domains have turned out from experiments to be far from trivial, but the subject is outside the scope of the present thesis[2].

The equal site-occupancies in the tetragonal phase does not imply a random distribution of the oxygens on a local scale. In fact, local probes of symmetry - perturbed angular correlation studies [13] - indicates that the Cu(1) site remains in an anisotropic field for all values of $x$, at least at high temperatures. Thus, the oxygens seemingly remain ordered locally in chain-fragments along either the a- or the b-axis, throughout the tetragonal phase. The orthorhombic distortion building up in connection with such local anisotropy will be very small, and the

[1] The effect of deviations from full stoichiometry at the apical site would arguably be very important, if the oxygen diffusion process involved jumps to vacant positions at the apical site. But, this is not the conventional view of the workings of the micro-kinetics.

[2] The process of twin domain formation will play a crucial part in some of the discussions in chapter 3, but the elastic forces will be treated in a way that leaves most experimental details irrelevant.

material appears tetragonal on the scale of the probes.

At low temperature many additional phases have been observed as faint superstructures, using transmission electron microscopy (TEM) techniques. However, with one exception - the Ortho-II phase - the stability of the phases is still debated. The oxygen kinetics is very slow at the relevant temperature of 300 K. In fact, it has been proven, that the diffusivity at room temperature is too slow to allow for any global diffusion from the surfaces to be detected (the stoichiometry $x$ being constant over weeks), while local re-arrangements of oxygens may take place [4]. Hence, measurements are generally performed on out-of-equilibrium samples, with resulting problems of sample dependency and irreversibility. Also, despite many attempts most of the additional phases have not been probed by neutron nor X-ray diffraction techniques.

The evidence in favour of the stability of the Ortho-II phase is now overwhelming. One argument in terms of thermodynamic measurements will be given in the present thesis. Furthermore, Flemming et al. [14] have been able to probe the structure by X-ray diffraction, and very recently Zeiske et al. [15] provided a neutron diffraction identification. The Ortho-II structure has orthorhombic symmetry, and - analogous to the Ortho-I structure - it can be described in terms of chains of oxygens parallel to the b-axis. In this case every second of the O(1) chains is filled, while all O(5) sites are empty, leading to a stoichiometric compound at $x = 0.5$. The X-ray study by Flemming reported on diffuse peaks centered at $(\frac{1}{2}, 0, 0)$ in a quenched crystal. By calibrating their lattice parameters to our lattice parameter vs. oxygen concentration results (see chapter 3), the stoichiometry of the sample in question is found to be $x = 0.58(5)$. The width of the peaks yielded coherence lengths of 21, 16, and 9 Å in the $a, b$, and $c$ directions, respectively. Thus, the domains formed were scarcely larger than a single Ortho-II unit cell. In contrast, the crystal used by Zeiske and coworkers was oxidized by stepwise cooling from 650 °C to 150 °C in 200 hours, followed by long-time annealing (400 h) at 150 °C. The correlation lengths derived were 40, 90 and 22 Å, relative to the $a, b$, and $c$-axes, respectively. The oxygen content was again derived from the lattice parameters: $x = 0.40(5)$.

Recently Sonntag et al. [16] also reported on the detection by neutrons of a structural phase at the concentration $x = 0.35(5)$ with super lattice peaks positioned at $(\frac{1}{2}, \frac{1}{2}, 0), (\frac{1}{4}, \frac{3}{4}, 0), (\frac{1}{2}, \frac{3}{2}, 0)$ and $(\frac{3}{2}, \frac{3}{2}, 0)$. The authors proposed a tetragonal $2\sqrt{2}a \times 2\sqrt{2}b \times c$ structure, but afterwards it has been pointed out by several e.g. [44] that their data are more consistent with an orthorhombic $4\sqrt{2}a \times 2\sqrt{2}b \times c$ structure. In both cases the compound is stoichiometric at $x = 3/8$. The latter structure corresponds to maximizing the distance between oxygen nearest neighbors, given the concentration. The sample exhibited magnetic peaks and was non-superconducting. Hence, it is likely that its electronic properties should be classified as semiconducting according to the distinction made in the introduction.

Turning next to the TEM data, a reference study was performed by Beyers et al. [18], on a series of slowly cooled powder samples with different $x$-values. Each sample was initially equilibrated at 500 °C for 3-4 days, then cooled to room temperature over a 20 hour period. Superlattice wavevectors were seen in all samples for $x > 0.28$. In the interval $0.28 < x < 0.65$ the Ortho-II phase appeared, although in an asymmetric fashion with the superlattice reflections much sharper for $x > 0.5$ than below (most probably indicating correlation along the c-axis as well). Between $x = 0.65$ and $x = 0.90$ a progression of very weak superlattice spots were detected, comprising $(3/5, 0, 0), (5/8, 0, 0)$ and $(2/3, 0, 0)$ reflections. In this interval the Ortho-II peak disappeared, except at $x = 0.65$, where an overlap existed. The super lattice peaks appeared generally in pairs, corresponding to the wavevectors belonging to the same star. Hence, $(m/n, 0, 0)$ and $((n-m)/n, 0, 0)$ were always symmetrically represented. Similar studies by Reyes-Gasga et al. [19],

[20] exhibited in general the same features but additional weak spots were found on occasion at (1/4,0,0) and (1/5,0,0). Now, it is of course impossible to determine the arrangement of oxygen atoms and vacancies from the diffraction pattern alone (this is even more true if only one peak is detected), although the concentration poses a strong constraint. However, the data presented are all compatible with a model, where the oxygens are ordered in chains along the b-axis, but with different spacings between the chains. Thus, the (2/3,0,0) superlattice spot corresponds to a structure with two filled chains alternating with one chain of vacancies, or alternatively one filled chain alternating with two vacant chains (in general both alternatives were present, although of course for different oxygen concentrations). Hence, all of these structures including the Ortho-I and Ortho-II can be be classified as belonging to a homologous series of chain -structures. the Ortho-I "super"-lattice peak simply being the original Bragg peak (1/1,0,0).

Reyes-Gasga and coworkers [19] proceed by arguing that the members of the homologous series - not including Ortho-I and Ortho-II - are all transient states. This is done both from an analysis of the scattering geometry and from *in-situ* heating experiments in vacuum. Finally, diffraction spots of the $4\sqrt{2}a \times 2\sqrt{2}b \times c$ structure were always detected in the late stage of the *in-situ* heating experiments, after the sample had become (pseudo)-tetragonal. This structure cannot be classified as a member of the above mentioned homologous series of chain structures.

The question of why the additional phases never has been found in neutron- nor X-Ray diffraction work remains to be answered. Initially, there were speculations, that it is due to TEM being an interacting probe - the structures being created by the beam. However, such a proposal is contradictory to intuition, exposing the material to heat should destroy an ordered phase, not create it. Also, several groups have performed careful test-measurements on their TEM-equipment. Sample preparation techniques are seemingly similar. Hence, we are left - for a solution - with the inherent differences between the experimental techniques. Here, two properties are evident. Firstly, diffraction is a bulk technique, while TEM-imaging is done on a very small part of the sample. Thus, TEM is in a sense better at probing fluctuations. Secondly, the minimal size of coherence-volume that can be detected is smaller for TEM probes. Especially the latter circumstance might be crucial, because the additional phases probably lacks registry along the c-axis. A more thorough discussion of these matters will be given in chapter 3.

## 2.3 Review of the Structural Phase Diagram: Theory

Considerable effort has gone into the molding of a theoretical description of the ground states and the thermodynamics of the oxygen ordering in YBCO. Ultimately the goal is to base such a description on the electronic structure of the material. Unfortunately, a serious problem arises when attempting to pursue such an endeavour. To illustrate this, let us take the example of the ASYmmetric Next Nearest Neighbor Ising (ASYNNNI) model, originally proposed by de Fontaine and coworkers [21].

The ASYNNNI model is formulated in terms of *effective* pair interactions (EPI's) between the oxygens in the basal plane. The EPI corresponding to an interaction over the distance (n) is formally defined by

$$V_n = 1/4(W^n_{oo} + W^n_{xx} - 2W^n_{ox}), \tag{1}$$

where $W^n_{oo}$ represents the total energy in the YBCO unit cell averaged in the thermodynamic sense over all configurations in the basal plane, which contains a pair of oxygens with the given distance (n). Similarly, $W^n_{xx}$ corresponds to the averaged total energy when two vacancies are present at the specified distance.

and $W^n_{ox}$ relates to oxygen-vacancy pairs. The thermodynamical averaging is done at constant oxygen concentration. The EPI's should not be confused with "conventional" pair potentials; they are derived from knowledge about the total three dimensional Hamiltonian for the YBCO system.

Now a "projected" Hamiltonian valid for the description of the ordering process in the basal plane can be formulated in terms of an expansion in the EPI's:

$$H_{2D} = \sum_{(n)} V_{(n)} \sum_{ij}^{(n)} \sigma_i \sigma_j + \mu_{2D} \sum_i \sigma_i. \qquad (2)$$

Here $\mu_{2D}$ is the "projected" chemical potential. $\sigma_i$ is the site occupancy variable for site $i$: it is 1 if the site is occupied, 0 if vacant. In the ASYNNNI model the expansion is truncated to contain only the nearest neighbor (NN) and next nearest neighbor (NNN) terms. The NNN interactions are allowed to be anisotropic, leading to a total of three EPI's, $V_1, V_2$ and $V_3$. Here, the $V_1$ interaction corresponds to the NN term, $V_2$ to the NNN term where the oxygens bridge a copper site in the basal plane and $V_3$ to the NNN term where the oxygens do not bridge any copper. An illustration is given in Fig. 3.

Superficially, the scheme for investigating the 2-D thermodynamics of the oxygen ordering is now specified: the EPI's should be calculated using e.g. band-calculations, and the thermodynamics derived from Eq. 2. However, it is impossible to average band-calculations in the thermodynamic sense required in the definition of the EPI's. Thus, to derive the total Hamiltonian we need to know the thermodynamics, and to understand the thermodynamics we need to know the total Hamiltonian. One solution to this problem is to treat the interaction with the rest of the unit-cell in a phenomenological way. For the ASYNNNI model, the simplest (and crudest) approximation is to assume that the three interaction potentials are concentration and temperature independent.

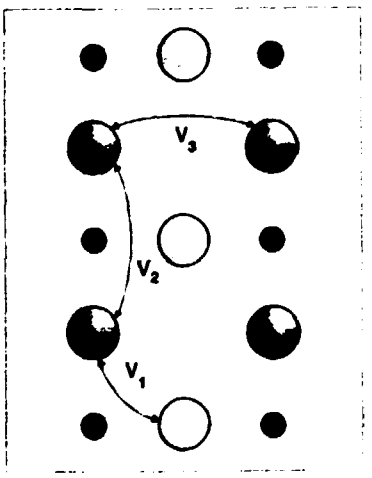


*Figure 3. Definition of effective pair interactions. $V_1, V_2$ and $V_3$ in the ASYNNNI model of oxygen ordering. The lattice in the basal plane is displayed: copper sites are marked by small spheres, filled oxygen sites by large spheres (all oxygen sites are filled in this diagram). $V_1$ is the nearest neighbour oxygen-oxygen interaction. $V_2$ and $V_3$ refer to the asymmetric next nearest neighbour interactions, where hybridization is taken into account, when the oxygens bridge a copper site ($V_2$).*

### 2.3.1 The ASYNNNI Model

In the following the EPI's will be treated as conventional concentration independent pair potentials. The oxygen configuration in the basal plane can then be described in terms of an anisotropic lattice gas model. We neglect elastic forces, and therefore the O(1) and O(5) sites will constitute a square lattice. Each lattice node - indexed by a single index i - may be either vacant or occupied. Correspondingly, the state of the node $\sigma_i$ is defined to be either 0 (vacant) or 1 (occupied). The Hamiltonian takes the form

$$H = -V_1 \sum_{ij}^{NN} \sigma_i\sigma_j - V_2 \sum_{ij}^{NNN-Cu} \sigma_i\sigma_j - V_3 \sum_{ij}^{NNN-Vac} \sigma_i\sigma_j - \mu_{2D} \sum_i \sigma_i, \quad (3)$$

where $\mu_{2D}$ is the chemical potential. NN denotes summation over nearest neighbours only, NNN-Cu summation over next nearest neighbors bridging a copper-site only, and NNN-Vac summation over next nearest neighbors not bridging a copper site, cf. Fig. 3.

A ground state analysis of the ASYNNNI model was performed by direct enumeration by Wille and de Fontaine [22]. For a fixed set of parameters $V_2/V_1$ and $V_3/V_1$ they minimized the energy. Eq. 3, over as many combinations of $\sigma$'s as possible. Completely ordered structures were found only at $x = 0.5$ and $x = 1.0$, and the total number of ground states appearing when varying the parameters was eight. Later Stoltze [23] was able to show rigorously that these proposed eight structures actually exhausted the set of possible stable ground-state structures.

Requiring next that both the Ortho-I and Ortho-II structure shall be stable at low temperatures, the $T = 0$ phase diagram is fully determined. The resulting inequalities imposed on the interaction parameters are: $V_1 < 0$, $V_2 > 0$ and $0 > V_3 > V_1$. This is as expected from simple chemical arguments: all interactions are basically (screened) repulsive Coulomb-interactions, except for the $V_2$ coupling, where the hybridization effects should be taken into account. Inoue et al. [24] arrive at the same conclusion $V_2 > 0 > V_3 > V_1$ from a tight-binding calculation.

For $T > 0$ there exists no closed-form solution to the Hamiltonian, Eq. 3. Simple mean field as well as Bragg-Williams approximations have turned out to behave badly. In consequence, the majority of the theoretical studies has been done using cluster variational methods (CVM), Monte Carlo simulations (MC) or transfer matrix calculations (TM). It is possible to compare the three techniques, by relating the CM and TM results of Aukrust et al. [25] to the CVM calculations of Wille et al. [26]. Both groups performed reference calculations of the structural phase diagram using $(V_2/V_1, V_3/V_1) = (-0.5, 0.5)$. MC and TM results are coincident at all temperatures above room temperature, while CVM results for the order/disorder transition temperatures in general are from 5% to 20 % above the results obtained using MC and TM, as might be expected from a mean field approach. The force of the MC technique is its broad applicability, e.g. it may be used for dynamical studies. Traditionally, slow convergence at low temperatures or near phase transitions has caused problems. However, due to a variety of tricks ("the n-fold way" [27], the Swendsen-Wang technique [28] and the Ferrenberg-Swendsen method [29]) these problems can by now to a large extend be avoided in equilibrium simulations. Thus, it is realistic to perform room temperature studies of the ASYNNNI model using, say 100 x 100 lattice sites, even on a serial computer. Also, the ingenious work by Lee and Kosterlitz recently [30], facilitates the distinction between continiuous and even very weak first order transitions.

As mentioned earlier, deriving the interaction potentials (or the EPI's) directly from first-principles is difficult. Using the rather crude Connolly and Williams [31] mode of approximation Sterne and Wille [32] found the values $V_1 = -372.5$ meV, $V_2 = 130.4$ meV and $V_3 = -60.0$ meV. With this set of parameters and employing

a 4- and 5-point CVM approximation Ceder et al. [33] calculated the theoretical phase diagram. Their results are reproduced in Fig. 4.

The phase diagram of Ceder at al. contains four stable phases: a high temperature disordered tetragonal phase (T), and three orthorhombic phases, Ortho-I (OI), Ortho-II (OII) and Anti-Ortho-I ($\overline{OI}$). At the stoichiometric concentration $x = 1.0$ the ground state of Ortho-I consists of alternating chains of filled and vacant oxygen sites. The sites in the filled chains bridge the basal plane copper-sites. The degree of degeneracy of this phase is obviously two. Similarly for the Ortho-II, at the stoichiometric concentration $x = 0.5$ the ground state consists of one chain of filled oxygen sites (bridging copper sites) alternating with three vacant chains. The degree of degeneracy of this phase is four. (These definitions obviously corresponds to the similar structures determined in the experimental part.) Notice, the significance of the three interaction parameters: $V_1$ empties the O(5) sites at low temperatures, $V_2$ creates the chains and $V_3$ stabilizes the Ortho-II structure.

A very important property of the model is that for $k_BT \ll V_2$ the $V_2$ parameter succeds in aligning (nearly) all oxygens into chains. The system accordingly behaves **quasi-onedimensional** at low temperatures. Actually, it has been proven from CVM calculations (using the Sterne and Wille set of parameters) that the site-occupancy of the O(5) sites goes to 0 at a concentration independent temperature around 300 K, and simultaneously the next nearest neighbour oxygen correlation function in the direction that bridges the copper sites goes to 1, again at a (somewhat concentration dependent) temperature around 300 K [33]. Thus, for temperatures below 300 K, to a good approximation, there are no "free" oxygens, they are all positioned in very long chains. This behaviour has important consequences for theory (and experiment).

First, we notice that *phase seperation cannot take place* in one dimension. For the ASYNNNI model this means, that at e.g. a non-stoichiometric position in the Ortho-I phase, the equilibrium configuration is that of a percolating Ortho-I cluster with dynamic fluctuations of low-concentration clusters (among these Ortho-II clusters) within it. For $T \to 0$ the chains will become increasingly longer, and the remaining entropy will be associated with translational degrees of freedom for the chains. Ultimately, at $T = 0$ degeneracy appears[3]. At, say $x = 0.80$, any configuration with the correct average concentration, that consists of a mixture of infinitely long chains positioned according to the Ortho-I structure and infinitely long chains positioned according to the Ortho-II structure will be a ground state. The situation is analogous for non-stoichiometric positions in the Ortho-II phase. Such extensions of non-stoichiometric states to $T = 0$ is also known from the 2-D ANNNI (Axial Next Nearest Neighbor Ising) model, which has been the focus of intense studies by Monte Carlo simulations, free fermion theory and other techniques.

Next, it is evident that for sufficiently low temperatures the ASYNNNI model can be mapped into the Ising chain Hamiltonian, with $V_3$ being the antiferromagnetic nearest neighbour interaction in the latter model [33]. Likewise, the chemical potential $\mu_{2D}$ maps into the external field. Here we should use an alternative formalism, where $\sigma_i = -1$ corresponds to a vacancy and $\sigma_i = 1$ to a particle. The solution to the chain Hamiltonian is of course known. At large positive fields the stable phase is ferromagnetic with all spins up, then antiferromagnetic for small external fields, then ferromagnetic again with all spins down for large negative fields. Translating back to the ASYNNNI model we find three stable phases: all O(1) chains filled (Ortho-I), every second chain filled (Ortho-II) and all chains empty. The latter does not correspond to the tetragonal phase, which is two-dimensional, but to the ordered orthorhombic Anti-Ortho-I phase

[3] *A phase transition takes place at $T = 0$: the minority clusters become percolating.*

shown in Fig. 4. At nonstoichiometric positions ($x \neq 0$) it consists of long oxygen chains, ordered orientationally, but not translationally. This analysis is valid as long as the one-dimensional approach is solid.

We will offer a few extra comments to this quasi-one-dimensional property. Firstly, it should be realized that the degeneracy at $T = 0$ will be lifted by nearly any perturbation, but provided all perturbations are sufficiently weak, there might still be a temperature window between the alignment of all oxygen particles and the onset of the pertubation effects, where the one-dimensional description is valid. Secondly, the estimated temperature (300 K) for the alignment is nearly coincident with the temperature where the kinetics "freezes" which makes it hard to predict whether any one-dimensional type behaviour can be experimentally detected (or alternatively experimentally prove a casual relation behind the coincidence). Finally, the concentrations at which the $\overline{OI}/OII$ and $OI!/OI$ phase transitions take place are (nearly) temperature independent in the one-dimensional limit. The corresponding Ortho-II span is $0.25 < x < 0.75$.

The CVM result for the phase diagram reported above predicts all phase transitions to be second order, except the T-OII and $\overline{OI} - OII$ transitions. As apparent in Fig. 4 a small miscibility gap appears for these transitions for intermediate temperatures (again, at low temperatures the two phase region collapses due to one dimensionality). In partial contradiction to this TM and MC results predict all phase transitions to be second order [25]. Aukrust et al. [25] also assigns universality classes to the various transitions. The relevant universality-class for the T-OII and $\overline{OI} - OII$ transitions are the Ashkin-Teller class, which probably gives the reason for the discrepancy, because mean field approximations are known to create erroneous first-order transitions for this class of transitions [34].

### 2.3.2 The Extended ASYNNNI Model

If the homologous series of chain structures mentioned in the experimental part are stable, longer range interactions are needed in order to account for them. It is easy to add long range terms of the type $\sum_{ij}^{5\Lambda} \sigma_i \sigma_j$, where the summation is over all fifth nearest neighbors, to the ASYNNNI Hamiltonian, Eq. 3, but calculations become very cumbersome. However, as mentioned earlier, and originally pointed out by de Fontaine et al. [35], at the relevant low temperatures the system behaves quasi-onedimensionally. All pair interactions can then be projected onto the direction normal to the chains. Furthermore, because the O(5) sublattice is completely depleted, there will effectively only remain interactions between parallel oxygen-chains with a spacing that is an integer multipla of $a$, the side length in the unit cell. Such one-dimensional behaviour can be modelled in terms of a 1-D Ising model with long range repulsive terms, where the nearest neighbour term corresponds to the $V_3$ interaction. The longer range interactions, which we may denote $V_4, V_5, V_6$, etc., are expected to obey the convexity relation $V_n < 1/2(V_{n+1} + V_{n-1})$, valid for (screened) Coulomb repulsion. The quasi one-dimensional ground states for such convex interactions are known [36], and may be obtained exactly by a continued fraction algorithm, shown to be completely equivalent to a structure combination branching mechanism [37]. The branching algorithm as reported by de Fontaine et al. [35] is reproduced in Fig. 5. To understand the structures present we will symbolize a filled row on the O(1) sub-lattice by $< 1 >$, and an empty one as $< 0 >$. Thus the structures Ortho-I and Ortho-II are now designated as $< 1 >$ and $< 10 >$, respectively, the brackets denoting periodic repetition. These two structures (level I in Fig. 5) are the generating structures for those shown at successive levels (II, III, IV, etc.). The level II structure is obtained by telescoping level I structure elements $< 1 >$ and $< 10 >$ to form structure $< 110 >$, also known as the Ortho-III structure. At level III, $< 10 >$ combines with $< 110 >$

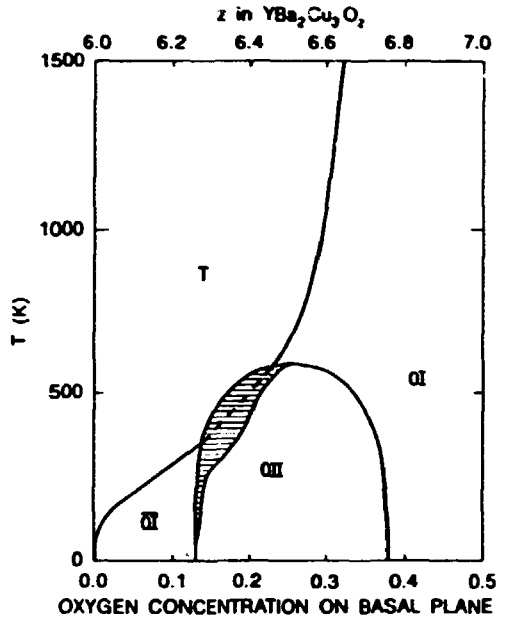


*Figure 4. The theoretical phase diagram calculated by a cluster variational method by Ceder et al. [33], using ab-initio values for the interaction parameters ($V_1 = -372meV, V_2 = 130meV, V_3 = -60meV$), derived from tight binding calculations by Sterne and Wille [32]. Four phases are present: a disordered tetragonal phase (T), and three orthorhombic phases, Ortho-I (OI), Ortho-II (OII) and Anti-Ortho-I ($\overline{OI}$). A small miscibility gap is associated with the T-OII and $\overline{OI}$-OII phase transitions.*

to form < 1110 >, etc. The stoichiometric composition is indicated below the structural formula for each of the "branching" phases in Fig. 5. The vertical scale is practically that of temperature, as branching to increasingly higher levels is expected to occur at successively lower temperatures.

Undoubtly, the analysis above is theoretically solid. However, the question remains how to judge the strength of the $V_4$ parameter, and most notably whether the OIII phase become stabilized above or below the temperature, where the kinetics in the sample freezes. Ceder et al. [38] computed the low temperature phase diagram when adding the $V_4$ parameter to the simple ASYNNNI phase diagram with a CVM technique. As expected they found that the lifting of the $T = 0$ degeneracy causes phase separation in most parts of the diagram below the maxima temperature, $T_{OIII}$ for the OI to OIII phase transition. (Landau symmetry rules: the OIII structure has a periodicity three times that of OI, hence a third order invariant is expected in the free energy of the OIII phase, and a first order transition is predicted.) On varying the strength of the parameter, $T_{OIII} > 350K$, even for $V_4$ as low as 100 K. However, the tendency for mean-field type calculations to overshoot transition temperatures should be borne in mind.

Obviously, the chain structures apperaring in the branching scheme of Fig. 5 are reminiscent of the homologous series experimentally observed. A detailed analysis shows that all the experimentally observed patterns can be accounted for by (a subset of) the first four levels of the branching scheme [35]. When comparing with the TEM results of Beyers et al. [18] a compelling agreement is found, even quantitatively.

However, experimentally the most complete investigations suggest that the states in the homologous series are transient [19]. Thus, an alternative explanation

for these states might be in terms of the low temperature kinetics of the standard ASYNNNI model. Little work has been done on this aspect, mostly due to general convergence problems at the temperatures in question. Burmeister et al. [39], [40] reports on a MC study, where transient phases of several of the homologous chain-states were found when inspecting the instanteneous configurations appearing during the relaxation process. However, no quantitative statements were made. Clearly, it would be helpful to derive quantities like the static structure factor for comparison with experiments.

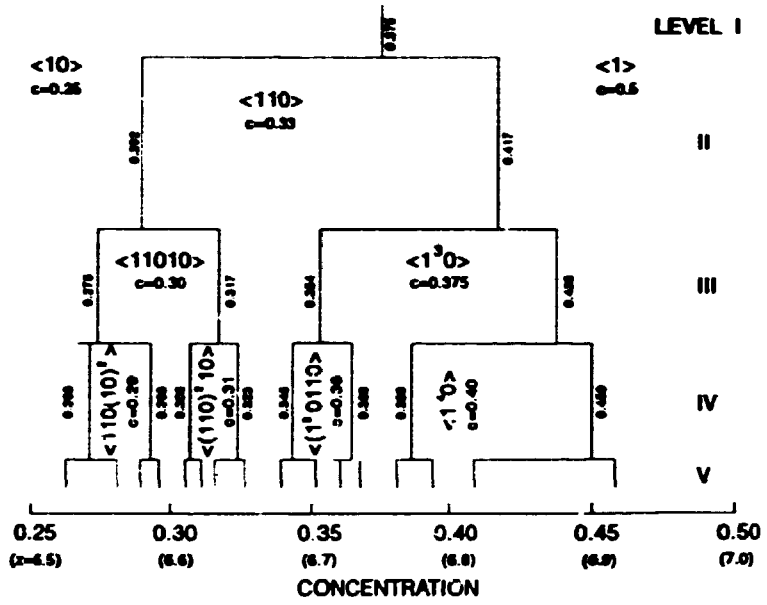


*Figure 5. Branching algorithm for quasi one-dimensional ordered superstructures stabilized by the long range interactions in the extended ASYNNNI model. The oxygen concentration $c = x/2$ are marked for the stoichiometric compositions. Adapted from Ref. [35]. See text.*

### 2.3.3 Beyond the ASYNNNI Model

The ASYNNNI model as specified by the Hamiltonian in Eq. 3 has proven itself an excellent tool for rationalizing a vast pool of structural and thermodynamic data. (The results reported in this thesis clearly emphasizes this point of view.) Actually, only one of the observed, stable or non-stable, structural phases presented above cannot be explained within the framework it provides: the $4\sqrt{2} \times 2\sqrt{2}$ structure. However, it is clear that the model is an oversimplification. The single site potentials have been left out, and the pair potentials should depend on the number and the distribution of charges in the system. These quantities change drastically with oxygen content x. Furthermore, the elastic degrees of freedom, most notably the internal strain and the energy bound in twin domain walls, have been neglected. In the following we will describe in a qualitative sense what happens when the fundamentals of the electronic properties are taken into account.

The interaction parameters in the Hamiltonian, Eq. 3 are purely phenomenological, although we have argued, that their signs and relative strengths corresponds to what would be expected from simple structural chemistry arguments. A more physical description has been provided by Aligia and coworkers [41], [17], [42].

[43], [44] using the Hamiltonian

$$H = E_0(x)\sum_i \sigma_i + \frac{1}{2}\sum_{ij} V_{ij}\sigma_i\sigma_j \tag{4}$$

where the summation is over interactions between all lattice sites. The interaction potentials are given as screened Coulomb potentials.

$$V_{ij} = -\frac{q^2}{4\pi\epsilon_0 r_{ij}}\exp(-r_{ij}/\lambda), \tag{5}$$

where $r_{ij}$ is the distance between sites, $\lambda$ the screening length, $q$ the charge of oxygen ions in the basal plane and $\epsilon_0$ the dielectric constant. The one exception from this assignment is the interaction between second nearest neighbors bridging coppers - the $V_2$ interaction, using the term from the ASYNNNI model.

$$V_2 = -\frac{q^2}{4\pi\epsilon_0 b}\exp(-b/\lambda) + E_{hybr} \tag{6}$$

Here, the hybridization is taken into account by the additional attractive term $E_{hybr}$. We will leave the discussion of the premises of this model, and use it to illustrate the effect of introducing the electrons. These couple in several ways to the Hamiltonian, most notably through the screening length, but also through $q$ and the hybridization.

The most prominent change in the electronic properties is the metal-insulator transition, taking place around $x = 0.4$ at low temperatures[4]. In the insulating phase the screening length ought to be large. Hence, for fixed $E_{hybr}$ we could imagine the Coulomb repulsion part of $V_2$ becoming more important than the hybridization term. All interactions are then negative and the ground state will roughly be determined by which structure (at a given concentration), that enables the nearest neighbor distance between oxygens to be maximized. The only established stable structure (apart from the disordered tetragonal) in the insulating regime is the $4\sqrt{2} \times 2\sqrt{2}$ phase [16], which exhibits exactly this property. For larger $x$-values, beyond the metal-insulator transition, $\lambda$ becomes much shorter (although still appreciable, due to the low number of carriers). $V_2$ will accordingly turn positive, and the situation is reminiscent of the extended ASYNNNI model, with the same resulting homologous series of chain structures.

A more detailed description of the possible ground states of the Hamiltonian Eq. 4, and a derivation of $E_{hybr}$ from an extended Hubbard Hamiltonian is given in references [43], [44]. We will refrain from a discussion of the validity of the model, because it bears on experimental details of the electronic transport properties of YBCO, a subject that is outside the scope of this thesis.

Understanding the thermodynamics of the oxygen ordering process in YBCO may arguably be simpler than describing the normal state electronic properties of the material. In the latter case, experimentally, the anisotropy and the existence of two channels for transport: the basal plane and the $CuO_2$ bilayers pose great challenges. Theoretically, the normal state properties remain at the core of the science of High Tc materials. Still, it is the hope of the author that it will become possible in the future to describe the coupling between the oxygen ordering and the electrostatics of the media, including the charge transfer effects in terms of e.g. tight-binding calculations combined in a self-consistent manner with thermodynamic tools.

[4]The precise position of the metal-insulator transition at higher temperatures, and its definition, is still debated in the literature.

## 2.4 Monte Carlo Simulations of the ASYNNNI Model

Monte Carlo simulations of thermodynamic phenomena are by now an established field [45], [46]. Based on a known Hamiltonian for a model system the Monte Carlo method generates a time sequence of phase space states of the system by performing a random walk. In equilibrium, thermodynamic observables found by averaging over this set of states are then used as a numerical approximation to the exact ensemble averaging over all of phase space. The method is known to give the correct answers in the limit where time goes to infinity. It applies to discrete as well as continuous, and classical as well as quantum mechanical systems. In certain cases, a direct interpretation of the time sequence can be established as well, allowing for studies of non-equilibrium physics.

The object of this section is to discuss Monte Carlo simulation technique in relation to the ASYNNNI model, Eq. 3, a classical two dimensional lattice gas system. A short introduction to Monte Carlo simulations in general will be given along with specific algorithms for the case of the lattice gas. Details relating to the simulations presented in chapter 3 and 4 can be found here. First, some thermodynamic variables for the lattice gas model in question will be derived.

### 2.4.1 The Lattice Gas Model

The lattice gas model describes diffusion of particles on a rigid square lattice with $L \times L$ nodes. At a given time $t$ each lattice node - identified by a single index i - is either vacant or singly occupied. Correspondingly the state of the node $\sigma_i(t)$, will be either 0 (vacant) or 1 (occupied). The phase space state, x, of the total system is given by the configuration $x(t) = \bar{\sigma}(t)$. The Hamiltonian, H, has the form - from Eq. 3

$$H = -\sum_{i,j} V_{ij}\sigma_i\sigma_j - \mu_{2D}\sum_i \sigma_i. \tag{7}$$

where $\mu_{2D}$ denotes the chemical potential. Because elastic effects are neglected only two independent thermodynamic variables appear, $\mu_{2D}$ and absolute temperature T. The density is $c = \frac{1}{L^2}\sum_i \sigma_i$, corresponding to an oxygen stoichiometry of $x = 2c$. The lattice gas can by a substitution ($S_i = 2\sigma_i - 1$) be mapped into a generalized 2D Ising model. Thus, spin terminology is often used.

Order parameters for the Ortho-I and Ortho-II phases are given as usual in terms of staggered magnitizations, that is by adding sums over different oxygen sublattices, multiplied by plus or minus 1. Following Aukrust [25] we define 8 interpenetrating sub-lattices, as indicated in Fig 6. The Ortho-I order parameter is defined

$$\Theta_{OI} = < \frac{1}{4} \mid \Theta_1 + \Theta_2 + \Theta_3 + \Theta_4 - \Theta_5 - \Theta_6 - \Theta_7 - \Theta_8 \mid > . \tag{8}$$

$\Theta_{OI}$ is easily seen to be 1 in the Ortho-I phase, $\frac{1}{2}$ in the Ortho-II phase and 0 in the tetragonal phase. Analogous for the Ortho-II phase[5]

$$\Theta_{OII} = < \frac{1}{2} \mid (\Theta_1 + \Theta_2) - (\Theta_3 + \Theta_4) + (\Theta_5 + \Theta_6) - (\Theta_7 + \Theta_8) \mid > \tag{9}$$

where $\Theta_{OII}$ is 1 in the Ortho-II phase, and 0 in both the tetragonal and the Ortho-I phase. Notice, that because $\Theta = 1$ and $\Theta = -1$ corresponds to the same energy the thermal averaging has been done over absolute values. When sampling moments of the order parameters, the || operators should be removed from the definitions, Eq. 8 and Eq. 9.

[5] A vectorized version of the Ortho-II order parameter may be needed in some cases. However, for the work presented in this thesis the scalar definition is sufficient.

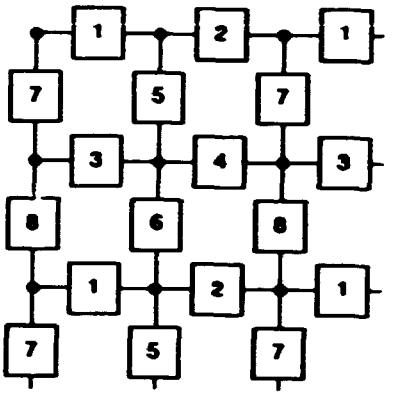


*Figure 6. The eight oxygen sublattices in the basal plane used to define the Monte Carlo order parameters for the ASYNNNI model. The full circles represent Cu(1) sites, and the numbered squares represent the oxygen sites. The numbering of the sublattices follows Aukrust et al. [25].*

The conjugate parameter for any order parameter, the susceptibility, can be found using

$$\chi = \frac{L^2}{k_B T}(< \overline{\Theta^2} > - < \overline{\Theta} >^2) \tag{10}$$

Here again, it is important that the absolute operators || are left out, which is why we have used the symbols $\overline{\Theta}$ in stead of $\Theta$.

The thermodynamic response functions are related to the thermodynamic potentials by the fluctuation- dissipation theorem. Thus the specific heat C is given by the fluctuations in internal energy per site $U = \frac{<H>}{L \times L}$

$$C = \left(\frac{\partial U}{\partial T}\right)_{\mu_{2D}} = \frac{L^2}{k_B T^2}(< U^2 > - < U >^2). \tag{11}$$

Another important response function is the 'compressibily' $\Gamma$ given by the fluctuations in density c

$$\Gamma = \left(\frac{\partial c}{\partial \mu_{2D}}\right)_T. \tag{12}$$

### 2.4.2 Equilibrium Simulations

By definition the thermodynamic average of any observable A of the lattice gas is given by

$$< A >= \frac{\sum_\Omega A(x) e^{-\frac{H(x)}{k_B T}}}{\sum_\Omega e^{-\frac{H(x)}{k_B T}}}, \tag{13}$$

where the summing is done over all $N = 2^{L \times L}$ states x (particle/ vacancy configurations) in phase space $\Omega$. We wish to approximate $< A >$ by $A_m$, summing only a subset $\Omega_m$ of phase space, where the number of elements m in $\Omega_m$ has to be reasonably small. Because the vast majority of configurations give vanishing contributions to $< A >$ neither sampling in a truncated grid nor random sampling will in general give valid results. The essential idea in Monte Carlo technique is in stead to sample the most important states (the low energy ones) with higher probabilities than the rest. Normalizing by such a probability function $P_m(x)$. $A_m$ is expressed by:

$$A_m = \frac{\sum_{\Omega_m} A(x) P_m^{-1}(x) \exp(-\frac{H(x)}{k_B T})}{\sum_{\Omega_m} P_m^{-1}(x) \exp(-\frac{H(x)}{k_B T})}. \tag{14}$$

One obvious choise for $P_m(x)$ is the equilibrium distribution itself $P_{eq}(x) \propto exp(-H(x)/k_B T)$. The procedure for averaging then reduces to simple summation

$$A_m = \frac{1}{m} \sum_{\Omega_m} A(x). \tag{15}$$

The problem with this approach is that computationally we do not have any means of ordering the phase space states according to energy. Thus, in Monte Carlo the sequence of phase space states $(x^1, ..., x^{n-1}, x^n, ..., x^m)$ is generated by a random walk. The transition probability $W_{ji}$ of state $x_j$ occurring at time n given state $x_i$ at time n-1 will then be independent of n, and the sequence of states can be described as a Markov chain. From general Markov chain theory [47] it follows that the criteria of detailed balance

$$\frac{W_{ji}}{W_{ij}} = e^{-\frac{H(x_j) - H(x_i)}{k_B T}}, \tag{16}$$

is sufficient to ensure equilibrium is approached[6]: $P_m(x) \to P_{eq}(x)$ for all x as $m \to \infty$. Calculated averages according to Eq. 15 are then guaranteed to approach the equilibrium values in the same late time limit.

The detailed balance criteria leaves a lot of freedom choosing $W_{ji}$. It can be shown [47] that the approach towards equilibrium is exponential with a time constant given by the second largest eigenvalue of $W_{ji}$ (the largest one always being 1). Unfortunately it is hard from a given Hamiltonian to design an optimal $W_{ji}$. Instead one generally chooses matrices where only a few degree of freedom can be changed simultaneously. This increases the chance of "staying within the equilibrium states once you are all ready there". It should be stressed that the Markov chain generated by the transition probability matrix not in any way has to mimic any physical relaxation mechanism.

In the original Monte Carlo method due to Metropolis [48], $W_{ji} = 0$ if the $x_i$ and $x_j$ configurations differ at more than one lattice point. The only possible events are thus that either nothing happens ($i = j$), or that exactly one vacancy is filled, or one particle removed. In spin-language the latter two opportunities correspond to the flip of one spin. Let the change in total energy associated with such a flip be $\Delta E$. This makes the exact transition matrix for Metropolis looks like

$$W_{ji} = \begin{cases} \frac{1}{N} & \text{one flip, } \Delta E < 0 \\ \frac{1}{N} e^{-\frac{\Delta E}{k_B T}} & \text{one flip } \Delta E > 0 \\ 1 - \sum_{i \neq j} W_{ji} & \text{no flips, } i = j \\ 0 & \text{otherwise} \end{cases} \tag{17}$$

The corresponding Metropolis algorithm can be formulated as:

1. Choose an initial configuration $x^1$. m=1.
2. Randomly pick one lattice node k.
3. Generate a random number R uniformly from [0,1[.
4. Compute the total energy difference $\Delta E$ associated with the vacancy/particle "flip" at site k. If $\Delta E < 0$ flip the site; otherwise flip it only in case $e^{-\frac{\Delta E}{k_B T}} > R$.
5. If equilibrium has been reached the new configuration $x^m$ may be used in averaging thermodynamic observables.

[6] Stictly speaking $W_{ji}$ has to be irreducible and aperiodic as well. Normally these conditions do not pose any problems for the algorithms chosen.

6. m=m+1. Goto 2.

It is easy to show, that this algorithm in fact gives rise to the transition matrix W in Eq. 17, and $\overline{\overline{W}}$ in turn is a probability matrix which fulfils the detailed balance criteria. The vacancy/particle flip at a single site is known as Glauber dynamics. (Note, that the lattice gas Hamiltonian Eq. 7 has no kinetic term. In a superficial sense we can think of this microstep: the flip as an imposed dynamics.)

The major drawbacks for Monte Carlo simulations in general are associated with finite time and finite size effects. Treating the time aspect first, it is clear that meta-stable states, long lived transients etc. can prohibit equilibrium to be reached in a number of steps that are within the capacity of any computer. Most notably such slowing down of the convergence is found at low temperature (freezing) and near phase transitions (critical slowing down). In the former case the Metropolis algorithm spends most of its time failing to do a flip ($P(x^{n+1} = x^n) \simeq 1$). It is possible to avoid such behavior to a certain extent by expelling the no-flip opportunities from the scheme: $W_{ii} = 0$, and renormalizing the rest of the $W_{ij}$'s in order that $\overline{\overline{W}}$ continues to be a probability matrix, while still fulfilling Eq. 16. Such an approach was initially described by Bortz, Kalos and Lebowitz [27] and is generally known as "the n-fold way algorithm".

Monte Carlo type averaging according to Eq. 15 only makes sense once equilibrium has been reached. However, no rigorous rule can be given to determine when the transients have died out. In practice we monitor the time evolution $A_m$ for various (relatively slowly evolving) observables A, e.g. order-parameters and moments of energy and particle concentration. Furthermore, comparison between different initial configurations can be useful. In the case of oxygen ordering in $YBa_2Cu_3O_{6+x}$, we find that a comparison between a random configuration ($T = \infty$) and the ground state configuration ($T = 0$) as initial configurations is very useful. In the first case energy is generally decreasing with time, while in the latter it must increase.

Having reached equilibrium, another concern is the number of iterations of e.g. the Metropolis algorithm that is necessary, in order that the various excitations within the equilibrium 'state' are sampled adequately. Again no definite rules can be given. In practice we monitor the evolution of the variance, $V(A)$, of the thermodynamic observable A in question and continue until it has decreased to a reasonable level. Because the configurations $x^{m+n}$ and $x^m$ are truly independent only for $n \to \infty$, the variance $V(A)$ sampled by a fixed number of configurations with a regular interval of iterations n between them, will be smaller the bigger n is. Furthermore, it generally takes much longer to calculate A(x) for one configuration x than to do one Metropolis-iteration. It follows, that a trade off between the total number of iterations and the number of samplings is needed. As a rule of thumb we sample with an interval of $N = L \times L$ iterations, corresponding to every time each spin on average has been "visited" once by the algorithm. In the literature this is known as a sampling frequency of 1 MCS/site (Monte Carlo steps per site).

Finite size problems occur predominantly in connection with continuous phase transitions, where fluctuations of all length scales are present. A presentation of some of the (rather elaborated) techniques needed to treat such problems is given below. It should be noted that such techniques are relevant, even when the correct size, shape and boundary conditions of the physical system are (known and) used. Partly to test for metastability, partly because one generally attempts to explain the physics in terms of bulk behaviour plus some finite size corrections.

### 2.4.3 Simulations of Phase Transitions

According to standard scaling theory [49], [50], [51] the free energy F of a finite system near the transition temperature $T_c$ is given in general by a homogeneous function

$$F(L,T) = L^{-(2-\alpha)/\nu} f(tL^{1/\nu}); \quad t = T - T_c \tag{18}$$

The scaling function f depends on the details i.e., the boundary conditions. The parameter $x = tL^{1/\nu}$ is known as the scaled temperature. $\alpha$ and $\nu$ are the critical exponents related to specific heat and correlation length, respectively. From the free energy the scaling properties of other observables may be derived. Most notably, the variation of the order-parameter in question $\Theta$, can be expressed in terms of critical exponents $\beta$ and $\nu$:

$$\Theta = L^{\beta/\nu} g(x) \approx t^{\beta} \text{ as } L \to \infty, \ t \neq 0. \tag{19}$$

The behaviour of the susceptibility is expressed in terms of another critical exponent $\gamma$

$$\chi = L^{\gamma/\nu} h(x) \begin{cases} \approx L^{\gamma/\nu} & \text{for } t = 0 \\ \approx t^{-\gamma} & \text{as } L \to \infty, \ t \neq 0. \end{cases} \tag{20}$$

Finally, for the specific heat

$$C - C_0 = L^{\alpha/\nu} k(x) \begin{cases} \approx L^{\alpha/\nu} & \text{for } t = 0 \\ \approx t^{-\alpha} & \text{as } L \to \infty, \ t \neq 0. \end{cases} \tag{21}$$

where $C_0$ is the non-divergent part. These formulas are valid for L larger than the coherence length $\xi$, and T close to $T_c$ only.

In principle it is possible to simultaneously determine the critical exponents and the critical temperature by a combination of temperature and size investigations, using e.g. Eq. 19, 20 and 21. In practice one may be hampered by severe cross-over effects ($\xi >> L$ for relevant T's) and the multi-dimensional fit is not unambiguous. To remedy the latter problem Binder [51] proposed to study cumulants of the energy or the order parameter $\Theta$. Thus the fourth order cumulant $U_L$

$$U_L = 1 - \frac{<\overline{\Theta}^4>_L}{3<\overline{\Theta}^2>_L^2} \tag{22}$$

is known [51] to behave according to ($U_L^*$ is a nontrivial constant)

$$\begin{array}{ll} U_L \to 0 & \text{for } L \to \infty \text{ and } T > T_c \\ U_L \to \frac{2}{3} & \text{for } L \to \infty \text{ and } T < T_c \\ U_L \approx U_L^* & \text{for } L << \xi. \end{array} \tag{23}$$

Hence, if one plots $U_L$ versus T for various L all curves will have a common intersection point located at $(T_c, U_L^*)$. This is a convenient way of estimating $T_c$ without being biased by assumptions about the critical exponents.

Finally we will demostrate how it is possibly to speed up simulations when the dependency of thermodynamic variables on a parameter is wanted, e.g. in connection with a phase transition (where the temperature-dependency of some fluctuation type variable is in question). The algorithm to be presented was recently introduced by Ferrenberg and Swendsen [29].

To understand the algorithm consider the simple Ising Hamiltonian

$$H(T,\mu,V) = -V \sum_{ij}^{NN} \sigma_i \sigma_j, \tag{24}$$

equivalent to

$$-H/(k_B T) = KS, \tag{25}$$

with $K = V/(k_B T)$ and $S = \sum_{ij}^{NN} \sigma_i \sigma_j$. In Monte Carlo simulations the thermal average of any variable A for fixed K: $< A(K) >$ is approximated by (cf. Eq. 14)

$$< A(K) >= \frac{\sum_m A_m \exp(K S_m)/P_m}{\sum_m \exp(K S_m)/P_m}. \tag{26}$$

Normally the Monte Carlo weight factor $P_m$ equals $\exp(K S_m)$, and Eq. 26 reduces to a simpel geometric sum. Notice, however, that if the set $(S_m, A_m)$ for all $i$ is *stored* during the evaluation of $< A(K) >$, we have all the information needed to evaluate $< A(K') >$ by simply inserting in Eq. 26:

$$< A(K') >= \frac{\sum_m A_m \exp((K' - K)S_m)}{\sum_m \exp((K' - K)S_m)}. \tag{27}$$

To summarize: by storing the variables $A_m, S_m$ we are able to determine the value of $< A(V,T,\mu) >$ for all values of $(V,T,\mu)$ within a certain distance in the three dimensional parameter space in stead of just in one point. (The method breaks down when the original random walk no longer gives a "representative" subset.) Thus the range of temperatures normally needed in order to determine a phase transition point is substituted by a single simulation.

For the ASYNNNI model we substitute $KS$ by $K_1 S_1 + K_2 S_2 + K_3 S_3 + (\mu/k_K T)N$, corresponding to the three interaction parameters present $V_1, V_2$ and $V_3$ and the chemical potential $\mu_{2D}$. The advantage of using the method is even larger in this case, because of the three extra dimensions. Most notably, in an attempt to fit the interaction parameters to an experimentally observed phase diagram, we may from a single Monte Carlo simulation at fixed $T, \mu, V_1, V_2$ and $V_3$, be able to simultaneously determine the phase transition temperature as function of $x$ and the interaction potentials (within certain limits).

### 2.4.4 Non-equilibrium Simulations

A dynamic interpretation of the Monte Carlo method is possible [52] for the lattice gas. The diffusion of particles is modeled by stochastic jumping between the available sites. The possible microsteps are thus vacancy-particle exchanges, also known as Kawasaki dynamics [53] (conserved local concentration, with a possible exception at the boundaries). It is assumed that the mean jump frequency is much smaller than the "phonon relaxation time". This ensures that the vacancy-particle distribution is everywhere in thermal equilibrium at all times. The interaction radius (how far can the particles jump) and a possible degree of anisotropy have to be specified.

The time step between two successive iterations is to be treated as a stocastic increase in time, $\Delta t$

$$\Delta t = -\frac{\tau \ln(R)}{N}, \text{R random number in}[0,1]. \tag{28}$$

where $\tau$ determines the absolute scale of time. ($\tau$ is the attempt frequency for a single jump). Note, that when more than one type of jumping is involved (e.g. both nearest neighbour (NN) jumps and next nearest neighbour (NNN) jumps) it may be essential to attempt these in the Monte Carlo simulation with the physically correct ratio. Normally the ratios - and even the allowed types of jumps (NNN or only NN) - are unknown. It is thus important to make sure that the achieved results from the Monte Carlo simulations are robust towards changes in interaction range.

It can be shown - using the Markovian master equation [45] - that the time dependent average of A, $< A(t) >$ (per definition found by ensemble-averaging at time t) can be approximated by averaging over an ensemble of initial states $x^1$. This means, that r statistically independent Monte Carlo series with configurations

$(x_k^1, ..., x_k^n, ...), k = 1, ..., r$ are generated. $< A(t_0) >$ is then approximated by a simple sum, evaluated at the discreet time n, which is closest to absolute time $t_0$:

$$< A(t_0) > \approx A_r(n) = \frac{1}{r} \sum_{k=1}^{r} A(x_k^n). \tag{29}$$

In practice, when simulating the kinetics after a quench from a temperature $T_1$ to $T_2$, the ensemble of initial states are generated by equilibrium Monte Carlo simulations at $T_1$.

## 2.5 Late Stage Growth Phenomena

Growth processes occur in a wealth of physical situations from the dendritic growth of a snowflake to the bulk ordering of alloys or the surface ordering of gasses on metal surfaces. Such phenomena can be characterized as time resolved studies of low symmetry structures governed by irreversible and far from equilibrium dynamics. Intense theoretical and experimental interest have been attributed to this field during the last two decades - for a review see e.g. [54], [55]. In this section we will consider the prototypical example of a lattice gas being quenched from a disordered high temperature phase to below the order/disorder phase transition temperature. The description and results can mostly be directly related to the case of oxygen ordering in $YBa_2Cu_3O_{6+x}$. The only important difference is the existence of long range elastic forces (due to internal strain) in the superconductor. The implication of the elastic contribution is not a trivial extension, cf. chapter 3.

The quenched lattice gas will generally be far from its equilibrium state. If the relaxation process requires phase seperation, nucleation or spinodal decomposition occurs, depending on whether one has quenched into the socalled meta-stable or un-stable state [55]. For the presently more relevant case of a quench into a stable phase, the relaxation process will be initiated by the random nucleation of small domains of this equilibrium phase. Depending of the degree of degeneration, domains of different types will appear. At intermediate and late times the vast majority of sites will belong to these domains. The lattice gas configuration can then be described by the topology of the interfaces, and the dynamics by the coarsening and competition between domains. An example of the evolution of these patterns for the case of YBCO is given in Fig 7. Because the lattice gas contains only short range interactions the excess energy (relative to the equilibrium energy) and therefore the thermodynamic forces will actually reside solely in the interfaces.

The usual crystallographic translational- and rotational symmetries does not apply to these systems with their stocastic type interfaces. A temporal scaling type of symmetry is often postulated in stead. Intuitively one expects that new information does not appear on all time scales: after a while the relative size-distribution of the different types of domains towards each other reach a steady state. The dynamics can then be described simply in terms of the evolution of some average domain size. Quantitatively this dynamical scaling can be formulated in terms of the domain-size distribution P(R,t), defined as the probability that a randomly chosen site of the lattice gas belongs to a domain of linear dimension R at time t. The average domain size then becomes

$$\overline{R}(t) = \int_0^\infty RP(R,t)dR. \tag{30}$$

The dynamical scaling implies that the probability of the normalized linear size $x = R(t)/\overline{R}(t)$ is independent of time

$$P\left(\frac{R(t)}{\overline{R}(t)}, t\right) = P(x,t) = f(x). \tag{31}$$

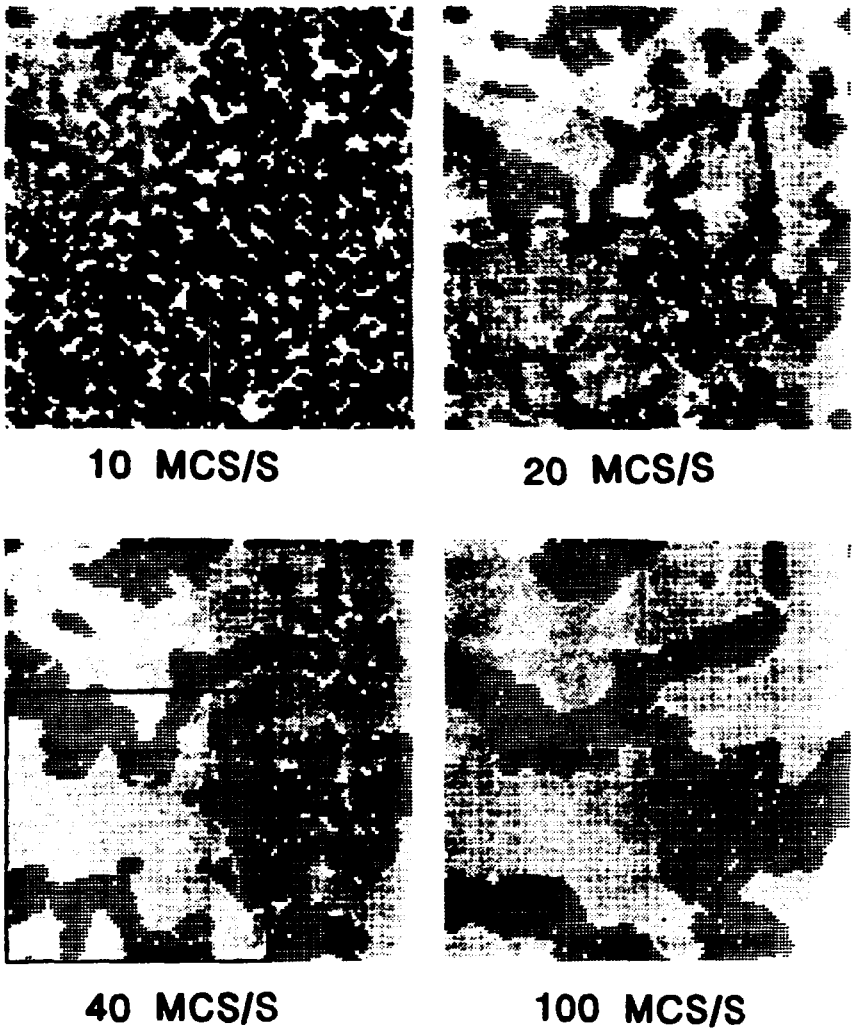


*Figure 7. Four snapshots of lattice gas configurations from a Monte Carlo simulation of the ASYNNNI model, showing the time evolution after a temperature quench to below the order/disorder phase transition. The quench was performed at the stoichiometric concentration $x = 1.0$ into the Ortho-I phase. The twofold degeneracy of this phase give rise to the nucleation, coarsening and competition between 2 different types of domains, marked with grey and black dots. The time scale is in Monte Carlo steps per site (MCS/S). A subconfiguration in snapshot 3 has been marked. The relative size of this subconfiguration with respect to the full snapshot is $(\frac{40}{100})^{0.5} = 0.63$. The equivalent appearance of this subconfiguration and the full configuration in snapshot 4 is a pictoral illustration of the fact that the model exhibits dynamical scaling in the late time regime with an algebraic growth law of the average domain size $l(t) \propto t^{0.5}$. For details see text.*

For an illustration see Fig 7.

As a consequence of the scaling symmetry all length variables $l$ follow the same growth law $l(t) \propto \overline{R}(t)$ in the late stage regime. Accordingly we can test the scaling hypothesis by comparing various length variables. Computationally the

self-averaging variables are preferable. Among these the most important one is the excess energy $\Delta E$, which qualify as a length measure, because it is proportional to the perimeter of the interface network.

The nature of possible late stage growth laws is of imminent interest. From a mixture of field theoretical approaches [56], [57], [58], [59] and Monte Carlo simulations [60], [61], [62] the emerging picture at present is the existence of algebraic growth laws

$$l(t) \propto t^n. \tag{32}$$

This functional dependency is universal in the sense that the value of n is independent of temperature, interaction parameters, interaction range, boundary conditions, degree of degeneration and even the dimensionality of the system. Thus n is believed to depend only on whether the order parameter in question is conserved or not. (The order parameter is conserved if particles at the interface between two types of degenerate domains cannot diffuse across the border and transform into particles belonging to the other domain.) The concept of universality have important consequences on experiments, because inhomogenieties and lack of detailed information need not be fatal.

The case for the non conserved order parameter - attributed to Lifshitz, Allen and Cahn [56], [57] - is very strong. The exponent is $n = \frac{1}{2}$. For the conserved order parameter (attributed to Lifshitz-Slyozov [58]) the argument for degrees of degeneracy exceeding 2 relies heavily on Monte Carlo simulations with their inherent finite-time problems. (Theoretical descriptions are difficult as one has to understand the thermodynamic driving force applying to the growth of a single interface-segment and simultaneously solve the global problem of finding the distribution function f(x) in Eq. 31). However, consensus seems to be [54] that $n = \frac{1}{3}$ is valid in general. The slower kinetics in the latter case is easily understood. Because the particles belonging to one type of domains cannot transform into the other types long range diffusion of single particles through 'hostile' domains have to take place.

# 3 The Structural Phase Diagram and the Thermodynamics of Oxygen Ordering

## 3.1 Introduction

The object of the present study [63], [64] is twofold: firstly, to obtain experimental information on the structural and thermodynamic properties of the oxygen ordering process in $YBa_2Cu_3O_{6+x}$, detailed enough to allow for a distinction between various microscopic models. Secondly, to attempt a coherent description of these measurements in terms of the simple ASYNNNI model of oxygen ordering.

The main experimental problems are assumed to be sample dependencies, slow oxygen kinetics at low temperatures and systematic errors in the determination of the absolute oxygen stoichiometry. Hence, it is proper to perform *simultaneous* studies of the various structural and thermodynamic properties using the same sample throughout. Moreover, care should be taken to assure equilibrium behaviour to as low temperatures as possible, and the relaxation rate towards equilibrium should be monitored. Finally, a systematic investigation of various standard ways of measuring the oxygen stoichiometry should be included.

With these constraints, we have designed and build a gas-volumetric equipment for *in situ* use on a powder neutron diffractometer. The gas-volumetric equipment consists of a closed environment connecting the sample to an oxygen reservoir of constant volume. Monitoring the partial pressure in this system allows us to evaluate the relative oxygen uptake in the superconductor (the value $\Delta x$) and - by following the temporal evolution - the relaxation towards equilibrium. The *in situ* thermodynamics of the oxygen ordering processes can be inferred from the partial pressure in the bulb, through the condition of equal oxygen chemical potential outside and inside the superconductor. We note, that pressure monitoring probably provides the most sensitive measurement of any thermodynamic response function, a relevant observation when probing phase transitions.

The theoretical part focus on the ASYNNNI model. This model is chosen because it is the simplest possible lattice gas model, that complies with the structural condition: the existence of the Ortho-II phase. Moreover, it exhibits a rich variety of thermodynamic properties including competing interactions, dimensional cross-over phenomena and local ordering schemes that allow for a vast number of predictions to be made. Also, as evident from the review given in chapter 2, the ASYNNNI model provides the basis for several more advanced theoretical attempts. The theoretical calculations will primarily be done by means of *Monte* Carlo simulations. The background for both the model and the Monte Carlo technique is given in chapter 2. In order to achieve more general conclusions, we will include a few additional results from the literature in the theoretical discussion.

The outline of the chapter is naturally divided in four parts: experimental technique, experimental results, theory, and a general discussion.

The section on experimental technique describes the preparation of the sample, the gas-volumetric set-up and details related to the neutron powder diffraction measurements. The sixteen run-series performed are presented together with a description of how we calibrate the absolute oxygen stoichiometry.

Next, the experimental results are presented, starting with the structural phase diagram. Following that an analysis of the broadening of the Bragg peaks for all neutron diffraction scans will be performed and related to twin domain sizes in the orthorhombic regions. Results for the equilibrium partial oxygen pressure

are given, and it is shown how these are related to the chemical potential in the superconductor. Finally, our data for the relaxation of the oxygen in-diffusion are reported.

The theoretical part initially compares the experimental and the theoretical structural phase diagram. A set of ASYNNNI interaction potentials ($V_1, V_2, V_3$) is derived. Using this set of parameters, we predict various other structural and thermodynamic features and compare with the experiment. This section includes some work on how to treat the internal strain degrees of freedom, and comments on the 3-D registry of the low temperature phases.

The discussion part refers shortly to the impact of our data on other models. An attempt to explain some differences in reported data in the literature in terms of the cooling-history of the samples used in these experiments is given.

## 3.2 Experimental Technique: Neutron Diffraction and Gas Volumetry

### 3.2.1 Synthesis

The YBCO powder is prepared by standard solid state reaction technique based on oxides $Y_2O_3$ (Megon 99.999%), $BaO_2$ (Fluka 97 %) and $CuO$ (Ventron Alfa 99.9 %). The powder is reacted twice at 950°C for a total of 30 hours, with thorough intermediate grindings. No traces of impurities are observed from analysis of X-ray or neutron diffraction patterns of this powder. Resistivity measurements reveal that the powder - when fully oxidized - is superconducting with an onset temperature of 93 K and a transition width of 1 K. The grain sizes are analyzed by laser light scattering technique. Plotting the volume of the grains vs. the logarithm of their linear size the distribution is found to be rather flat with diameters ranging from 2 to 100 $\mu$m (10 % with diameters larger than 50 $\mu$m, and 10% with diameters smaller than 5 $\mu$m). Qualitative analysis using SEM confirms this distribution range, but residual sintering may have shifted the measured distribution towards larger diameters. From this powder a cylindrical sample of diameter 11.3 mm, height 28.8 mm and a density of 81% of the theoretical value is prepared.

### 3.2.2 Gasvolumetry

We use a gas volumetric technique based on the experimental setup shown in Fig. 8. A quartz sample tube is placed inside a furnace on a neutron powder diffractometer and connected via a capillary to a control panel consisting of valves, a gas reservoir, a pressure monitor and a turbo drag-pump. A water cooled aluminum furnace, with a tantalum foil kept under dynamic vacuum as heating element, is used for the measurements. The furnace has very fast response rates during heating and also during cooling down to 150 °C, where the relaxation times become larger than 15 minutes. The furnace is equipped with an alumel-cromel thermocouple placed inside the sample tube for temperature monitoring. Standard 99.7% oxygen gas is used. The gas pressure monitor is a MKS-Baratron, type 310B, with a resolution of 0.01 Torr and an accuracy of 0.08% of the reading. The turbo drag-pump has an ultimate pressure of $5 \cdot 10^{-6}$ mbar. The gas reservoir consists of a bulb of volume $V_0 = 337.6$ ml (valves V1 and V2 in Fig. 8 open) while the volume of the total system (valves V1, V2, and V4 open) is $V = 392.5$ ml. With this size of volume the variable amount of oxygen in the sample and in the reservoir are approximately equal at high pressures (760 Torr), while at low pressures (below 5 Torr) the amount of oxygen in the reservoir is below 1% of the sample amount. The gas volumetric equipment may - with a suitable smaller sample tube volume - equally well be used for studies and controlled annealing of $mm^3$-sized crystals.

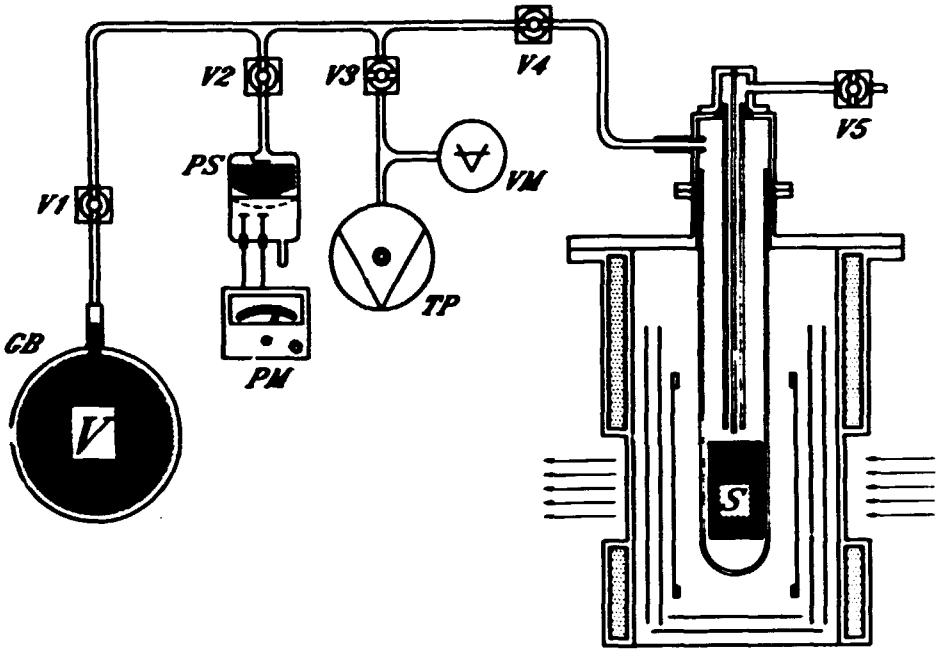


*Figure 8. Gas volumetric equipment for on-line pressure measurements on a powder neutron diffractometer. The sample (S) is mounted in a quartz tube in the neutron transparent furnace, and connected via a capillary to the gas reservoir (GB), pressure sensor/meter (PS/PM), and turbo-pump (TP) with vacuum meter (VM). V1 to V5 are valves.*

To evaluate the oxygen uptake $\Delta x$ of the superconductor the system is approximated by a two-volume model. The volume of a variable "hot zone" in the furnace, $V_s$, is at the variable temperature T, while the residual volume, $V - V_s$, is fixed at temperature $T_0$ (the total volume $V$ is also fixed). A straightforward application of the ideal gas law leads to the following expression

$$\Delta x = \frac{2VP_i}{NRT_0}\left(1 - \frac{P}{P_i}\left(1 + \frac{V_s}{V}\left(\frac{T_0}{T} - 1\right)\right)\right). \tag{33}$$

Here N is the number of moles of YBCO in the sample, $P_i$ the initial pressure and P the momentary pressure in volume $V$. To check the validity of Eq. 33 and find an expression for $V_s$ three calibration runs using inlet pressures of 25, 96, and 454 Torr are performed, decreasing the temperature in steps of 50 °C in each run from 725 °C to room temperature. An $Al_2O_3$ dummy sample of equal specific volume as our YBCO sample is used during the calibration. All three runs are satisfactorily approximated by Eq. 33 with a linear increase for $V_s$ : $V_s = 13.25 + 5.15 \cdot T/295$ ($V_s$ in ml and $T$ in Kelvin).

### 3.2.3 Neutron Diffraction

All neutron diffraction measurements are carried out on the multi-detector powder diffractometer at the DR3 reactor at Risø National Laboratory. The diffractometer has twenty detectors separated by 5.228°, giving a total of 2000 data points for standard one hundred instrumental settings. It is equipped with a germanium crystal of 1'' mosaicity as monochromator. To assure optimal resolution at large scattering angles, where the density of Bragg peaks becomes high, the monochromator scattering angle was selected to be close to 90°. The collimation between

reactor and monochromator, monochromator and sample, and sample and detector, is 60', 10' and 10', respectively. Diffraction data aiming at a full structure determination, to be used for a calibration of the absolute $x$ values, cf. below, are collected at room temperature without the use of a furnace, and with a neutron wavelength of $\lambda = 1.08$ Å, in order to access a large Q range. In this case the (7,1,1) reflection of the Ge monochromator is used. For studies of the structural phase diagram, where optimal resolution is required a wavelength of $\lambda = 2.32$ Å is used, corresponding to the Ge (3,1,1) reflection. For $Q < 3.0\AA^{-1}$ the resolution width (FWHM) is $0.013\AA^{-1}$. The wavelength calibration is done by full profile refinement to a standard $Al_2O_3$ powder scan using the EDINP profile refinement program [65]. The resolution at a scattering angle of $2\theta = 70°$ is found to be $\mathrm{FWHM}_{res} = 0.312°$, which is consistent with a theoretical model calculation of the resolution function.

Analysis of the powder diffraction patterns obtained in the furnace involved subtraction of a background profile by linear interpolation between 12 points. The background mainly reflects the diffuse scattering from the quartz sample tube. For the $\lambda = 1.08\AA$ data a full structural refinement is done using the EDINP profile refinement program. For the $\lambda = 2.32\AA$ data a special version of the program is used. It refines lattice constants $(a,b,c)$, zero angle offset, an additional angle - independent background, the profile parameters $(u,v,w)$, and independent Bragg peak intensities. The $(u,v,w)$ parameters result from a simultaneous fit to the peak widths (FWHM) of all the Bragg peaks in the diffraction pattern - weighted with their intensities - according to the equation:

$$FWHM_{uvw} = 2\sqrt{u\tan^2(\theta_i) + v\tan(\theta_i) + w}, \tag{34}$$

($\theta_i$ being the Bragg angle of reflection).

The refinements are carried out assuming orthorhombic symmetry and different start values for the $a$- and $b$-axes. When the difference $\Delta(ab)$ between the refined $a$ and $b$ becomes smaller than the experimental resolution, the structure is defined to be tetragonal. In practice, the phase transition temperature $T_\phi$ corresponds to the temperature above which $\Delta(ab)$ becomes independent of temperature. Test refinements above $T_\phi$ assuming tetragonal symmetry give essentially the same results and merit of fits as those carried out assuming orthorhombic symmetry.

### 3.2.4 Calibration of Absolute Stoichiometry

To calibrate the absolute stoichiometry a comparison is performed between four conventionally used techniques. A fully reduced sample is prepared by evacuating for four hours at 725 °C, and a fully oxidized sample similarly by annealing in pure oxygen at 450 °C for sixteen hours followed by slow cooling to room temperature ($60^0$ per hour). Iodiometric titration analysis and neutron diffraction measurements are performed on this set of samples. The results are compared with data on the maximum span in x-values at room temperature obtained from both weight measurements and gas volumetric measurements (difference between the pressure values of trace no. 1 and no. 16, cf. Fig. 9). The same sample is used throughout. The calibration results are listed in Table 1, while the results of the full structure refinement of the neutron diffraction data are given in Table 2. The agreement between the results from the various measurements are reasonably good. The adopted values are $x = 0.15(2)$ for the fully reduced sample and $x = 0.92(2)$ for the fully oxidized sample. With these uncertainties, the accuracy of our x-data are comparable to the degree of homogeneity in the sample.

| | $x$(oxidized) | $x$(reduced) | $\Delta x$ |
|---|---|---|---|
| Neutron diffraction | 0.89(3) | 0.18(3) | 0.71(6) |
| Iodiometric titration | 0.903(5) | 0.194(5) | 0.71(1) |
| Gas volumetry | | | 0.77(1) |
| Weight measurements | | | 0.79(1) |

*Table 1. Determination of the oxygen stoichiometry parameter $x$ in $YBa_2Cu_3O_{6+x}$ on an absolute scale. Comparison is made between results from four different experimental techniques using the same sample throughout. Oxidized and reduced refer to room temperature measurements on a fully oxidized and a fully reduced sample, respectively. $\Delta x$ is the difference between the measured values for these two cases. For details on synthesis and annealing refer to the text. Adopted values: $x$(reduced) = 0.15(2), $x$(oxidized) = 0.92(2).*

| Sample | Atom | Occupancy | $x$ | $y$ | $z$ | $B$ |
|---|---|---|---|---|---|---|
| $YBa_2Cu_3O_{6.89}$ | Y | 1 | 0.5 | 0.5 | 0.5 | 0.31(6) |
| 298 K | Ba | 2 | 0.5 | 0.5 | 0.1833(4) | 0.71(7) |
| $a$=3.8186(2) | Cu(1) | 1 | 0 | 0 | 0 | 0.57(7) |
| $b$=3.8843(2) | Cu(2) | 2 | 0 | 0 | 0.3549(3) | 0.54(5) |
| $c$=11.6777(8) | O(2) | 2 | 0.5 | 0 | 0.3774(5) | 0.90(8) |
| $x$=0.89(2) | O(3) | 2 | 0 | 0.5 | 0.3780(5) | 0.84(8) |
| $R_w$=11.6% | O(4) | 2 | 0 | 0 | 0.1608(4) | 0.80(8) |
| $R_{wexp}$=8.3% | O(1) | 0.78(2) | 0 | 0.5 | 0 | 0.69 |
| | O(5) | 0.11(1) | 0.5 | 0 | 0 | 0.69 |
| $YBa_2Cu_3O_{6.18}$ | Y | 1 | 0.5 | 0.5 | 0.5 | 0.44(7) |
| 298 K | Ba | 2 | 0.5 | 0.5 | 0.1957(4) | 1.01(10) |
| $a$=3.8581(2) | Cu(1) | 1 | 0 | 0 | 0 | 1.15(9) |
| $c$=11.8115(9) | Cu(2) | 2 | 0 | 0 | 0.3607(3) | 0.48(4) |
| $x$=0.18(3) | O(2) | 4 | 0.5 | 0.5 | 0.3786(5) | 0.84(5) |
| $R_w$=15.1% | O(4) | 2 | 0 | 0 | 0.1556(4) | 0.80 |
| $R_{wexp}$=10.7% | O(1) | 0.18(3) | 0.5 | 0.5 | 0 | 0.70 |

*Table 2. Structural parameters for a fully oxidized and a fully reduced sample of YBCO obtained by EDINP profile refinement to neutron powder diffraction data. $R_{wexp}$ and $R_w$ are the least squares residuals expected and obtained from the full powder profile refinement, respectively. Isotropic B-factors for O(1), O(4) and O(5), were fixed at values determined from Jorgensen et al.'s anisotropic temperature parameters [5].*

### 3.2.5 Series of Measurements

Sixteen traces in $(x,T)$-space are mapped out with simultaneous measurements of structural data (neutron powder diffraction scans) and oxygen partial pressures. The trajectories of these are given as thin curves in Fig. 9. The structural data are obtained from powder neutron diffraction measurements at approximately 22 temperatures along each trace, starting at 725 °C and ending at room temperature. The temperature steps are 22 °C close to the estimated phase boundaries and 45 °C elsewhere. After each 22 °C or 45 °C quench a 17 minite break is allowed for temperature equilibration. The diffraction measurements themselves take 75 minutes. Each of the traces are initiated by evacuating the sample for four hours at 725°C. This procedure is found to give a highly reproducible fixpoint in $(x,T)$-space, with an uncertainty in the oxygen content of $\Delta x \leq 0.003$. Then the pump

is disconnected and a controlled amount of oxygen let into the oxygen reservoir (volume $V_0$) and subsequently allowed to flow into the sample tube (expansion to volume $V$). A waiting time of 60 minutes is sufficient to assure pressure equilibrium is established before the first scan. The sixteen traces are performed in randomized order. They span an interval in equilibrium partial pressure from 0.5 Torr to 636 Torr. The inlet pressure $P_i$ in volume $V$, to be used in Eq. 33 for calculation of oxygen stoichiometries, is derived from the actual inlet pressure in volume $V_0$ by multiplication with $V_0/V$. Values of $P_i$, equilibrium pressures $P_{725}$ and $P_{25}$, and oxygen stoichiometries $x_{725}$ and $x_{25}$ at 725 °C and 25 °C, respectively, corresponding to the values at the beginning and the end of each of the traces, are given in Table 3.

| Trace | $P_i$(Torr) | $P_{725}$(Torr) | $x_{725}$ | $P_{25}$(Torr) | $x_{25}$ |
|---|---|---|---|---|---|
| 1 | 2.41 | 2.55 | 0.146 | 0.47 | 0.150 |
| 2 | 16.83 | 5.82 | 0.170 | 0.69 | 0.180 |
| 3 | 35.04 | 11.76 | 0.195 | 1.59 | 0.212 |
| 4 | 70.29 | 20.95 | 0.245 | 1.53 | 0.280 |
| 5 | 106.33 | 29.08 | 0.295 | 1.49 | 0.346 |
| 6 | 134.32 | 44.29 | 0.321 | 1.77 | 0.398 |
| 7 | 157.13 | 61.46 | 0.336 | 2.49 | 0.443 |
| 8 | 181.41 | 79.05 | 0.351 | 3.81 | 0.486 |
| 9 | 205.52 | 87.49 | 0.375 | 4.64 | 0.525 |
| 10 | 245.63 | 128.67 | 0.376 | 4.82 | 0.600 |
| 11 | 283.44 | 161.16 | 0.394 | 5.83 | 0.675 |
| 12 | 324.99 | 179.47 | 0.433 | 8.37 | 0.741 |
| 13 | 358.72 | 215.12 | 0.451 | 11.67 | 0.807 |
| 14 | 455.70 | 297.42 | 0.451 | 53.23 | 0.900 |
| 15 | 788.87 | 635.42 | 0.478 | 375.20 | 0.918 |
| 16 | 863.18 | 892.86 | 0.481 | 636.25 | 0.922 |

*Table 3. The inlet pressure $P_i$, and the equilibrium oxygen pressure and stoichiometry at 725 °C and 25 °C, corresponding to the start and end values for the sixteen traces in $(x,T)$-space shown in Fig. 9.*

During the neutron diffraction measurements the pressure and the sample temperature are monitored for all 100 settings of the spectrometer. In this way the decay rate of the oxygen partial pressure, and therefore the relaxation time for bulk oxygen in-diffusion, may be determined and used to evaluate whether equilibrium has been reached. Results of these studies will be presented later on.

It is important to realize that local equilibration of the oxygen configuration, e.g. after a small change of temperature, will be faster than global equilibration with respect to in-diffusion of particles from the surfaces. Hence, the set-up has been optimized to ensure operation at (nearly) constant $x$-values at low temperatures - no in-diffusion, vertical traces - while in-diffusion in reasonable quantities takes place at higher temperatures. In the latter case, the in-diffusion rate provides valuable additional information without the danger of slowing down kinetics.

## 3.3 Experimental Results

### 3.3.1 The Structural Phase Diagram

The structural phase diagram of YBCO is established from an analysis of the 350 sets of diffraction scans taken along the trajectories of the sixteen traces in $(x,T)$-space shown in Fig. 9. All data are well accounted for by single phase

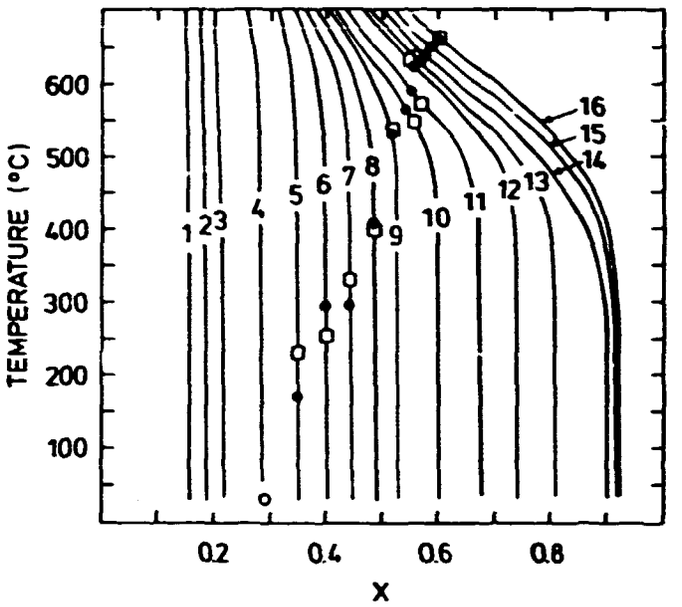


*Figure 9. The structural phase diagram of YBCO. Trajectories of the sixteen experimental traces in $x$ vs. temperature space are given as thin lines. Solid circles are experimental values from neutron powder diffraction data of the transition line separating the tetragonal and orthorhombic phases. The open circle for trace no. 4 is the extrapolated $x$-value where the orthorhombic distortion disappears at room temperature. The squares marks the transition line as infered from the peak broadening due to twin domain formation.*

refinements. The transition temperatures, $T_o$, separating the tetragonal phase at high temperatures from the orthorhombic phase(s) at low temperatures are given in the figure as filled circles. Typical uncertainties in the transition temperatures are ±40°C. For traces nos. 1-4 no orthorhombic splitting is observed. For trace no. 4 measurements are carried out down to 10 K, but no significant broadening is observed during cooling. None of the spectra contains superlattice peaks which could be used to distinguish between different orthorhombic phases.

The structural data of the lattice parameters $c$, $a$ and $b - a$ are displayed as contour plots in Fig. 10. The contour lines are found by a linear interpolation to nearest neighbours in the 350 data sets using a regular grid. No smoothing is performed. For reference purposes the room temperature lattice parameters are also reproduced in Fig. 10. The uncertainty in terms of absolute and relative oxygen stoichiometry is 0.02 and 0.01, respectively. From these two figures we may extrapolate the $x$ value at which the orthorhombic distortion disappears at room temperature: $x = 0.28(2)$. This point is markes as an open circle in Fig. 9. Based on our structural data in Fig. 10 we derive a volume thermal expansion coefficient which is approximately independent of both $x$ and $T$ and has a value of $43(3) \times 10^{-6} K^{-1}$.

One should note, that the traces in $(x,T)$-space becomes nearly vertical below approximately 400 °C (cf. Fig. 9). This reflects the low equilibrium oxygen pressure at such temperatures, which gives a large change in the chemical potential of the molecular gas outside the sample with the number of particles, compared to the changes in the chemical potential of the atomar oxygen gas in the superconductor with the same number of particles. Hence, when the temperature is abruptly decreased by, say 45 °C, a small number of in-diffusing particles is suf-

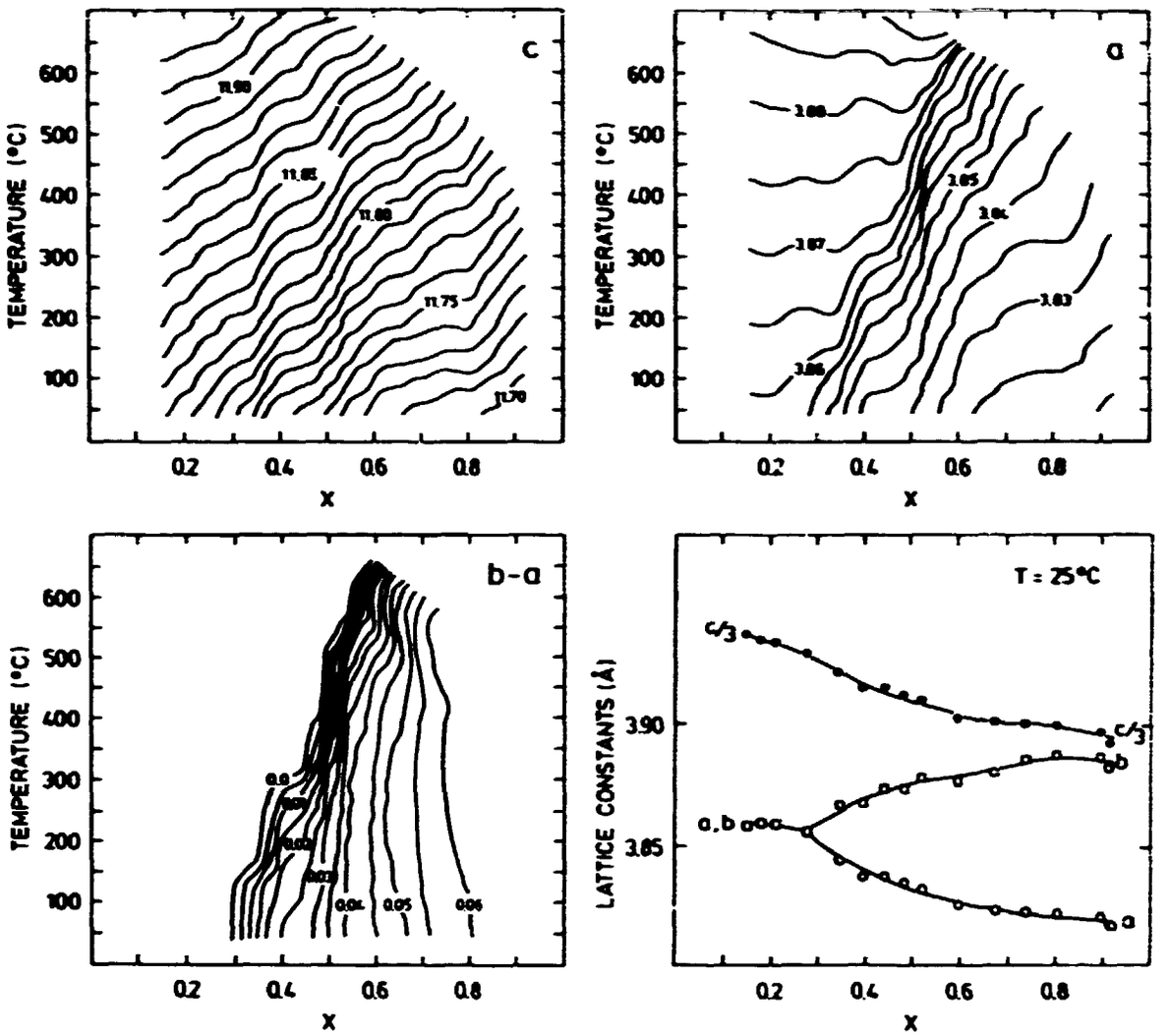


*Figure 10. YBCO lattice parameters: c, a, and b − a are shown in the three first figures. The contour lines Å are made from interpolation between the 350 points taken along the trajectories shown in Fig. 9. The relative and absolute uncertainty in x is $\Delta x = 0.01$ and $\Delta x = 0.02$, respectively. For reference the room temperature lattice constants, a, b and c/3 are given in the fourth figure.*

ficient to establish equilibrium. Thus we are effectively lowering the temperature at constant x-values. This decouples the slow in-diffusion process, and the equilibrium relaxation time is determined by the much faster internal redistribution processes. This decoupling is essential for achieving equilibrium properties at low temperatures.

### 3.3.2 The Broadening of the Bragg Peaks

In order to search for multi-phase structures, possibly related to first order phase transitions, and to study micro-domain properties we analyze selected Bragg peak broadenings for all the neutron powder diffraction scans. These data also provide important information on the homogeneity of oxygen concentration in the sample.

Least square fits to Gaussian profiles are performed for some selected peaks: the (004), (113), (200) and (020) reflections. Due to problems of overlapping Bragg

peaks the in-plane reflections (200) and (020) cannot be fitted at all temperatures and concentrations. The peaks width, FWHM, of the (113) and (004) reflections are found to be independent of temperature and oxygen concentration, with values FWHM = 0.33°(2) and FWHM = 0.330°(15), respectively (to be compared with the experimental resolution width of 0.312°). The lack of peak broadening of the (004) peaks combined with the variation of the c axis with oxygen stoichiometry (cf. Fig. 10) gives an upper limit on the degree of inhomogeneity in the sample: $\Delta x < 0.05$. In contrast to the out of plane peaks, the in-plane reflections reveal large variations as exemplified by the temperature dependency of the peak widths in traces nos. 7, 8, and 12 shown in Fig. 11. There is no qualitative difference between the behaviour of the (200) and (020) reflection. The room temperature values of both the out of plane and the in-plane reflections are given for the various traces in Table 4.

From the analysis of individual Bragg peaks we conclude that only the peaks corresponding to the (hk0) reflections show observable broadenings. In order to get better statistics, we will switch the focus to an analysis of the weighted mean peak broadening of all peaks, $FWHM_{ave}$, as it appears in the profile parameters (u, v, w), cf. Eq. 34. The very large intensity of the (200) and (020) powder peaks indicates that this pair of reflections will give rise to the major contributions to $FWHM_{ave}$. The variations of $FWHM_{ave}$ will therefore predominantly reflect the variations of the widths of the (200) and (020) peaks. The (u, v, w) parameters are known at all temperatures and x-values with good accuracy from the EDINP refinements. The temperature dependence of the $FWHM_{ave}$'s evaluated according to Eq. 34 is shown in Fig. 12 for twelve of the traces. For $\theta$ the value $\theta = 35°$ is selected because it represents the center of mass of integrated peak intensity versus scattering angle as well as being approximately the scattering angle for the (020) reflection. Similar plots with other $\theta$ values exhibits the same overall features. The shape of the graphs in Fig. 12 are well described by two constant levels corresponding to orthorhombic and tetragonal phase, separated by an intermediate zone. Traces nos. 2 and 4 (and 1 and 3) contain only one level corresponding to the tetragonal phase. The temperature mid-points of the intermediate zones are presented as open squares in Fig. 9. The good agreement between these temperatures and the transition temperatures, $T_\phi$, determined by analyzing the lattice parameters indicate that the peak broadening is associated with the structural phase transition from tetragonal to orthorhombic symmetry. The levels of the orthorhombic phases (temperature averaged $FWHM_{ave}$ at $\theta = 35°$) are listed in Table 4 for traces nos. 5 to 16. For the purely tetragonal traces nos. 2 and 4 the average values determined in the entire temperature range have been added.

The results of the peak width analysis are consistent with an assumption that the peak broadening results from twin domain formation in orthorhombic YBCO, and that the size of the twin domains 'freezes' at a temperature near $T_\phi$. In consequence, we can interpret the $FWHM_{200}$ data given in column four of Table 4 in terms of an in-plane correlation length, $\zeta$, related to twin domain sizes by deconvoluting with a Gaussian resolution function of half-width $FWHM_{res} = 0.312°$. The results obtained for $\zeta$ are given in the last column of Table 4. The room temperature (200) peak widths are plotted versus oxygen stoichiometry in Fig. 13. The figure suggests a grouping of the peak widths according to three intervals of oxygen concentration. First an interval $0.15 < x < 0.30$ (traces nos. 1 to 4), corresponding to the tetragonal phase, with inherent small isotropic broadenings. Next two intervals corresponding to orthorhombic structural symmetry: $0.30 < x < 0.50$ (traces nos. 6 to 8) and $0.50 < x < 0.92$ (traces nos. 9 to 16). The peak widths, and therefore the twin domain sizes are approximately constant as function of $x$ within each of the three intervals. The adopted values for the two orthorhombic intervals are 250 Å and 350 Å, respectively.

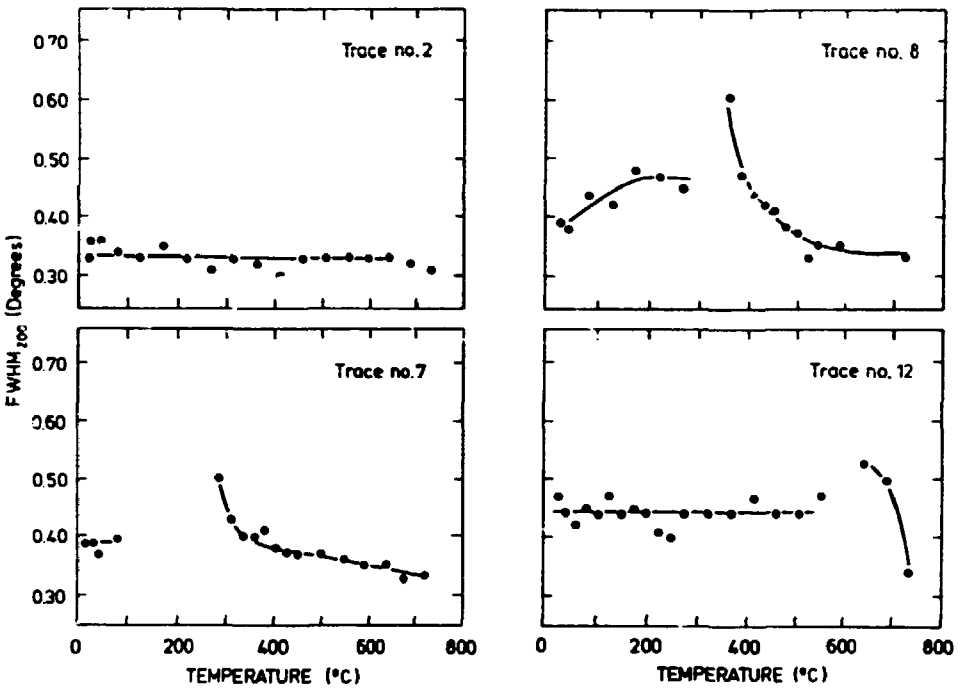


*Figure 11. Peak widths (FWHM) of the tetragonal (200) and the orthorhombic (200)/(020) reflections (o), determined from least square Gaussian fits to neutron powder diffraction peaks. The trajectories in (x,T)-space for the four traces (nos. 2, 7, 8, 12) are shown in Fig. 9. The solid curves are guides to the eye.*

### 3.3.3 The Equilibrium Oxygen Partial Pressure

The data for the oxygen equilibrium partial pressure P are presented in Fig. 14 as isotherms. The contour lines are made using a linear interpolation to nearest neighbours in the 350 data sets using a regular grid. No smoothing is performed. The room temperature isotherm is found to be almost indistinguishable from the 100 °C contour. Due to the small impurity of 0.3 % of the oxygen gas and possibly a little degassing from the quartz-tube the data become unreliable for very small oxygen pressures. The dotted line in Fig. 14 represents this limit on the validity of the data.

There are three significant features which should be noticed in Fig. 14. Firstly, the closely lying isotherms and isobars around $x \approx 0.9$ which indicate that $x = 0.92(2)$ is the maximum concentration that may be obtained at pressures below 760 Torr, or alternatively that the kinetics becomes very sluggish above this concentration. Secondly, a jump in the pressure is observed in the low temperature isotherms at $x = 0.48(2)$. Finally anomalous behaviour is reflected in the isothermal data for $.20 < x < 0.25$. From a preparation point of view our pressure data show that it should be possible to prepare fully oxidized samples by quenching from 400 °C in air.

The chemical potential of the oxygen molecular gas, $\mu(O_2)$, can be calculated on basis of the equilibrium partial pressures by applying standard formulas for an ideal gas with a generalized expression for the specific heat $C_p$ : $C_p = n(A + BT + CT^2)$, where $T$ is the absolute temperature and $n$ the number of moles of molecular oxygen:

$$\mu(O_2) = G_0 - (S_0 - A)(T - T_0) - AT\ln(T/T_0) + RT\ln(P/P_0) \qquad (35)$$

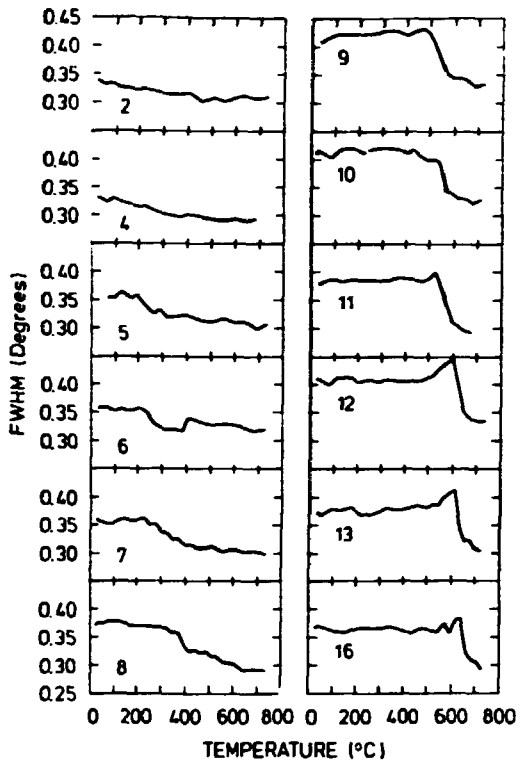


*Figure 12. The temperature dependence of the peak widths ($FWHM_{uvw}$) for twelve of the sixteen traces in $(x,T)$-space shown in Fig. 9. The graphs for traces nos. 1,2 and 3, as well as for traces nos. 14, 15 and 16 are almost identical. $FWHM_{uvw}$ has been calculated from the refined values of the profile parameters $u, v$, and $w$, determined from the full neutron powder diffraction pattern, using Eq. 34 and a Bragg angle of $\theta = 35°$.*

$$-B(T-T_0)^2/2 - C(T-T_0)^2/(2TT_0^2). \tag{36}$$

Here R is the gas constant, $G$ is the Gibbs free energy, $G_0$ its specific value at ambient temperature ($T_0$) and ambient pressure ($P_0$), and $S_0$ the entropy at $(T_0, P_0)$. Using values from Barin and Knacke [66] we have $A = 7.16, B = 1.00 \cdot 10^{-3}, C = -0.40 \cdot 10^5, S_0 = 49.005$ - all in units of cal/(mol K) - and $G_0 = -14.611$ kcal/mol.

The full Hamiltonian for the superconductor may be written in the following form that allows for direct comparison with various two dimensional models of oxygen ordering in the material:

$$H = V_0 \sum_i \sigma_i + \sum_{ij} V_{ij}\sigma_i\sigma_j + E_b + E_{ph}, \tag{37}$$

where $E_b$ is the binding energy of $YBa_2Cu_3O_6$, $V_0$ the additional single site energy appearing in relation to introduction of an oxygen in the basal plane, $\sum_{ij} V_{ij}\sigma_i\sigma_j$ the pair-interaction Hamiltonian, e.g. the ASYNNNI Hamiltonian, and $E_{ph}$ the total contribution from the phonons in the material to the Hamiltonian. All terms may be concentration and temperature dependent. Defining $\mu_{2D}$ to be the derivative of the pair-interaction Hamiltonian with respect to the number of particles in the material N, we have for the equilibrium state

$$\mu(O_2)/N_A = 2(\mu_{2D} + V_0 + \frac{\partial E_{ph}}{\partial N}) - E_d. \tag{38}$$

| Trace | Conc. $x_0$ | Full width half maximum (FWHM) | | | | Correlation length |
|---|---|---|---|---|---|---|
| | | (004) | (113) | (200) | (uvw) | $\zeta$(Å) |
| 2 | 0.180 | 0.32(1) | 0.31(1) | 0.33(1) | 0.330(5) | 775(300) |
| 4 | 0.280 | 0.33(1) | 0.31(1) | 0.35(1) | 0.332(6) | 525(100) |
| 5 | 0.346 | 0.31(1) | 0.32(1) | | 0.356(5) | |
| 6 | 0.398 | 0.30(2) | 0.33(1) | 0.40(1) | 0.353(3) | 330(25) |
| 7 | 0.443 | 0.32(1) | 0.33(1) | 0.39(1) | 0.354(5) | 355(35) |
| 8 | 0.486 | 0.35(2) | 0.32(1) | 0.39(1) | 0.366(10) | 355(35) |
| 9 | 0.525 | 0.34(2) | 0.32(1) | 0.45(1) | 0.423(7) | 255(10) |
| 10 | 0.600 | 0.33(2) | 0.33(1) | 0.46(1) | 0.410(8) | 245(8) |
| 11 | 0.675 | 0.35(1) | 0.32(1) | 0.45(1) | 0.386(5) | 255(10) |
| 12 | 0.741 | | 0.33(1) | 0.46(1) | 0.411(10) | 245(8) |
| 13 | 0.807 | 0.32(2) | 0.35(1) | 0.45(1) | 0.380(13) | 255(10) |
| 16 | 0.922 | 0.30(2) | 0.33(1) | 0.44(1) | 0.365(8) | 265(15) |

*Table 4. Analysis of Bragg peak broadening from room temperature neutron powder diffraction data. The numbers in the first coulomn refers to the experimental traces presented in Fig. 9. The second coloumn gives the oxygen concentration. The FWHM for the (004)-, (113)- and (200)-reflections listed in coloumns 3 to 5 are the peak widths in degrees of the associated Bragg peaks. The FWHM marked (uvw) - in coloumn 6 - are calculated according to Eq. 34 at $\theta = 35°$ - it constitutes a weighted mean of all peaks (see text). The values in coloumn 6 are those pertinent to the tetragonal phase (trace nos. 2 and 4) or the orthorhombic phases (trace nos. 5 to 16), respectively. The instrumental resolution width near (200) is 0.312°. The data are used to determine average twin domain sizes. The corresponding in-plane correlation lengths, $\zeta$, determined from the (200) data, are listed in the last coloumn.*

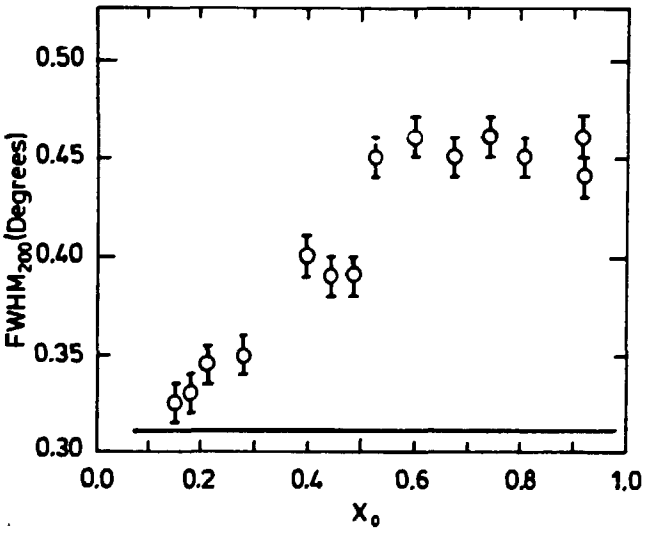


*Figure 19. The room temperature peak width (FWHM) of the tetragonal (200) and orthorhombic (200)/(020) reflections, determined from least square Gaussian fits to the neutron diffraction peaks. Peak widths are plotted versus oxygen stoichiometry x. The experimental resolution $FWHM_{res} = 0.312°$ is shown as a solid horizontal line.*

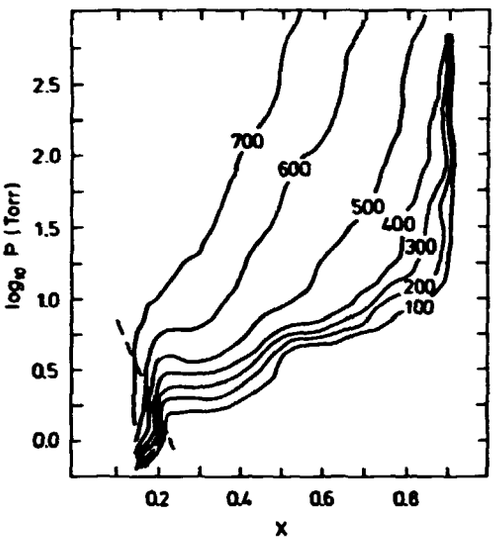


*Figure 14. Oxygen equilibrium partial pressures shown as isotherms in °C. Data taken below the dotted line are of limited validity due to impurities of the oxygen gas.*

The chemical potential $\mu(O_2)$ is in this context defined as the derivative with respect to the number af molecules, not the number of moles; hence the factor $N_A$. $E_d$ is the dissociation energy of one oxygen molecule. Estimating $\mu_{2D}$ from simulations, important information on the temperature and concentration dependency of observable $V_0 + \frac{\partial E_{pA}}{\partial N}$ can be achieved ($E_d$ is tabulated). Subtracting the phonon contribution using specific heat and neutron diffraction data, we may actually determine the single site potential (the internal stress) with a reasonable degree of accuracy. We will return to this question.

### 3.3.4 Diffusion

The oxygen in-diffusion process is monitored during each neutron powder diffraction scan by measuring the pressure relaxation. Thus we sample the pressure 100 times in the time window between approximately 17 minutes and 95 minutes after a 22°C or 45°C quench. The furnace is sufficiently fast above 150°C, that for all purposes we may think of the quench and the thermal relaxation process in the sample as instantaneous. Several test traces with the sample removed are performed. They reveal a small leak and/or degassing from the quartz tube, that only influences our data for very small oxygen partial pressures.

In appendix A a field theoretical approach is given to the physics of in-diffusion in the present gasvolumetric set-up. It is assumed, that the diffusion process is governed by the bulk behaviour (no slowing down due to surface barriers). This assumption will be justified experimentally in this section. The diffusion process will then be driven solely by the gradients in the total internal chemical potential $\mu_{int} = \mu_{2D} + V_0 + \frac{\partial E_{pA}}{\partial N}$. The constraint that the chemical potential at the surface at all times should be equal to the instantaneous chemical potential of the ideal gas outside, effectively means that $\mu_{int}$ will rise during the equilibration process, while $\mu(O_2)$ decreases. This complicates the description, and unless the experiments are run under conditions that allow for approximations of the resulting differential equation, data analysis will be at best a very tedious endeavour. As shown in the appendix the differential equation may to a very good approxima-

tion be linearized and solved in a closed form provided two operating criteria are met. Firstly, the quenches should be performed in sufficiently small steps, effectively operating in a quasi-stationary mode. This criterion is generally met in the present case. Secondly, the number of moles of oxygen in the environment should be sufficiently high compared to the number of moles in the sample, that we can neglect the decreasing $\mu(O_2)$ during the in-diffusion process. A specific criteria for the validity of this simplification is established. Given the approximations, the resulting solution for the relaxation of the pressure $P = P(t)$ is

$$P(t) = P(0) + (P_1 - P_0)(1 - \alpha) \tag{39}$$

$$\alpha = \frac{8^2}{\pi^4} \sum_{m=1}^{\infty} \sum_{n=1}^{\infty} \frac{1}{(2m-1)^2(2n-1)^2} \exp(-(D_m^x(m-1/2)^2/L_x^2 + D_n^x(n-1/2)^2/L_y^2)4\pi^2 t) \tag{40}$$

where $D_m^x$ and $L_x$ is the mutual diffusivity and the sample dimension along the a-axis, respectively. Likewise, y-indices refer to the b-axis. $P_0$ and $P_1$ are the initial and final pressures, respectively. The diffusion along the c-axis is known to be $10^{-6}$ times slower than the in-plane diffusion [8], [67] and can therefore be completely neglected. Also the in-plane anisotropy is known to be sizeable [68], $D_m^x \neq D_m^y$. The equation above is valid for a single perfect twin-domain of YBCO.

Next, we can make a final simplification by keeping only the first harmonic in Eq. 40

$$P(t) = P(0) + (P_1 - P_0)\left(1 - \frac{8^2}{\pi^4} \exp(-\pi^2(D_m^x + D_m^y)t/L^2)\right). \tag{41}$$

As shown in the appendix, this approximation is perfectly valid provided we first start monitoring when the pressure has relaxed at least 30 % of its full value[7].

Experimentally, various combinations of power laws and exponentials are tested empirically. In general, we find that the pressure data $P = P(t)$ are well described by a simple exponential decay[8]:

$$P(t) = P_0 + \Delta P[1 - \exp(-t/\tau)]. \tag{42}$$

The amplitude $\Delta P$, and the time constant $\tau$ may be used as fitting parameters. An example of the merit of fit is given in Fig. 15. Analyzing our data in terms of more complex functions relevant for the rather broad grain size distribution gives fits that are less satisfactory. Hence, we conclude that the relevant diffusion lengths are determined by some intrinsic materials properties like micro-cracks, twin domain distributions, etc., and that these intrinsic properties apparently have a narrow size distribution.

Three groups of results have to be excluded from the data analysis. Firstly, all results related to scans below 150 °C because of insufficient cooling rate of the furnace at these temperatures. Secondly, results below 450 °C for trace no. 1 and below 400 °C for trace no. 2 because of poor statistics (the pressure differences are comparable to the noise level of the manometer). Thirdly, results taken at high temperatures and high partial pressures because the pressure is fully relaxed under these circumstances before the first pressure measurement takes place.

In order to ease comparison with other experiments (different densities, etc.) we will present the $(\tau, \Delta P)$ set of values obtained by use of Eq. 42 in terms of the in-diffusion flow J, of atomic oxygen through the surface. If we imagine a totally dense cylinder of YBCO with the c-axis parallel to the axis of the cylinder and a radius $r_1$ the in-diffusion flow through the cylindrical walls is:

[7] Experimentally one has the option to monitor either the last 70 % of the relaxation process as here, or alternatively the first 5-10 %. The latter can be approximated by a simple error-integral.

[8] For historical reasons the factor $(8/\pi^2)^2$ was set equal to 1 during the analysis of the data. None of the qualitative results reported below are affected by this error.

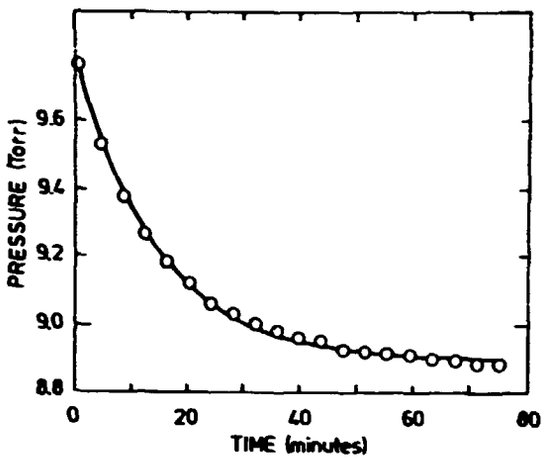


*Figure 15. A typical fit by a simple exponential decay rate (full line) to the pressure relaxation data (o). The data are taken from trace no. 10 at a temperature of 450 °C.*

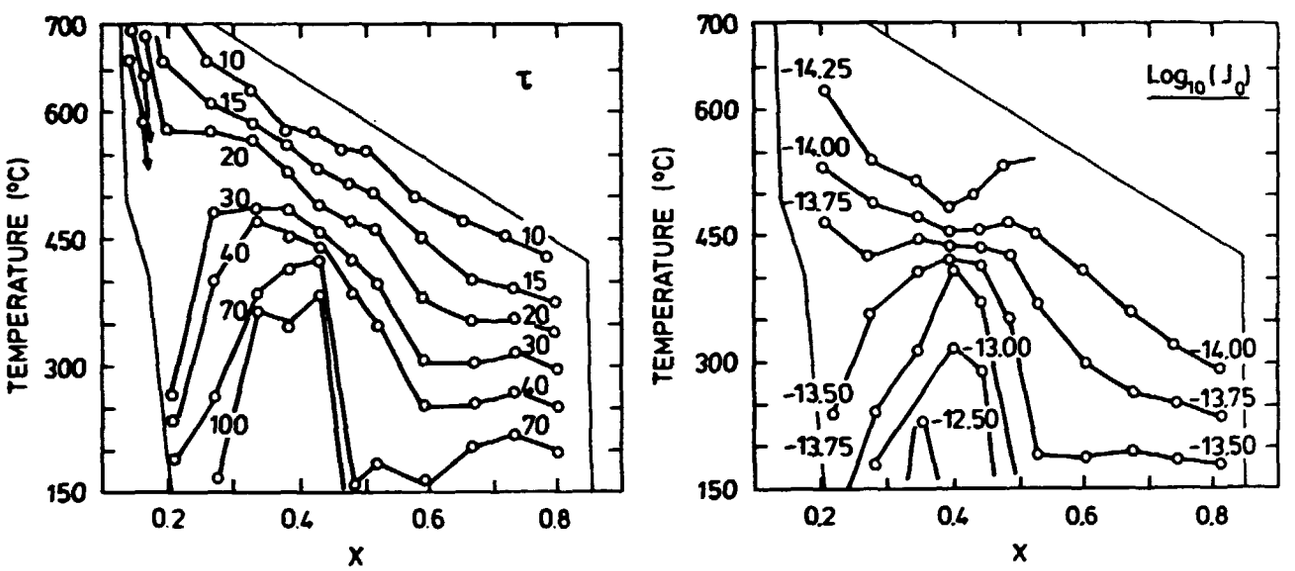


*Figure 16. Relaxation times $\tau$, and prefactors, $J_0$, of oxygen in-diffusion flow. $J = J_0 \exp(-t/\tau)$. The contour lines are determined by linear interpolation in pressure relaxation data measured along the trajectories of the sixteen traces shown in Fig. 9. The open circles mark the crossing of the contour lines and the trajectories. $\tau$ isochrones are in minutes, and $J_0$ in moles of atomic oxygen flowing through 1 cm$^2$ of sample surface per second. The $J_0$ values are calculated using a cylindrical unit-size model of radius 1 Å with no diffusion along the cylinder axis. The thin curves are boarder lines to regions in $(x,T)$-space where our experimental setup could not measure the pressure relaxation with sufficient accuracy.*

$$J = J_0 \cdot \exp(-t/\tau) \tag{43}$$

$$= 4.4 \cdot 10^{-13} \frac{\Delta P r_1}{\tau T} \exp(t/\tau) \frac{\text{mole}}{\text{cm}^2\text{s}} \tag{44}$$

with $\Delta P$ in Torr, $\tau$ in minutes, $T$ in Kelvin and $r_1$ in Å. Contour plots of $\tau$, and

$\log_{10}(J_0)$, with $r_1$ arbitrarily set to 1 Å, are given in Fig. 16. The borders to the groups of excluded results are marked by thin lines. Generally the contour lines of both $\log_{10}(J_0)$ and $\tau$ follow a $T\log_{10}(P)$ type behaviour at high temperatures, including the dip near $x = 0.22$ (cf. Fig. 14). For low temperatures (below 450 °C) there is a marked enhancement of both $J_0$ and $\tau$ in the interval $0.32 < x < 0.48$.

Examples of Arrhenius plots of $\tau$ for two of the traces are given in Fig. 17. At high temperatures we are generally able to fit the data to a first order polynomial: $\ln(\tau) = C + \Delta/kT$, if the tetragonal to orthorhombic phase transition is taken into account. However, traces nos. 1, 2, 14, 15, and 16 are not analyzed since data are too sparse. The resulting activation energies are plotted versus the final x values of the traces in the insert of Fig. 17, and the activation energies, $\Delta$, as well as the prefactors, $C$, are given in Table 5. Both the prefactor and the activation energies can within the uncertainties be taken as constants in each of the two phases. The adopted activation energies are 0.55 eV and 0.25 eV in the tetragonal and the orthorhombic phase, respectively. Below a certain temperature, $T_{Arrh}$, deviations from the Arrhenius behaviour evolve. After a transition region of approximately 100 K, $\tau$ approaches a constant level. The onset temperatures, $T_{Arrh}$, are also listed in Table 5. It should be mentioned that trace no. 3 does not fit into the pattern presented above. For this trace the non-Arrhenius behaviour is present at all temperatures. Actually, as is evident from Fig. 16 the diffusion becomes much faster near $x = 0.20$.

To account for the cut-off temperatures $T_{Arrh}$, we analyzed the pressure relaxation data for the temperature closest to $T_{Arrh}$ within each trace. At these particular temperatures the pressure relaxation achieved when the monitoring begins P(17) are found to be related to the total difference in pressure $\Delta P$ by $(P(17) - P(\infty))/\Delta P = 0.75(5)$ for all traces. As described in appendix A, the single harmonics approximation is theoretically known to be break down when analyzing data related to the first 30 % of the relaxation process measured in absolute terms. This coincidence is highly suggestive that the prominent kinks in the Arrhenius plots are due to an over-simplified analysis at low temperatures.

The $\tau = 70$ min isochrone is positioned at approximately the same temperature as $T_{Arrh}$. Below this isochrone in the phase diagram, the sample does not fully reach equilibrium with respect to in-diffusion, because the total duration of one diffraction scan and one break between scans is 95 minutes. However as mentioned several times, because of the decoupling of in-diffusion at low temperatures (the nearly vertical traces in (x,T)-space in Fig. 9) that also takes place around the $\tau = 70$ min isochrone, near equilibrium properties may actually be prominent down to about 150°C for all traces.

Based on these arguments we reason that the results for the structural phase diagram and the oxygen partial pressure corresponds to near equilibrium data for temperatures down to 150 °C. We refrain from extracting absolute values from the pressure relaxation data below $T_{Arhh}$, but feel free to do qualitative comparisons for all temperatures above 150 °C.

## 3.4 Results of Monte Carlo Simulations of the ASYNNNI Model

As discussed elsewhere we have chosen to analyze the experimental data in terms of the simple ASYNNNI model for oxygen ordering, Eq. 3. In order to perform quantitative comparisons a series of Monte Carlo simulations is performed, and will be presented below. To maintain a coherent presentation, and be able to draw more general conclusions, we will in some cases include additional experimental work from the litterature in our discussion. A clear description of these experiments is

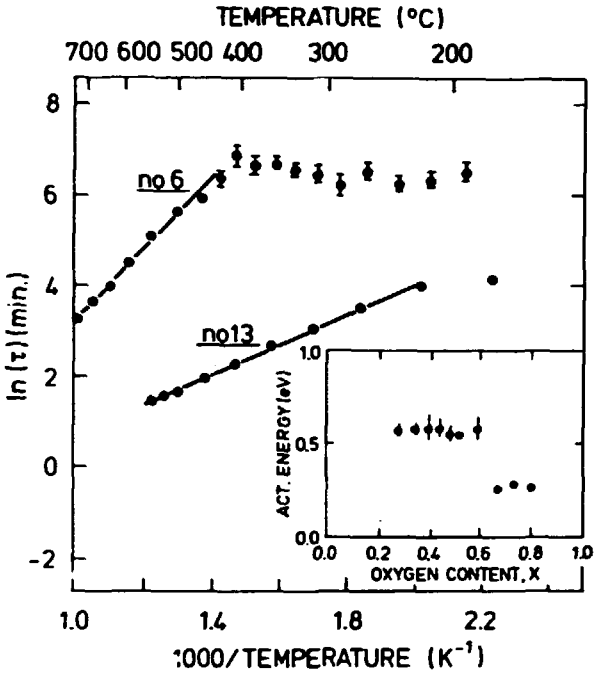


*Figure 17. Arrhenius plot of the bulk oxygen in-diffusion relaxation times, $\tau$, measured along the traces nos. 6 and 13 shown in Fig. 9. Activation energies obtained at high temperatures for all the traces are shown in the insert. The two levels of activation energies may be related exclusively to the tetragonal (0.55 eV) and the orthorhombic (0.25 eV) phases.*

| Trace | $x_0$ | $\Delta$ (eV) | C (ln(min)) | $T_{Arrh}$ (K) |
|---|---|---|---|---|
| 4 | 0.280 | 0.57(4) | -4.1(4) | 820 |
| 5 | 0.346 | 0.58(4) | -3.4(4) | 770 |
| 6 | 0.398 | 0.59(7) | -4.4(7) | 695 |
| 7 | 0.443 | 0.59(5) | -4.4(5) | 630 |
| 8 | 0.486 | 0.56(4) | -4.4(5) | 680 |
| 9 | 0.525 | 0.55(3) | -3.8(4) | 550 |
| 10 | 0.600 | 0.58(7) | -4.5(10) | 450 |
| 11 | 0.675 | 0.26(1) | -2.0(1) | 500 |
| 12 | 0.741 | 0.29(1) | -2.3(1) | 520 |
| 13 | 0.807 | 0.26(1) | -2.1(1) | 490 |

*Table 5. Diffusion activation energies, $\Delta$, and prefactors, C, for the experimental traces shown in Fig. 9. These are found from Arrhenius fit to the pressure relaxation time $\tau$: $\ln(\tau) = C + \Delta/k_BT$, where $T$ is absolute temperature. Results for traces nos. 4-10 are from fit to data in the tetragonal phase, while nos. 11-13 are from fit to data in the orthorhombic phase. $x_0$ corresponds to the final oxygen content (room temperature) of the traces. $T_{Arrh}$ denotes the temperature below which non-Arrhenius behaviour starts to develop, due to an over-simplified data-analysis. The uncertainties in $T_{Arrh}$ are approximately 100 K.*

given either here or in the experimental review in chapter 2. The simulation technique is in most cases based on standard Metropolis algorithms with Glauber or Kawasaki dynamics. An introduction to these algorithms, including a description of technical problems to take into consideraton, is given in chapter 2. Hence, we will in most cases refrain from a (rather tedious) listing of the tests performed to assure that the results represent equilibrium, are size-independent, robust to various interaction parameters, etc.

This section will also contain some comments on how to incorporate the internal strain in the theoretical models. We will concentrate on simple qualitative observations mostly related to the influence of the twin-domains on the low-temperature structural behaviour. Various more elaborate models are at the moment under investigation.

### 3.4.1 The Structural Phase Diagram

The Ortho-II super-structure is not detected at any point during our experiment. However, there are very strong arguments - some to be presented below - for believing that the Ortho-II phase is present. Most likely, the structural coherence length of the phase is too small, especially along the c-axis, to be detected in powder diffraction experiments. Thus, if we compare with the recent single crystal neutron diffraction observation of the phase by Zeiske et al. [15], it is characteristic that they find diffuse peaks, with intensities six orders of magnitudes smaller than the Bragg peaks. Such a resolution can never be achieved in a powder experiment. We will return to this question.

Initially, we will propose a criteria for whether the ASYNNNI model matches the experimentally observed structural phase diagram or not, which is independent of the size of the interaction parameters. Hence, assume the Ortho-II structure is present, and the multiple point, the vertex between the T, OI and OII phases, is situated well above room temperature in the phase diagram, cf. Fig. 4. Then the structural phase transition will take place at an oxygen concentration, $x_\phi$, that is nearly independent of temperature and interaction parameters and equal to $x_\phi \approx x_\phi(T=0) = 0.25$ for $T \lesssim 300$ K. This prediction should be compared with the experimentally determined value of $x_\phi = 0.28(2)$, cf. Fig. 10. To go a little further, we may for the moment consider the TEM measurements by Reyes-Gasga and coworkers [19],[20] and Beyers et al. [18]. Their cooling-rates are almost identical to the ones used here. In both cases the authors report on room temperature detection of faint spots at $(\frac{1}{2},0,0)$ in reciprocal space between $x \approx 0.28$ and $x \approx 0.65$. Again, this should be compared with the $T=0$ theoretical span $0.25 < x < 0.75$. At room temperature we would expect the span to be sligtly smaller. The reasonable agreements in both cases are strong indications, that the ASYNNNI model might be a relevant frame-work for theoretical studies.

To proceed, we need *ab initio* calculations of the interaction parameters. Only one set of such first principles parameters is reported in the literature. They are due to the LMTO band structure calculations performed by Sterne and Wille [32], with resulting values $V_1 = -375.2$ meV, $V_2 = 130.4$ meV and $V_3 = -60.0$ meV. Using this set Hilton et al. [69] mapped out the phase diagram employing Monte Carlo and Transfer Matrix calculations. The resulting theoretical phase diagram is compared with our experimental data-points in Fig. 18.

The agreement between the two set of data in Fig. 18 is reasonable. Originally, Ceder et al. [33] had performed a analogous calculations using a CVM technique and found an even better agreement, but this was soon realized to be a fortuitous coincidence, due to the fact that CVM models overshoot transition temperatures with up to 20 % in the present case. There is a definite need to do more first

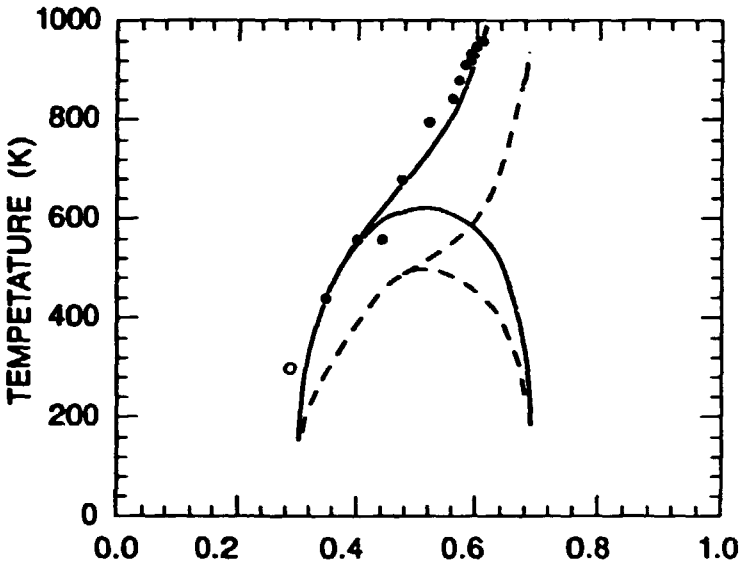


*Figure 18. The structural phase diagram of $YBa_2Cu_3O_{6+x}$. Comparison between our experimental data and equilibrium Monte Carlo simulations based on the ASYNNNI model. Two sets of interaction parameters are used. The fully drawn line corresponds to a best fit due to Hilton et al. [69], while the dashed line corresponds to first principles parameters, based on the LMTO calculations by Sterne and Wille [32].*

principles work, preferably reaching beyond the rather crude Connolly-Williams method [31] employed by Sterne and Wille.

The accuracy (5 %) and concentration range over which the phase transition temperature, $T_\phi$, is determined experimentally, cf. Fig. 9 makes it sensible to try as an alternative to fit the interaction parameters. Monte Carlo simulations or transfer matrix methods are the natural tools for such calculations, because the accuracy needed is beyond what can be obtained by CVM. However, making such multi-dimensional fits using standard MC or TM methods are at best a very tedious endeavour. Nevertheless Hilton et al. [69] have made an attempt. Their resulting best fit to our experimental data points is: $V_1 = -4176$ K, $V_2 = 2512$ K and $V_3 = -360$ K. Note especially the small $V_3$ parameter. The corresponding line $T_\phi = T_\phi(x,T)$ is shown for comparison in the same figure as the phase diagram made using the Sterne and Wille interaction parameters. The correspondance between fit and experimental data is obviously excellent. However, the inherent problems of such multi-dimensional fits should be remembered. Also, successful fits to the line of transition points do not guarantee that the interaction parameters are constants independent of concentration and temperature.

Recently, we have discovered that it is possible to circumvent the technical Monte Carlo problem by applying an extension of the Ferrenberg-Swendsen method [29]. This will in the present case allow for a reduction in computer-time of several orders of magnitude, and therefore facilitate realistic error bars to be assigned to the fitted parameters. A description of the method and its implication for the present case is given in chapter 2. Results are due shortly. Because the fitting problem is not completely solved, the original Sterne and Wille parameters are used as the standard set of interaction potentials in most of the studies below.

### 3.4.2 The Equilibrium Oxygen Partial Pressure

The equilibrium oxygen partial pressure P is related to the chemical potential in the sample by Eq. 36 and Eq. 38. The dissociation energy is concentration independent. It follows that the three abrupt changes in P with oxygen content appearing in Fig. 14 should be ascribed to either variations in the single site potential $V_0$, in the phonon spectra or in the two dimensional oxygen ordering process (the term $\mu_{2D}$). In the following, we will investigate whether the source of each of these abrupt changes could be the oxygen ordering process as described by the ASYNNNI model.

The equilibrium variation of $\mu_{2D}$ with $x$ is shown in Fig. 19 for four different reduced temperatures: $T = 0, 0.1, 0.125$ and $0.175$, using the Sterne and Wille set of interaction parameters. At $T = 0$ the curve exhibits three jumps at $x = 0, 1/2$ and 1. Between the jumps $\mu_{2D}$ is constant, an important observation, related to the absence of phase-separation even at the lowest temperatures. At higher temperatures the jumps broadens, and for $k_BT \approx \mid V_3 \mid$ the jump in the middle disappears. The existence of a jump at $x = 0.48(2)$ at low temperatures in the isotherms of the experimental oxygen partial pressure, cf. Fig. 14, is a direct proof of the thermodynamic stability of the Ortho-II structure. Independent of volume-fraction of Ortho-II present, we can deduce the temperature of the multiple point, where the tetragonal, Ortho-I and Ortho-II phases meet, from the temperature, where the jump disappears: $T_{\text{multi}} = 725(125)$ K. This is in excellent agreement with the independent value obtained from fitting the phase diagram, $T_{\text{multi}} = 630$ K, cf. Fig. 18.

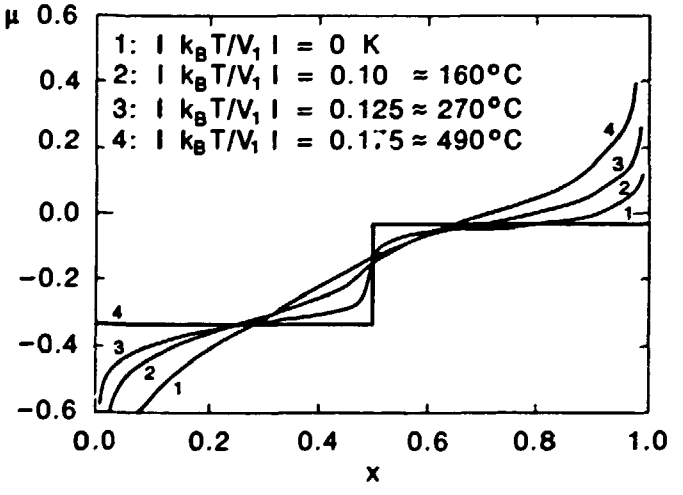


*Figure 19. Monte Carlo simulations of the variation of the chemical potential $\mu_{2D}$ with oxygen stoichiometry, $x$, for four fixed temperatures. The ASYNNNI model with the Sterne and Wille set of interaction potentials is used. Temperatures are given both in reduced units of $-\frac{k_B}{V_1}$ and on an estimated absolute scale in °C.*

The anomaly around the stoichiometry $x = 0.22$ can possibly be related to the existence of a disorder line in the tetragonal phase. A disorder line is generally defined as a line in a phase diagram marking positions where short-range correlations change their qualitative behavior [70]. Such disorder lines are often found in anisotropic lattice-gas models with competing interactions. The change in correlations are associated with increasing local fluctuations, analogous to a

conventional global phase transition. The increased amount of fluctuations again leads to maxima in the thermodynamic response functions, like - in the present case - the compressibility $(\frac{dx}{d\mu_{2D}})_T$ (x being the oxygen stoichiometry).

The existence of such an disorder line in YBCO around $x = 0.22$ was originally predicted by Rikvold and coworkers [71] using mean-field techniques as well as Monte Carlo simulations and Transfer Matrix results. However, they associated the change in local correlations with the breaking of local isotropy by formation of finite fragments of positionally and orientationally disordered oxygen chains. This is against intuition, because the formation of chains is energetically favourable at all temperatures in the ASYNNNI model and the disorder lines exist also at very low temperatures, where the entropy-terms are negligible. Also, the position of the disorder line is known to be sensitive to the $V_3$ parameter, and Rikvold et al. used a value for this parameter that differs from the best fit. We therefore repeat parts of their survey using the Sterne and Wille set of parameters instead, and are able to confirm their results. Our disorder line is found to be positioned at $x = 0.24(3)$ independently of temperature up to at least 1000°C, in striking agreement with the experimental data. However, the local symmetry-breaking is due to local orientational ordering of the already existing chain-fragments on increasing concentration. The high-concentration state is thus nothing but a finite-size variant of the Anti-Ortho-I domain mentioned in the introduction.

Experimentally, a similar extrema in the derivative of the equilibrium oxygen pressure is observed around $x = 0.3$ by McKinnon et al. [72] in a single temperature study at 650°C. A symmetrically positioned disorder line, also predicted from theory and positioned inside the orthorhombic phase near $x = 0.78$, does not appear in neither our experimental data, nor the work of McKinnon et al.

The most prominent feature of the experimental data, the steep rise in the compressibility at $x = 0.92$, cannot be explained on basis of the equilibrium ASYNNNI model. In stead it may be attributed to an abrupt change in $V_0$, due to a ferroelastic instability [73] or the phenomena of "over-doping" [74]. Alternatively the kinetics might be very sluggish [75], or the rise could be associated with the existence of depleted oxygen regions in connection with the twin-domain walls. In the later case the experimental data on the dimension of the twin-domains ($\approx 250$ Å) requires the depleted layer to have a thickness of 10 Å. In the following we will have oppurtinity to test several of these hypothesis theoretically.

Next, we will compare the theoretically derived values for the 2-D chemical potential of the oxygens in the superconductor, $\mu_{2D}$, with the experimental 3-D values of $\mu(O_2)$. The relationship between the two variables is given by Eq. 38: $\mu(O_2) = 2(\mu_{2D} + V_0 + \frac{\partial E_{ph}}{\partial N}) - E_d$. In order to avoid the large - and uninteresting - thermal depencies of the ideal gas in the gas bulb, the focus is on isothermal properties. Because the theoretical values vary more or less linearly with the interaction parameters, a full account of the resulting values of $V_0 + \frac{\partial E_{ph}}{\partial N}$ is only relevant once these parameters have been determined with a good accuracy. Here, we will be satisfied with as an example to give the result for the temperature $T = 490$°C, using the Sterne and Wille set of parameters.

The difference between the experimental and the theoretical chemical potential is shown as function of $x$ in Fig. 20. To expel the concentration independent terms the two potentials are set equal at $x = 0.35$. The structural phase transition is known to take place at $x = 0.54(2)$, cf. Fig. 9. Evidently, an onset appears exactly at the phase transition, with the difference in $\mu$ from vanishing beginning to grow rapidly towards the high $x$-value limit. It is found that a fit to $A + B(x - 0.54)^2$ gives reasonable results - in eV

$$V_0 + \frac{\partial E_{ph}}{\partial N} = 0 \quad \text{teragonal phase; } x < 0.54 \tag{45}$$

$$V_0 + \frac{\partial E_{ph}}{\partial N} = 0.008 + 2.02 \cdot (x - 0.54)^2 \quad \text{orthorhombic: } x > 0.54 \qquad (46)$$

The best fit is marked with a continuous line in Fig. 20.

This result for the single site potential (including the phononic contribution) may be directly compared to the observations of Shaked and coworkers [76]. They have derived the isothermal variation of the single site potential at the same temperature (490 °C) from neutron diffraction data of the site occupancies of oxygen O(1) and O(5) sites, and the quantum chemical approximation[9]. They find similar behaviour and a best fit of $V_0 + \frac{\partial E_{ph}}{\partial N} = 1.46 \cdot (x - 0.5)$ eV. We have "fitted" our data to the same function, and obtain a very reasonable fit. Hence, following two completely independent procedures we end up with indistinguishable results. We conclude that the single site potential and phononic contributions vary little with $x$ in the tetragonal phase, but rises steeply in the orthorhombic phase towards the maximum oxygen concentration. From Fig. 10 it follows that the lattice parameters - and hence probably the internal strain - develops linearly with $x$ at this temperature. Combining this piece of information with the successful fit to the quadratic form, we speculate that the rise is caused by the elastic forces in the material. From similar low temperature calculations we find that the rise in $V_0 + \frac{\partial E_{ph}}{\partial N}$ becomes very prominent towards $x = 0.92$. Thus we further speculate that the observed maximum in $x$ of $x = 0.92$ is related to the concentration dependency of the elastic forces.

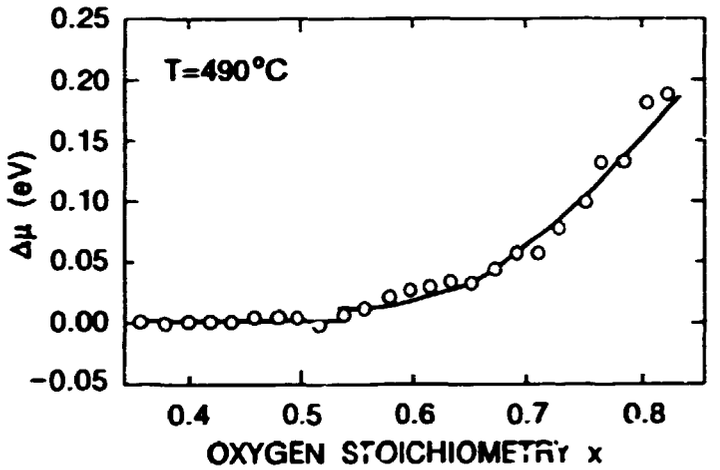


*Figure 20. The difference (o) in chemical potential $\Delta\mu = \mu_{exp}/2 - \mu_{2D}$ between the experimentally measured value and the theoretical value, calculated from Monte Carlo simulations of the ASYNNNI model. The figure refers to the variation with oxygen stoichiometry at a constant temperature of 490°C. The structural phase transition takes place at $x = 0.54$, cf. Fig. 9. The fully drawn line represents the best fit to $\Delta\mu = a + b(x - 0.54)$ for $x > 0.54$, with resulting $a = 0.008(3)eV$ and $b = 2.0(1)eV$. The quadratic rise is taken as an indication of the internal strain in the material growing linearly with $x$ within the orthorhombic phase (see text).*

[9]The site occupancies on the two oxygen sites in the basal plane cannot be resolved with the setup used in our experiment.

### 3.4.3 The Influence of the Twin Domain Formation on the Low Temperature Oxygen Ordering Processes

On slow cooling the tetragonal/orthorhombic phase transition is initially driven by the forces related to the configurational energy of the oxygen pair interactions, but in the final stages the elastic forces become very important, as manifested in the creation of twin domain boundaries. From the analysis of the broadening of the Bragg peaks, we infer that the sizes of the twin-domains become fixed shortly below the transition temperature. In a superficial sense we may therefore think of the resulting size of the twin domains as determined by the length scale where the "configurational forces" - trying to create larger randomly distributed domains - are matched by the internal stress. The "frozen" strain energy will then per definition exceed the energy involved in any oxygen ordering processes driven by the pair interactions and taking place at lower temperatures (well within the orthorhombic phases). Such processes will therefore only take place if they comply with the restrictions set by the internal stress. This observation has important consequences for the possible phase transformations from the Ortho-I phase to any of the low temperature phases belonging to the homologous series of chain-structures proposed by TEM measurements (cf. the experimental review in chapter 2). More generally, we may raise the question: is it reasonable to employ Hamiltonians that are defined solely in terms of oxygen pair interactions, e.g. the ASYNNNI Hamiltonian, for descriptions of the structural properties within the orthorhombic phases?

From the theoretical point of view the internal stress may be described in terms of elastic degrees of freedom. To include these in a projected Hamiltonian for the ordering processes in the basal plane, consider a 2-D pair-interaction Hamiltonian, $H_{bin}$ (e.g. the ASYNNNI model), and *copper* lattice sites situated at $\bar{r}_i$. The strain-free distance between two nearest neighbour (NN) copper sites, that bridge an oxygen ion is denoted $b$. Likewise, the strain-free distance between two NN sites, bridging a vacant oxygen site is $a$[10]. A revised Hamiltonian, $H_{tot}$, may then be defined by

$$H_{tot} = H_{bin} + H_{strain} \tag{47}$$

$$H_{strain} = \frac{V_{strain}}{2} \sum_{ij}^{NN} \sigma_{ij} (|\bar{r}_i - \bar{r}_j| - b)^2 \tag{48}$$

$$+ \frac{V_{strain}}{2} \sum_{ij}^{NN} (1 - \sigma_{ij}) (|\bar{r}_i - \bar{r}_j| - a)^2 \tag{49}$$

$$+ K \sum_{ij}^{NN} (|\bar{r}_i - \bar{r}_j| - d)^2 \tag{50}$$

where $\sigma_{ij}$ is the state of the oxygen site, situated between copper site $i$ and $j$. $\sigma_{ij}$ is 1 if the site is occupied and 0 if it is empty. The two former sums provide the coupling to the binary oxygen ordering process. The latter is an *ad hoc* penalty function introduced to keep the lattice from too excessive local distortions. (Without the latter term the lattice might self-intercept etc.). Other penalty functions with more direct physical intrepretations can be introduced, depending on the boundary conditions.

[10] Comparing with Fig. 20, the internal strain grows linearly with $x$ from $x \approx 0$, where it is vanishing. Hence, the stoichiometric Ortho-II case seems to be nearly strain-free, while the stoichiometric Ortho-I case is attributed with the maximum amount of stress. Thus $a$ and $b$ in Eq. 50 must be properly renormalized.

The literature provides little guidance for how to treat the extended Hamiltonian, Eq. 50. Physically the relaxation of the lattice following an oxygen jump will move with the speed of sound. Thus the internal strain is at all times in equilibrium given the specific oxygen configuration. Therefore, to proceed, let us first solve the Hamiltonian for a given oxygen configuration. Because the phonons have been left out, we simply have to find the ground-state of the lattice, $\bar{r}_i$. In order to get a linear description we approximate Eq. 50 by a version where the x- and y-parameters are decoupled. Minimizing this decoupled version of $H_{strain}$ with respect to $x_i$ and $y_i$ we end up with a linear set of equations, that even in some cases (depending on the boundary conditions) involve a band-matrix. The matrix inversion problem is sufficiently simple that it can be done within a reasonable time-frame.

Next, in relation to Monte Carlo simulations of the oxygen ordering the jump-frequency will to a first approximation be determined by the binary oxygen interactions and the **local** strain. Thus we may substitute $\exp((\Delta E_{bin} + \Delta E_{strain})/k_B T)$ for $\exp(\Delta E_{bin}/k_B T)$ in the Metropolis transition matrix, cf. Eq.17, where $\Delta E_{strain}$ is found by matrix inversion within some (small) square box around the site in question. The values of $x_i$ and $y_i$ at the boundary of the box are fixed. With suitable intervals more global minimizations of the strain energy must be done. Simulations performed along these lines are presently under investigation.

In this context, we will focus on some qualitative comments and predictions for the three dimensional case. We start by noting that the registry along the c-axis is determined solely by the internal stress. In fact, for e.g. the stoichiometric Ortho-II case, the (screened) Coulomb repulsion between oxygens leads to a 3-D ground state with a cell doubling taking place along the c-axis. In this ground state the chains in all basal planes are aligned, but they are translated a distance $a$ with respect to each other between two neighboring planes. However, simple calculations reveal, that due to the long distance between planes all binary interactions are negligible - at least for screening lengths below $\lambda \lessapprox 6a$.

Next, we note all members of the 2-D homologous series of chain-structures introduced in the review of the theoretical structural phase diagram, chapter 2, including the Ortho-II phase have a degree of degeneracy of at least four. The degenerate ground states belonging to one specific of these structural phases can be mapped into one another by translation and transposing (turning the lattice 90°). Now, imagine a stack of basal planes positioned on top of one another, all in 2-D ground state configurations, but not necessarily the same one. It is intuitively clear that mismatch between NN planes that involves transposing costs orders of magnitude more in excess strain energy than mismatch due to translation only. Effectively this means that once the twin domains are "frozen" only half of the 2-D degenerate ground states are available during the transformation to any low temperature phase. Within the ASYNNNI model (in fact any model with an attractive $V_2$ parameter) the low temperature thermodynamics is characterized as quasi-one dimensional within the planes. Combining these two observations the dynamics in creating any of the low temperature phases will be governed by translation of (long) chain fragments, all chains in all planes pointing in the same direction. However, the shuffling of chains in different planes need not be correlated. The Ortho-I phase itself constitutes an exception: here the degree of degeneracy was only two from the beginning, leaving no translational degrees of freedom after "freezing". Hence, when quenching into the Ortho-I phase, the 3-D registry will be assured much earlier than when quenching into e.g. the Ortho-II phase at the same temperature.

For the Ortho-II phase the difference between the T-OII phase transition for $x < 0.5$ and the OI-OII phase transition for $x > 0.5$ should be noticed, cf. Fig. 18.

In the former case twin domains are created, and the dynamics can be described in terms of the nucleation and growth of domains of the four types of Ortho-II ground states. In the latter case the twin domains were already formed in connection with the T/OI phase transition, and the dynamics is governed by the shuffling of chain-fragments. This has several consequences. First, we expect the size of the twin domains for $x < 0.5$ to reflect some intrinsic Ortho-II ordering vs. strain feature, while the size for $x > 0.5$ reflects the similar Ortho-I feature. Within the ASYNNNI model the boundary of the Ortho-II phase is known to be nearly symmetrical around $x = 0.5$. Still, based on the arguments above we would predict the room temperature twin domain size to change drastically at $x = 0.5$ (and only at this concentration), when cooling various samples at near constant stoichiometry. This is in perfect agreement with the experimental data, that leads to a distinction between two $x$-intervals, $0.30 < x < 0.50$ and $0.50 < x < 0.92$, with approximately constant twin domain sizes in each of 350 Å and 250 Å, respectively.

If the twin domain boundaries constitute effective channels for in-diffusion we would also expect a drastic change in diffusivity around $x = 0.5$. Again, this is consistent with our experimental in-diffusion data, where the 100 minutes isochrone is nearly vertical in (x,T)-space at $x = 0.5$ (cf. Fig. 16). To perform a quantitative analysis, we note that according to Eq. 41, $\tau \propto L^2/D_m$, where $\tau$ is the relaxation time, $L$ is the relevant length-scale and $D_m$ the effective mutual diffusivity. Assuming $D_m$ to be constant, $\tau$ should scale with the size of the twin domain squared when passing $x = 0.5$. Experimentally we find $\tau(x = 0.45)/\tau(x = 0.50) \approx 2.5$ below 30 °C, and for the corresponding ratio of the twin domain sizes $(L(x = 0.49)/L(x = 0.53))^2 = 2.0$. Thus, within the poor accuracy of our low temperature pressure relaxation measurements, the experimental data supports the idea of constant $D_m$ and the twin domain boundaries as effective diffusion path-ways.

Finally, concerning the Ortho-II phase, we note that the speed of ordering processes in general terms decrease sharply with the number of degenerate ground states. Hence, if we for a moment neglect the existence of an upper limit on domains in terms of the twin-domain size, we would expect the Ortho-II domains created when cooling down through the Ortho-I phase to have a larger coherence volumes than similar domains, created when cooling down through the T-OII phase transition. (In particular we would expect the coherence along the $c$-axis to be longer in the former case.) This is consistent with the experimental work by Beyers et al. [18], who reports on a much larger intensity in the Ortho-II superlattice spots appearing in TEM diffraction patterns for $x > 0.5$ than below.

Similar type of arguments can be applied for the additional members of the homologous series of chain-structures. 3-D registry will only appear when the in-plane domain sizes reaches a certain threshold limit. Due to the very sluggish kinetics at the low temperatures in question, it is very likely that this limit will never be reached. Furthermore, the question remains whether the phases will exhibit 3-D registry, even when in equilibrium. Here, it should be remembered that for a finite size system with a large degree of anisotropy the ordering temperature $T_\phi = T_{2D}$ for the in-plane ordering does not correspond to the 3-D critical temperature, $T_{3D}$. (In the thermodynamic limit, $L \rightarrow \infty$, we must have $T_{2D} = T_{3D}$). The finite length scale in the present case is the "frozen" size of the twin-domains. Hence, it is probably a good approximation to treat the low temperature structural phase diagram in terms of randomly positioned interstitial chains in an Ortho-I or Ortho-II matrix. Such an approach has reasonably successfully been attempted by Khachaturyan et al. [77].

### 3.4.4 Diffusion

Several fundamental questions rise in connection with the diffusion process in YBCO: Is the kinetics determined by the bulk behaviour?, Does metastable states appear?, How non-linear is the process? and what constitutes the effective length-scale for in-diffusion? Answering such questions is a prerequisite for establishing connections between experiment and theory for the microscopic kinetics. Also, it should be remembered that the success of dynamical MC simulations may depend crucially on the assignment of the physically correct jumping range (e.g.: do the oxygens only jump between nearest neighbour (NN) sites or do additional next nearest neighbor (NNN) particle/vacancy exchanges take place?) In the following we will try to sort out some of these gross scale features.

First, we note that the succesful fitting of the experimental in-diffusion data to Ficks law - a simple exponential, when the higher harmonics have died out - provides evidence that the kinetics is determined by bulk behaviour. This is consistent with the general trend in the literature. (The mechanism governing out-diffusion has on the other hand to the author's knowledge not been revealed.) We have also speculated that the twin domain boundaries might be effective channels for diffusion. Next, we will focus on the concept of metastability. Here, we will introduce some additional experimental work, we performed early on [78]. The work is related to the far from equilibrium physical properties of large-scale in-diffusion. An YBCO-sample is initially reduced by evacuation at 750 °C for two hours, *in situ* on a neutron powder diffractometer. The sample is then cooled to room temperature and the chemical potential abruptly changed by exposing the sample to one atmosphere of oxygen pressure. The following relaxation towards the equilibrium $x \approx 0.92$ orthorhombic state is monitored by the time evolution of the intensity of the tetragonal $(2,0,0)_t$ and the orthorhombic $(2,0,0)_0$ and $(0,2,0)_0$ peaks. The temperature is initially kept constant at 110 °C for 16 hours, then increased to 165 °C for an additional 60 hours, followed by a final heating for 3 hours at 252 °C. The resulting time-dependence of the peaks and the temperature profile is shown in Fig. 21. The general feature appearing in the figure, is that following a **small** rise in temperature initially a large increase in the intensity of the orthorhombic peaks takes place, then the process seemingly dies out at a **finite** ratio, with a substantial amount of tetragonal intensity left. This is not as expected from continuum models, like the one used to analyze the quasi-stationary in-diffusion data in the experimental part of this chapter.

However, more pronounced experimental evidence for the concept of metastability is at hand. At room temperature, it is generally acknowledged that the stoichiometry in samples does not change over months, independently of the partial pressure in the surroundings [4]. Such behaviour cannot be explained as a temperature effect, extrapolating activated diffusivity coefficients found at higher temperatures to 300 K. Hence it must be due to the introduction of some hypothetical surface barriers at low temperatures or due to metastability/freezing of the bulk kinetics.

Trying to understand the concept of metastability/freezing within the ASYNNNI model, Monte Carlo simulations of the large scale in-diffusion process are performed. Such studies are also important to get a qualitative understanding of the structural inhomogenieties in far from equilibrium samples. Here one may compare with the case of quenched samples. For the latter case, an extended theoretical survey, including comments on the implications for annealing schedules has been provided by J.V. Andersen et al. [79].

Technically, we pursue fixed temperature simulations, where an initially empty configuration is disposed to a fixed chemical potential at the surfaces, sufficiently large to allow for full oxidation ($x \approx 1.0$) to be the equilibrium state. The sim-

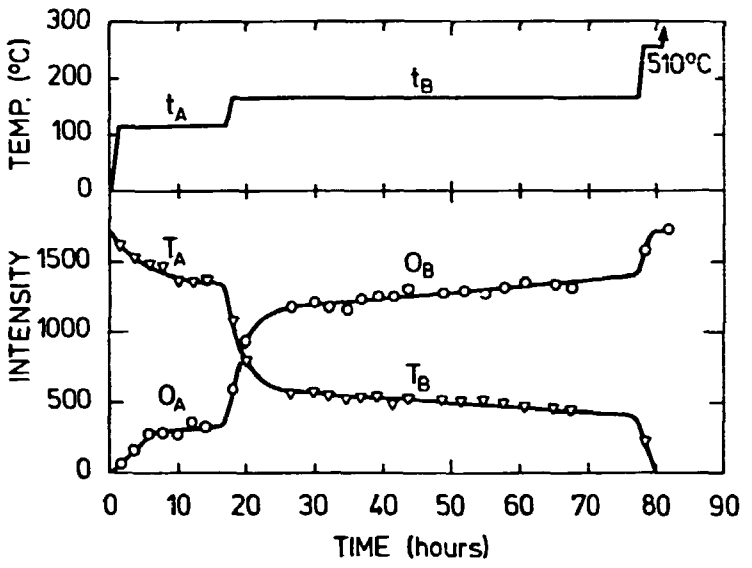


*Figure 21. Time dependence of neutron diffraction peak intensities during the transformation from tetragonal to orthorhombic phase (start: $x \approx 0$) obtained from: the tetragonal $(200)_t$ peak, and the sum of the orthorhombic $(020)_o$ and $(200)_o$ peaks. Upper part shows the temperature profile for the experiment. The two constant temperature plateaus named A and B corresponds to $t_A = 110°C$ and $t_B = 165°C$, respectively. From the experiment by Als-Nielsen et al. [78]. The time dependence is taken as indication for NN oxygen jumps only, see text.*

ulation algorithm is based on Kawasaki dynamics in the interior and Glauber dynamics on the borders of a square 64 x 64 lattice. The attempt frequency for sites governed by Glauber dynamics has been set equal to the attempt frequency for the Kawasaki sites, implying that the diffusion is governed by the bulk properties. During the in-diffusion process an analysis of the average oxygen concentration and the amount of Ortho-I and Ortho-II domains present is continuously performed.

Using the Sterne and Wille set of interaction parameters simulations are performed at reduced temperatures $| k_BT/V_1 | = 0.15, 0.13, 0.10$ and 0.07, the latter corresponding to room temperature. Two types of oxygen jumping is considered: an isotropic NN case, and an isotropic case with equal jump-frequency for jumps to NN and NNN sites. An example of the instantaneous configuration, taken when the average concentration becomes $x = 0.5$ for the NNN case and $T = 0.10$ is shown as a snapshot in Fig. 22. From the figure, it is clear that the kinetics can be described in terms of a shell model. Initially an outer shell consisting of a nearly perfectly ordered Ortho-I structure is formed very fast. From the inner interface of this shell another shell of nearly perfect Ortho-II structure is nucleated. The center region may be described in terms of single or paired chains stretching into a tetragonal void. The interfaces between the two orthorhombic shells and between the Ortho-II phase and the tetragonal phase are growing with approximately the same speed, and the area of the Ortho-II shell reaches a maximum of 20% of the total area at $x \approx 0.7$. The model develops a global orientationally preference shortly after the beginning, and will generally evolve into a single domain. The evolution of the average oxygen concentration with time is shown in Fig. 23. The shell-formation does not appear to give rise to major non-linearities[11]. Another

[11] Diffusion models with temporal evolution of interfaces between different domains with different diffusion constants cannot be solved analytically

important observation is that the average oxygen content steadily rises until the equilibrium value of $x = 1.0$ is reached. Thus, the experimentally observed upper limit of $x = 0.92$ cannot be attributed to a freezing of oxygen vacancies in the case of NNN hopping. The NNN-features reported above are general for the four temperatures used in the simulation, with the one exception of the disappearance of the Ortho-II shell above the temperature for the multiple point.

The evolution of the average oxygen concentration with time for the case of nearest neighbors only is shown together with the previously mentioned NNN case in Fig. 23, for T=0.10. The time scale for the two figures are different in order to exhibit the main features of both cases in the same figure. Clearly, in the NN case, metastability occurs. For iterations beyond 50,000 MCS/site the oxygen content is fixed. Comparing snapshots of the instantaneous oxygen configuration taken at different times in the interval after this fixation reveals that the configuration is truly "frozen": the snapshots are (nearly) identical. The appearance of meta-stable states are found for all temperatures, the oxygen concentration of the metastable state decreasing with lower temperatures.

To understand the phenomenon, we note that in the NN scheme the oxygens have to jump successively between the O(1) and the O(5) sub-lattice. For $k_BT << V_2$ the equilibrium ASYNNNI model behaves quasi-onedimensional, cf. the theoretical review in chapter 2. Thus at low temperatures the O(5) lattice is (nearly) depleted and (nearly) all oxygens are situated in chains. Breaking such a chain in the middle will be associated with an energy barrier of at least $V_1$, and is therefore a very rare event. Hence, the only "allowed" jumps in equilibrium are those associated with adding and subtracting particles from the end of the chains. This is in contrast to the NNN case where braking a chain may cost as little as $V_3 \approx 350$ K in energy.

For the NN metastable state, we find from the snapshots that a perfect Ortho-I shell has developed near the surface, preventing further in-diffusion from the environment. In the center perfect Ortho-II domains evolve. Locking appears between these domains, and the domains and the boundary-shell, meaning that the relevant particles in the chain ends have no favorable sites to jump into. This locking phenomena obviously is the root of the appearance of metastable states in the simulations. The exact average oxygen concentration at which the locking takes place is to a first approximation given by the ratio between a temperature dependent shell thickness and the total size of the lattice. Without information of the lattice size in the neutron diffraction work mentioned above it is not possible to attempt a direct comparison between theory and experiment. However, the qualitative feature of jumps between different metastable states on small variations in temperature is also found in simulations. Finally, for the experimentally observed "freezing" around room temperature, we note the coincidence between this temperature and the temperature where the equilibrium site occupancy of the O(5) sites goes to 0, according to the CVM calculations by Ceder et al. [33]. It is tempting to relate the two facts, providing an explanation for the freezing. However, refinements of room temperature neutron diffraction data of the site occupancies [5], [7], [3] generally tend to leave a small fraction of approximately 4 % of the O(5) sites occupied.

We conclude, that the oxygen kinetics is governed (predominantly) by NN jumps, leading to metastable behaviour for large scale indiffusion at low and intermediate temperatures. This observation has important consequences for annealing procedures and comparison between different set of experimental data in general. A complete understanding of the details of the room temperature freezing effect is still lacking.

From the analysis above, we argue that a reasonable degree of understanding of the fundamental properties of the in-diffusion process has been achieved. Hence,

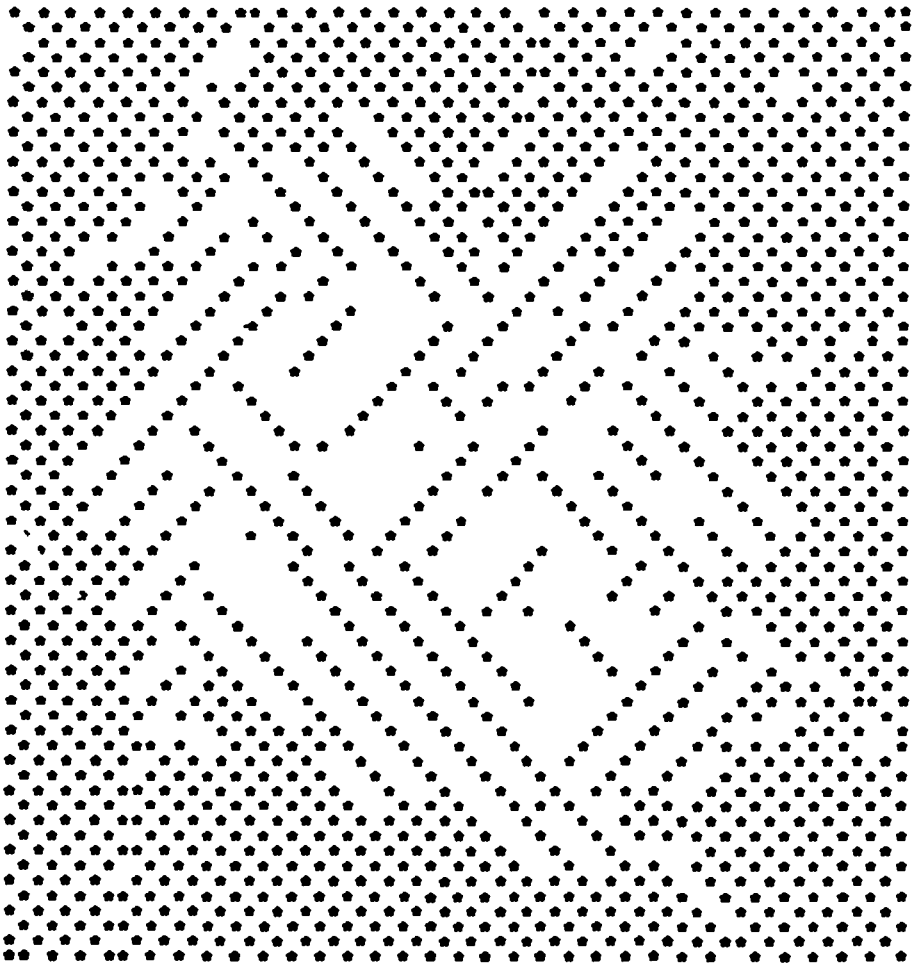

*Figure 22. Snapshot of the instantaneous oxygen configuration in the basal plane during in-diffusion from the boundaries of the lattice. Only oxygen sites are shown: (°) denotes filled, (·) empty sites. The lattice was originally empty, then exposed to a constant external chemical potential of $\mu = 1$, that eventually will lead to an equilibrium state of the perfect Ortho-I structure. The Sterne and Wille parameters are used, and the constant temperature is $|k_BT/V_1| = 0.10$. In the bulk equal attempt-frequencies are described to all nearest neighbour and next nearest neighbour jumps.*

we may proceed to deduct micro kinetic properties, like the diffusivity coefficients, activation energies etc. from the simulations. Such theoretical investigations are still at an intermediate stage. In this context, we therefore desist from a discussion of these properties.

## 3.5 Discussion

During the theoretical part of this chapter we have been focusing on the simple ASYNNNI model. Discussing the experimental data in relation to e.g. models with interaction parameters depending on the oxygen stoichiometry is more difficult. Generally details of the electronic properties for the basal plane have to be taken

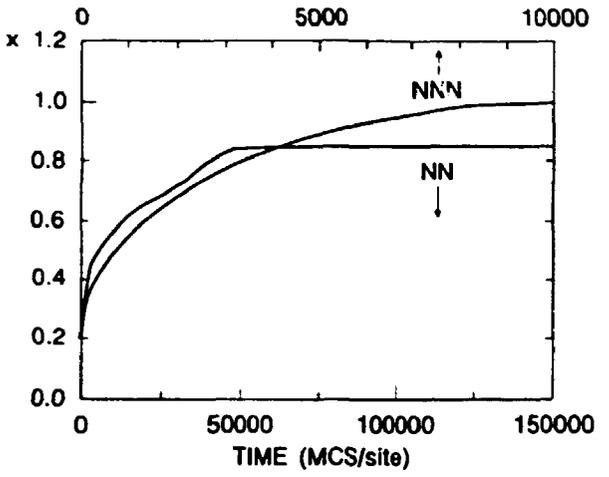


*Figure 23. The simulated dynamics of the in-diffusion process described in terms of the relation between average oxygen stoichiometry: $6 + x$ and time measured in units of MCS/site. The initially empty lattice is exposed to a high chemical potential at the surface, eventually leading to the stoichiometric Ortho-I phase. The temperature is kept constant. Two curves relating to the case of nearest neighbour (NN) oxygen jumps only, and nearest neighbour as well as next nearest neighbour (NNN) jumps are shown. The Sterne and Wille set of interaction parameters are used, the corresponding reduced temperature being $| k_B T/V_1 | = 0.10$. To be able to display both curves in the same figure different time scales are used.*

explicitly into consideration. Reliable experimental data are often lacking. However, the size of the $V_3$ parameter determined from the equilibrium partial pressure constitutes a fixpoint, because it refers to a constant stoichiometry, $x = 0.5$. Thus in relation to the Aligia model, Eq. 4, we can determine the screening length $\lambda(x = 0.5)$. Assuming the effective charge on the oxygens in the basal plane to be $q = -2 \mid e \mid$, we find $a/\lambda(x = 0.5) = 8.0$, where $a$ is the lattice constant. Assuming $q = - \mid e \mid$ in stead, we obtain $a/\lambda(x = 0.5) = 6.7$. Thus for all reasonable choices of $q$, the screening length is very small. According to conventional wisdom the screening length ought to decrease with increasing oxygen content. Hence, for $x > 0.5$, $\lambda$ will generally be smaller than $0.15a$. Inserting in Eq. 5 all the longer range potentials - beyond $V_3$ - becomes totally negligible (e.g. the size of the $V_4$ parameter is at most 1 K). Clearly experimental input is needed in order to determine whether such small screening lenghts are meaningful. If they are, the observed homologous series of chain-structures can definitely not be stabilized by the oxygen pair-interactions, and must therefore be of a transient nature. If they are not, the Aligia model has inconsistencies.

There is a large scattering between the structural data reported in the literature. It is our viewpoint that most of these discrepancies are due to different methods of estimating the absolute oxygen stoichiometry and different annealing schemes. Furthermore, variations in powder densities and grain size distributions will effect the formation of twin domains and the diffusion constants. In the following we will compare our results to some reference experiments, and try to relate the possible differences to these three main factors.

First let us compare the room temperature value of $T_\phi$, $x_\phi(300)$ [5], [7], [80]. Here, Jorgensen et al. [5] reports on $0.35 < x_\phi(300) < 0.38$, on quenching to liquid nitrogen from 500°C. This agrees with the result of Cava et al. [7] who find $0.35 < x_\phi(300) < 0.45$ using a Zr-gettering technique and quenching from

440°C. Our data - referring to a slowly cooled sample - points toward a lower structural transition concentration $0.28 < x_\phi(300) < 0.34$. Seemingly, the onset of the structural phase transition drops toward lower $x$-values with increasing annealing time at low temperatures. This is consistent with the very slow in-diffusion relaxation rates measured in this part of phase space, cf. Fig. 16.

The variation of the lattice parameters as function of temperature and concentration in Fig. 10 is smooth. This is in contrast to the report by Cava et al. [7] of a jump in the c-axis parameter of $\Delta c = 0.08$ Å at 5 K between $x = 0.35$ and $x = 0.45$ on quenching from 440°C. Initially the sample had been annealed for four days at this temperature using a Zr-gettering technique. It has been suggested that the appearance of the jump should be attributed to the Zr-gettering technique, speculated to give rise to better equilibrated samples. However, the slow kinetics around $x = 0.30$ below 400 °C might again be the correct explanation.

For the oxygen partial pressures, a review is due to Lindener [81]. He concludes, that the results in the literature are strongly dependent on experimental technique and sample preparation method. We have compared our data, cf. Fig. 14, with those reported by Specht et al. [82] and Schleger et al. [83], the former cooling along the isobars, the latter performing isothermal measurements at temperatures above 450°C. Our interpolated isotherms exhibits the same variation with oxygen stoichiometry, but are shifted $\Delta x = 0.07$ downwards compared to the two other data set. This discrepancy is almost certainly due to different methods of determining the absolute x-values, the two other groups attributing their most oxidized samples to the ideal stoichiometry of $x = 1.0$.

The kinetics of the oxygen in-diffusion process in the YBCO ceramic is quite complicated, with diffusion taking place along the surface, the grain boundaries, micro-cracks and twin domain boundaries in addition to the true bulk kinetics. Furthermore, the present study provides strong theoretical arguments for the existence of metastable phenomena in the bulk behaviour. Moreover, there are theoretical indications that mutual diffusion and tracer diffusion coefficients may vary with a factor of 100 or more [68]. Consequently, the scattering in the experimental data is on the scale of orders of magnitudes. For a review see e.g. ref. [102]. Before the sources of the large scale differences have been identified it is probably risky to do calculations of microscopic diffusivity coefficients etc. Studies of the macroscopic diffusion properties might also provide valuable input for the most important of the remaining sample preparation issues: how to oxidize large single crystals.

## 3.6 Conclusion

In the metallic regime, our experimental data provide strong support for the validity of the 2-D ASYNNNI model description of the oxygen ordering process. Thus a jump in the chemical potential at $x = 0.48(2)$ is evidence of the thermodynamic stability of the Ortho-II phase, and the structural phase transition at room temperature takes place at $x \simeq 0.28(2)$, in agreement with theory. Interaction parameters $V_1 = -4176$K, $V_2 = 2512$ K, and $V_3 = -360$ K gives an excellent merit of fit to the location of the experimental structural phase transition line, and predict the correct position of the multiple point (T/OI/OII) at $x = 0.5$ and $T = 725(125)$ K. Multiple phases do not appear, in agreement with predictions of second order phase transitions and the existence of non-stoichiometric phases at all temperatures. With the difficulties of calculating *ab initio* parameters in mind, the reasonable correlation with the independent LMTO parameters by Sterne and Wille is most encouraging.

In the semiconducting regime kinks in the oxygen compressibility at $x = 0.22(2)$ are consistent with a disorder line in the ASYNNNI model due to local orienta-

tional ordering of already existing chain-fragments. Hence $V_2$ is most likely positive for all oxygen concentrations, at least at high temperatures. This is possibly in contradiction with the low temperature observation of a stable $4\sqrt{2} \times 2\sqrt{2} \times 1$ phase by Sontagg et al. [?].

From an analysis of the broadening of the Bragg peaks we find evidence that the size of the twin-domains during slow cooling freezes shortly after passing the phase transition. Hence the room temperature size is determined by which of the orthorhombic phases (OI or OII) the sample initially enters. The corresponding average values for the OI and OII phases are 250 Å and 350 Å, respectively. A discussion on the influence of the twin domain formation on the low temperature ordering process, including a novel theoretical approach for including the internal strain in Monte Carlo simulations are given.

The gas-volumetric technique has proven a powerful tool for deducing information on both the thermodynamics of the oxygen ordering, and the internal strain. Hence, assuming that the ASYNNNI model gives a valid description of the oxygen ordering, a quadratic rise with $x$ in stress energy - corresponding to a linear increase in the internal strain - is found in the orthorhombic regime. Associated with this steep increase in stress energy is the existence of an upper limit on the oxygen concentration: $x = 0.92(2)$.

The in-diffusion process is at high and intermediate temperatures governed by the bulk kinetics. We provide strong evidence - based on earlier experimental data - that nearest neighbour hopping is the relevant oxygen hopping range, leading to metastability phenomena in far from equilibrium experiments. Also, the $x = 0.92$ limit on the oxygen concentration might be related to freezing of chain-segments of vacancies. We further speculate that the twin-domain boundaries are effective pathways for the diffusion. Experimentally, we find Arrhenius behaviour of the pressure relaxation times at high temperatures for all $x$-values with activation energies of 0.55 eV and 0.25 eV in the tetragonal and orthorhombic phases, respectively. Below 450 °C a marked enhancement of the relaxation time appears in the interval $0.32 < x < 0.48$, relevant in connection with e.g. discussions of the plateau-behaviour of the superconducting transition temperature.

# 4 The Relationship between Structure and Superconductivity

The object of this second part [104], [105], [106] of the thesis is to theoretically investigate the possibilities for explaining the observed static and dynamic variations of the superconducting transition temperature - reported in the literature - within the framework of a linear charge transfer model.

The outline is as follows: first an introduction to the relevant experiments is given in connection with some general comments on the relationship between structure and superconductivity in $YBa_2Cu_3O_{6+x}$. The linear charge transfer model is presented. Next a systematic Monte Carlo simulation study of the equilibrium features of the ASYNNNI model allows us to set strong constraints on the nature of a linear charge transfer process. A specific model is established. In the following section a corresponding simulation study of the dynamic features of the ASYNNNI model is performed. Based on a reanalysis of the experimental data a rather fundamental relation between the time-evolution of the structural and superconducting properties is revealed. Finally in the discussion part we demonstrate how the static and dynamic information merge to give a coherent picture of the charge transfer process. A physical interpretation of this result is offered, and suggestions for extensions to other copper-oxide superconductors are added.

## 4.1 Introduction

Shortly after the discovery of $YBa_2Cu_3O_{6+x}$, it was realized by Cava and coworkers [107], that the variation of superconducting transition temperature, $T_c$, with oxygen content exhibits so-called plateau effects. From a later reference work by this group [7], the resulting variation is reproduced in Fig. 24. On lowering $x$, a plateau of $T_c \approx 93$ K for $x > 0.85$ is followed by a broad intermediate region, then another plateau of $T_c \approx 58$ K for $0.45 < x < 0.6$, before a final disappearance of superconductivity takes place near $x = 0.3$. The Meissner volume fraction in this study is above 50 % for all superconducting samples, while the widths of the superconducting transitions are much broader (up to 3 K) for samples belonging to the intermediate region, $0.6 < x < 0.85$, than for samples belonging to the plateau regions.

Many similar studies have been performed, most notably by the Argonne group headed by Dr. Jorgensen [9]. In general the generics of the lineshape of the curve in Fig. 24 (two plateaus and a distinct cutoff for $T_c$) is reproduced, but details tend to vary. The differences are believed to be due partly to different standards for determining the absolute $x$-values, partly to different annealing procedures. Especially the latter cause has proven to be crucial, with more pronounced plateaus for better equilibrated samples. The plateaus can in fact be made to disappear completely by quenching from sufficiently high temperatures [103]. At present it remains an open question what the $T_c$ versus $x$ curve looks like for the true equilibrium state.

A major breakthrough took place in 1990 by findings due to the Argonne group [4], [3], [84] of time-dependent variations of $T_c$ appearing in quenched YBCO as function of room temperature annealing. As a part of this work Jorgensen et al. [3] reports on the equilibration of a powder sample at 520 °C for 112 h. The oxygen content at this point is determined by iodiometric titration to be $x = 0.41$. The sample is then quenched into liquid nitrogen, and broken into two pieces. During the following week both pieces are annealed in air at room temperature, the first one *in situ* on a neutron diffractometer. With suitable intervals the second piece is cooled for a short time in order to measure the magnetization with a SQUID, and

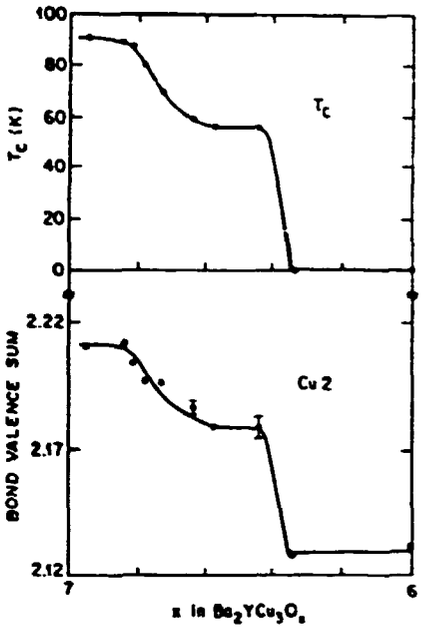


*Figure 24. Comparison of superconducting transition temperature $T_c$ and the bond valence sum of the bilayer Cu(2) copper as function of oxygen stoichiometry. Reproduced from Cava et al. [7]*

infer the value of $T_c$. The resulting transition temperature as function of annealing time is reproduced in Fig. 25.

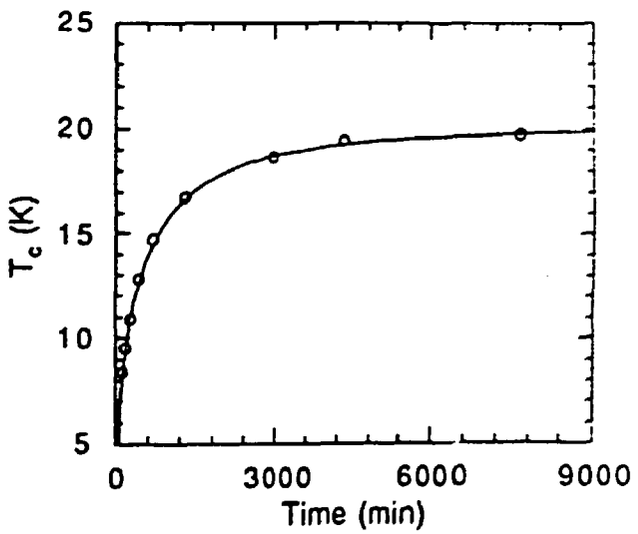


*Figure 25. Superconducting transition temperature, $T_c$, as function of the annealing time at room temperature for a quenched sample of $YBa_2Cu_3O_{6.41}$. The indicated $T_c$'s are the onset temperatures for diamagnetism. The solid line is the the function $T_c(t) = T_c(\infty) - (T_c(\infty) - T_c(0))\exp(-(t/\tau)^{0.5})$, with $\tau$ = 386 min. Reproduced from Jorgensen et al. [9]*

From Fig. 25 it is evident that $T_c$ begins to increase rapidly with time after 2 hours from a value of 0 K for later to level off at an asymptotic value near 20 K.

This behavior is shown by Veal [4] to take place independent of the oxygen pressure in the environment, reflecting the well-known fact that at room temperature the oxygen in-diffusion is extremely sluggish, effectively not altering the oxygen stoichiometry. The dynamical variation of $T_c$ is thus a direct proof, that the superconducting properties depend on the configuration of oxygens in the basal plane, not just on the average oxygen concentration. This dependency is the reason for the above mentioned variations in the static $T_c$ versus x data, due to differences in oxidation procedures. The experimental data shown in Fig. 25 was originally - on an empirical basis - fit to the function $T_c(t) = T_c(\infty) - (T_c(\infty) - T_c(0))\exp(-(t/\tau)^{0.5})$. The curve corresponding to the resulting best fit, with $\tau$ = 386 min. is also shown in the figure. Obviously the merit of fit is reasonable. However, from the number of experimental points it is clear, that the functional form cannot be determined in a unique way.

The corresponding neutron diffraction study reveals a drastic decrease with time in the a- and c-parameter of about 0.04%, while the b-parameter is almost constant. It is possible to fit the evolution of the orthorhombic strain to the same type of empirical curve as used for $T_c$ with the same value of $\tau$, suggesting a common origin to the temporal evolution. Another important finding from this work, is that the site occupancies on the O(1) and O(5) sites are constant during the experiment with values n(O1) = 0.36(1) and n(O5) = 0.04(1), respectively. Any oxygen ordering process taking place will therefore effectively be reduced to local reordering within the O(1) sublattice.

Next, the Argonne group investigated the concentration dependency of the dynamic effect. The resulting rise in $T_c$, $\Delta T_c = T_c(\infty) - T_c(0)$, following a fast quench to room temperature is plotted as function of $x$ in Fig. 26 (reproduced from ref. [84]). Evidently the dynamic effect reaches its peak value at low $x$-values associated with the 60 K plateau, while it is vanishing in the intermediate region and on the 90 K plateau. This behaviour is almost certainly related to differences in relaxation time constants. Notice in particular, that the large $\Delta T_c$ values are confined to $x < 0.5$. This coincides exactly with the region where our diffusion studies reported in chapter 3, resulted in very long relaxation times, cf. Fig. 16. The kinetics for $x < 0.5$ is also expected to be slower from a theoretical point of view, cf. section 3.4.3.

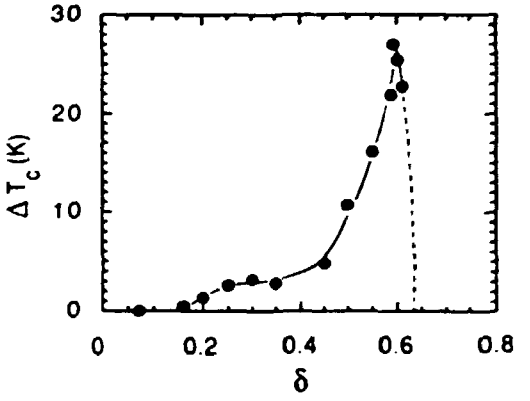


*Figure 26. Difference in $T_c$ for single crystals annealed at 25 °C and crystals annealed at 290 °C and quenched rapidly to room temperature, plotted as function of $\delta = 1 - x$. From Claus et al. [84]*

Much effort has been invested in trying to relate the features of the $T_c = T_c(x)$ curve directly to structural properties. Presently only one thing is nearly univer-

sally accepted: YBCO only becomes superconducting when orthorhombic. Actually, the onset of $T_c$ appears in all studies at $x$-values that are slightly higher than the $x$-values for the structural phase transition. This trend is also found in dynamical studies [4]. Studies of the superconducting properties of $YBa_2(Cu_{1-y}M_y)_3O_z$, where M is Co or Fe (doping on the Cu(1) site) were originally thought to contradict this picture: samples were both superconducting and tetragonal for some y-values. However, quite recently it has been proven [85] that the symmetry in effect is only tetragonal on the average. The microdomains are actually orthorhombic, but their coherence volumes are very small. It is even likely that a minimum amount of orthorhombic strain may be necessary for superconductivity in this material, as will be discussed later. It should be added, that the question of whether all copper-oxide superconductors have anisotropic $CuO_2$ layers when superconducting has not been experimentally settled.

The implications of the 90 K plateau have been much debated. As discussed in chapter 3 the inverse oxygen compressibility rises steeply with $x$ near $x = 0.92$, not permitting the stoichiometric compound to be synthesized with our annealing technique. We gave evidence that this phenomenon originate in a similar rise in the internal stress of the material. Hence, we may speculate that the 90 K plateau is associated with a ferroelastic instability, with the stable compound under high oxygen pressures being $YBa_2Cu_4O_8$. Alternatively, the 90 K plateau is an example of "overdoping", the existence of a maximum in the general $CuO_2$ hole concentration versus $T_c$ relationship (or the structural and electronic "instabilities" may be related). In the case of overdoping, one would expect the plateau to be a rounded maximum with the peak centered at $x = 0.92$, and expect a minimum at the same position for the pressure dependence, $dT_c/dP$. Both phenomena are found in a study by Rusiecki et al. [75], who claims that the fully oxidized state can be reached by a very prolonged annealing procedure.

Understanding the nature of the 60 K plateau seems more troublesome. It is clear - by comparing to other high $T_c$ materials - that it cannot be due to some general feature only related to the $CuO_2$ planes. Interpreting the plateau in terms of a structural phase, the Ortho-II phase is the only candidate. The (1/2,0,0) super-lattice peak identifying the phase, is observed in TEM studies on well equilibrated samples in the interval $0.28 < x < 0.65$ [18], [19], [20], an interval that spans the plateau region. Moreover, in the extensive study by Cava, previously mentioned, only one sample, at $x = 0.64$, showed a multiple transition, indicating the coexistence of two phases in the sample with $T_c$'s of approximately 53 K and 71 K. Intuitively such behaviour would be expected near the phase boundary, in agreement with the above mentioned experimental span for the Ortho-II phase.

Further, Beyers et al. [18] proposed to interpret the intermediate region as a superposition of minor plateaus related to additional phases in this interval. This point of view rises some problems related to the kinetics. Thus from Fig. 25 we learn that virtually no increase in $T_c$ takes place in this region during a dynamic measurement. Hence, either the kinetics is very fast, and the $T_c$ vs. $x$ curve should correspond to equilibrium behaviour, or the kinetics is very slow, and the transformation to the various low temperature phases have hardly started. In the former case, the additional plateaus should be present (and the corresponding structural phases be clearly visible in e.g. TEM measurements), while in the latter the minor plateaus remain a somewhat academic concept. Also, it should be remembered that there are both experimental (section 2.2) and theoretical reasons (section 3.5) to believe that the additional phases are of a transient nature.

More generally the idea of associating plateaus etc. with specific structural phases is likely to be a misconception. Thus, from the structural investigations in chapter 3 we concluded that the ASYNNNI model provides a valid description of the oxygen ordering process in the metallic regime. Within this model the

non-stoichiometric compounds are stable even at $T = 0$. More importantly, at intermediate temperatures, and say $x = 0.6$ the equilibrium configuration consists of a percolating cluster of the Ortho-II type with dynamic fluctuations of clusters with higher average oxygen concentrations, most notably Ortho-I type clusters, inside it. Hence, the relevant description of the oxygen configuration in the basal plane is in terms of a thermodynamic model comprising the dynamical coexistence of several structural phases, not in terms of a series of single-phase structures following one after another as function of $x$. It should be added that there are no signs in the literature of dips in the Meissner volume fraction near the phase transition lines between any of the (hypothetical) low temperature orthorhombic phases. (There is a sharp decrease in volume fraction associated with the cut-off for $T_c$ near $x = 0.3$, but that is another story.)

The conclusion to be drawn from the discussion above is that the superconducting transition temperature depends on the oxygen configuration in the basal plane; this configuration can in turn only be described in terms of a model of the thermodynamics of the oxygen ordering process. Based on our experimental findings in chapter 3, the simple ASYNNNI model is an excellent candidate for such a model.

Turning next to the electrostatics of YBCO, it is crucial to gain information on the number of holes in the $CuO_2$ planes and in the basal plane as function of oxygen stoichiometry. Unfortunately direct probes like electron energy-loss spectroscopy and angle-resolved photoemmision spectroscopy [87] cannot produce data with a sufficient accuracy. (However, they do conform to the picture of disappearance of holes in the $CuO_2$ planes for non-superconducting samples, and they are able to determine the symmetry of the holes: predominantly O 2p character.) Instead more indirect measures have been used. Among these arguably the most successful one is an empirical technique based on structural measurements, known as the "bond valence sum" method. We will give a short introduction.

The object of the "bond valence technique" is to relate the valence of a cation to the bond-lengths of the cation-anion bonds surrounding it, by referring to a data base of well characterized compounds. Thus by definition the bond valence sum of a specific cation, V - a measure of its formal valence- is given in terms of the distance to the nearest neighbors $R_i$, by

$$V = \sum_i \exp(R_0 - R_i)/B. \tag{51}$$

The constant B is universal $B = 0.37$, while $R_0$ characterizes the cation-anion pair and the formal valence of the cation (assumed integer). Brown and Altermatt [86] have prepared an extensive tabulation. It has been shown that for most compounds where the formal valence is known, V lies within 0.1 of the correct result. Interpolating between values of V for different integer formal valence (different $R_0$) has become a widespread method to measure the formal valence of mixed valence compounds. For covalent bindings like the Cu-O pair in the bilayers of YBCO, the bond valence sum of course cannot be taken as a measure of the Cu valence, but reflects the total charge in the bond instead. One problem with the method is that the bond-lengths are determined not only by the valences, but also by the internal stress in the material. However it is possible, although demanding, to determine both the strain-field and the valences in a self-consistent manner [73]. Three additional problems arise in the case of the YBCO Cu(2) site: the database of $Cu^{2+} - O^{2-}$ compounds is very limited, the possible split-site of the O(4) site may blur some of the bond-length determinations, and finally, it remains a question whether it is meaningful to talk about a Cu formal valence varying continuously between 2 and 3 in the first place. Additional critical remarks to the use of bond valence sums in copper-oxide superconductors studies have been given recently by Jansen et al. [88].

The most extensive experimental survey that relates to the use of the "bond valence sum" concept is due to Cava and coworkers [7]. They prepared a series of oxygen deficient pellets by a Zr-gettering procedure, measured $T_c$ and related their data to neutron diffraction studies at 5 K. The results for the transition temperature was mentioned earlier, and are shown in Fig. 24. From the neutron refinements all bond-lengths of nearest neighbour atoms in the unit cell are inferred as function of x. Comparing the two data sets, the most notable feature is an abrupt decrease (0.08 Å) in the length of the c-axis found to coincide with the appearance of superconductivity. This effect is associated with a similar abrupt decrease (0.08 Å) in the Cu(2)-O(4) distance, and a large additional puckering (0.09 Å) of the Ba-O(4) plane (Ba moving away from the $CuO_2$ plane). The other bond-lengths are less concentration dependent.

These observations all comply with a model based on the idea of a transfer of electronic holes from the basal planes to the bilayers. With increasing oxygen concentration at some point such a transfer takes place, introducing holes into the $CuO_2$ planes necessary for superconductivity. Accordingly the formal valence of the Cu(2) site will increase and a Jahn-Teller distortion takes place, the apical oxygen being drawn closer to the Cu(2) site. Simultaneously, by simple electrostatics, the barium is repulsed from the plane of the bilayers in response to the transfer of holes. It should be noted that the c-axis was also found to decrease drastically with time in the previously mentioned room temperature annealing experiments.

Next, the obtained variation with stoichiometry of the bond valence sum for the Cu(2) site is shown in Fig. 24. The bond valence sum clearly exhibits a two plateau type behaviour, with the total positive charge decreasing by about 0.08 $e$ per plane copper as $x$ decreases from 7 to 6. The data were ***not*** corrected for stress-effects. However, from our structural studies in chapter 3 we know that no singularities are present, with a possible exception at $x = 0.92$. Hence, comparing with the $T_c$ versus x data in the same figure, we conclude that there exists a strong correlation between the superconducting transition temperature and the formal valence (as expressed by the bond valence sum) of the Cu(2) copper. The plateaus coincide, and the valence is constant in the non-superconducting region. In contrast, the bond valence sum for the chain-copper is found to vary in a linear manner.

The crystal field at the rare earth site in $ReBa_2Cu_3O_{6+x}$ is also sensitive to the average charge in the $CuO_2$ planes. Based on a long series of inelastic neutron scattering measurements of the crystal field splitting levels Furrer and coworkers have managed to infer the difference as function of oxygen concentration. For a recent review see [89]. Their data confirm, that the decrease of $T_c$ between the two plateaus coincides with a transfer of approximately 0.03 electrons per Cu(2) site, and the disappearance of superconductivity with a further transfer of 0.05 electrons per Cu(2) site. Thus - relating again to Fig. 24 - it seems that the effect of the internal stress on Cu(2) bond valence sum is small, and the correlation between $T_c$ and V may therefore be interpreted in terms of a simple proportionality.

Several sets of experimental data suggest that such a linearity might be a universal property of the High $T_c$ materials, until a certain upper threshold is reached. Most notably the $\mu$SR data by Uemura and coworkers [74] indicates a correlation between $T_c$ and $n_s/m^*$, the carrier density divided by the effective mass. Their main result is reproduced in Fig. 27. Interpreting the figure simply in terms of a $T_c$ versus charge transfer plot (constant effective mass), it follows that the relationship for YBCO is linear, at least for x-values less than x=0.85. For $x > 0.85$ their data suggest transition to an "overdoped" regime.

The linear charge transfer model introduced above provides a possible decoupling between understanding the electrostatics of YBCO and describing the su-

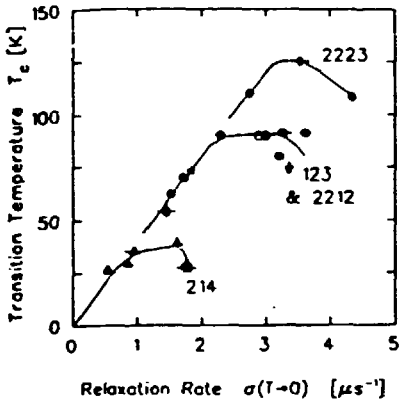


*Figure 27. $T_c$ plotted versus muon-spin-relaxation rate $\sigma(T \to 0)$ measured in sixteen different specimens of high $T_c$ superconductors. The horizontal axis is proportional to $n_s/m^*$. Triangles represent the La-system, closed circles the YBCO system, the stars double layer Bi- and Tl-compounds and the diamonds triple layer Bi- and Tl-compounds. Error bars are within the size of the symbols. Adapted from Uemura et al. [74].*

perconducting pairing mechanism. Hence, we may attempt to use conventional theoretical tools for the electrostatics. Here band-calculations will probably not provide the answer, because as discussed at length in connection with the theoretical review of the structural phase diagram, cf. chapter 2, it is hard to combine such calculations with thermodynamic averaging. Alternatively, one may attempt from simple structural chemistry arguments to deduce the charge transfer. Here, the focus has been on assigning transfer probabilities to the Cu(1) sites in the basal plane depending on the in-plane coordination number $n_{coord}$ of the copper site in question. Thus it seems natural to assign $n_{coord} = 0$ with monovalent copper, and a vanishing transfer probability. Likewise $n_{coord} = 2$ should be associated with divalent copper, and some finite probability for charge transfer, etc. However, such models based on the coordination number only have generally not been found to be able to reproduce the generic $T_c$ vs. $x$ relationship.

## 4.2 Monte Carlo Simulations of the Equilibrium $T_c$ versus $x$ Behaviour

The object is to investigate, if it is possible to explain the static variations of $T_c$ with $x$ within the framework of a linear charge transfer model, combined with structural data generated by the ASYNNNI model. A systematic survey of the possible topology of the relevant oxygen clusters in the basal plane giving rise to the charge transfer will be given.

For the model, we take the superconducting transition temperature to be directly proportional to the amount of holes transferred to the $CuO_2$ layers. We assume, that the charge transfer is a given function of the two dimensional configuration of oxygens in the basal plane, and associate each of the Cu(1) sites with a transfer probability, determined by the nature of the oxygen cluster around it within some (anisotropic) interaction range. Hence, $T_c$ can be related to a sum of independent cluster contributions $CT(\text{cluster}_i)$:

$$T_c \propto CT/A \propto \frac{1}{A} \sum_i CT(\text{cluster}_i), \tag{52}$$

where A is the total area of the basal plane considered, and CT the total amount

of charge expelled from the basal plane.

A classification is performed on basis of the interaction range: the relevant cluster type in Eq. 52 can be either 0-dimensional, 1-dimensional or 2-dimensional. In the first case the transfer probability for a given Cu(1) site is determined by its coordination number: how many of the nearest neighbour oxygen sites are occupied. In the second case the probability is a function of the length of the chains of oxygens,that bridges the particular copper site. Finally, in the third case the probability will be related to the type and area of the surrounding cluster.

The emphasis is on showing that the linearity of Eq. 52 and the inherent features of the ASYNNNI model poses strong conditions on the possible cluster dimensionality. In fact, the systematic study below will provide evidence for a specific set of clusters as the relevant ones.

### 4.2.1 Technique

Equilibrium Monte Carlo simulations are performed using a traditional Metropolis algorithm with Glauber dynamics and periodic boundary conditions on a square lattice. The normalized Sterne and Wille set of interaction potentials, $(V_1, V_2, V_3) = (-1, 0.36, -0.12)$ is used. To ensure equilibrium is reached, two simulations are in all cases run simultaneously with different initial oxygen configurations: a completely random configuration, and a completely ordered one. When - after $n_{init}$ MCS/site - the average energy and average order parameter becomes equal for the two runs, it is assumed that equilibrium is established. From this point on sampling is done for every 10th MCS/site, for a total of $n_{sampl}$ samplings. To test for finite size effects, runs with $L^2$ oxygen sites, with $L = 16, 32$ and 64 is performed. The corresponding values of $(n_{init}, n_{sampl})$ are (20000,12000), (60000,6000) and (130000,3000). With these choices the statistical uncertainties should be comparable for the three different choices of L. Results below relates to $L = 64$, unless there is a note specifying something else.

Among the thermodynamic observables sampled are the energy, the number of particles, the Ortho-I order parameter and the Ortho-II order parameter. (The order parameters are defined in the introduction, chapter 2.) Further observables sampled are results of a picture analysis of the instantaneous oxygen configuration. The picture analysis algorithm counts the number of nearest neighbour oxygens to each copper site in the basal plane (the in-plane coordination number $n_{coord}$). The average number of sites having $n_{coord} = 0, 1, 2, 3$ and 4 are sampled. The algorithm also counts the number of unbroken oxygen chains of length $l$, with $2 < l \leq L$. Finally an analysis of the distribution of Ortho-I and Ortho-II domains are performed, to be explained later. The variance of all variables are found by sampling their squared values as well.

The question of assigning the temperature remains to be answered. From our experimental investigations in chapter 3 we estimate that the oxygen kinetics freezes in between 300 K and 500 K. We choose to perform equilibrium studies for the two temperatures at the end of this interval; that is for reduced temperatures $| k_B T/V_1 | = 0.07$ and 0.11, respectively. If the simulations give the same qualitative results for the two temperatures, we will argue that the simulated oxygen configurations are representative of the experimental situation. Unless otherwise noticed, results given below are all for the case of 300 K.

### 4.2.2 Results

The ratio of Cu(1) sites with coordination numbers 0, 1 and 2 are shown in Fig. 28 as function of oxygen content. The remaining cases with $n_{coord} = 3$ and $n_{coord} = 4$ are left out, because they always represent ratios of less than 1 %, reflecting the

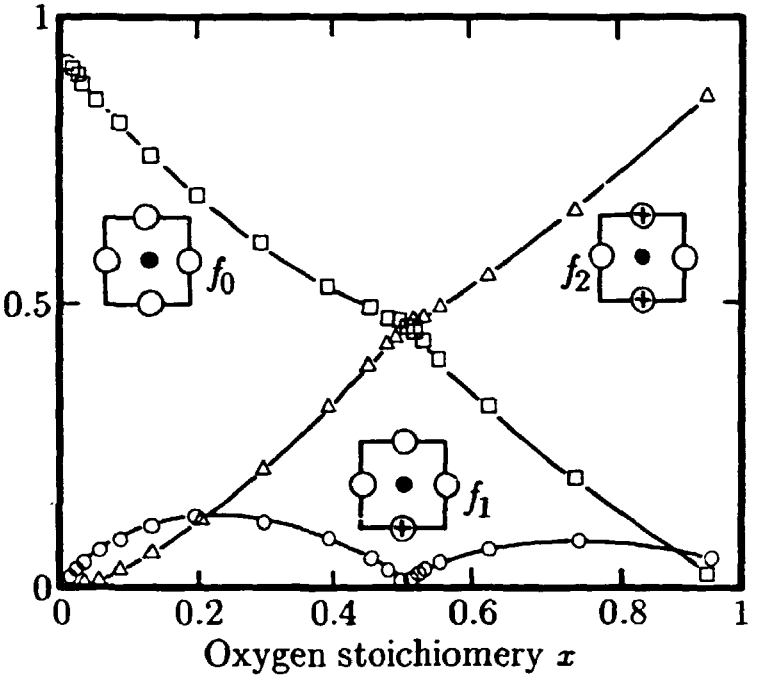


*Figure 28. Statistical analysis on the in-plane coordination number of the copper sites in the basal plane of YBCO. The ratio of copper sites with coordination numbers $n_{coord}$ = 0, 1 and 2 ($f_0$, $f_1$ and $f_2$) are given as function of oxygen stoichiometry x. The ratio of copper sites with coordination numbers 3 and 4 are vanishing throughout.*

large nearest neighbour repulsion $V_1$. To interpret the figure, we note that a coordination number of 2 represents a chain segment, while $n_{coord}$ = 1 is related to disorder appearing at the end of chains or in connection with isolated oxygens. For temperatures $k_BT < V_2$ the oxygens tend to be situated in long chains, as evidenced by the $n_{coord}$ = 2 ratio being close to 50 % and 100 % near the stoichiometric x-values of 0.5 and 1.0, respectively. At non-stoichiometric positions dynamical fluctuations of minority phases within a percolating cluster of the majority phase takes care of the concentration constraint. The majority of the $n_{coord}$ = 1 contributions arise in connection with these fluctuations. The fluctuations become dominant features near the T/OII and OII/OI phase boundaries taking place at $x \approx 0.25$ and $x \approx 0.75$, respectively. Furthermore, at sufficiently low temperatures the ASYNNNI phase diagram becomes symmetric around $x = 0.5$, cf. section 2.3.1. Hence, from theoretical arguments we expect a $n_{coord}$ = 1 ratio, nearly symmetric around $x = 0.5$ with maxima at $x = 0.25$ and $x = 0.75$, in agreement with the numeric result.

Assuming the relevant interaction range for the charge transfer process to be "0-dimensional", $T_c$ should be proportional to a linear combination of the three curves in Fig. 28, cf. Eq. 52. Invariably any such linear combination will give results that reproduce none of the generic features of the static $T_c$ versus x data ( the plateaus and the distinct cutoff near x=0.3).

The full chain length distribution is calculated. Three representative curves: the relative number of chains of minimum length, $l$ = 3, 5 and 8 are shown in Fig. 29 as function of x. It should be noted that the chains of minimum length 8 will be a subset of the chains of minimum length 3, etc. From the $l$ = 3 curve it follows that the vast majority of oxygens belong to chains. If we compare that

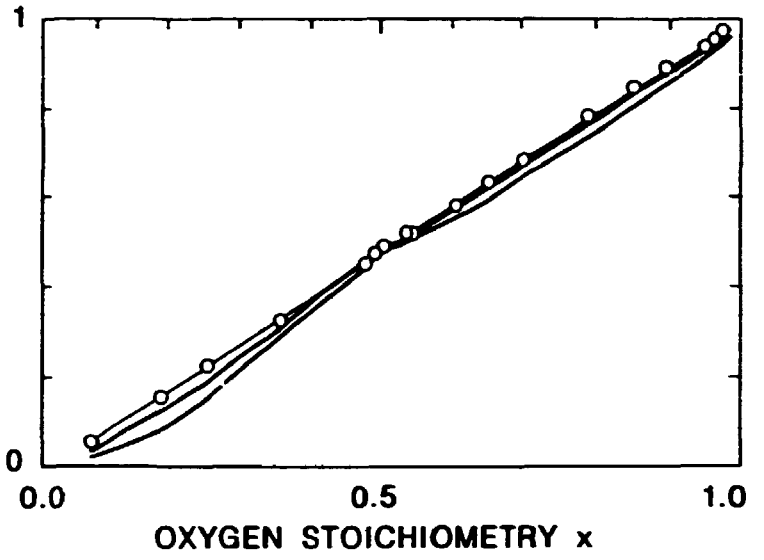


*Figure 29. Statistical analysis of the oxygen chain length distribution as function of x. The curves correspond to the number of oxygen sites belonging to a chain of minimum length l: l = 3 (above), l = 5, and l = 8 (below). The system size used is* 64 x 64.

with the $n_{coord} = 1$ curve in Fig. 28 it is clear that the entropy presents itself in terms of broken chains and not in terms of single site oxygens. Judging from snapshots of the instantaneous oxygen configuration, it is further clear that the broken chains in the orthorhombic phases are related to the boundaries between the percolating domain and the fluctuation clusters. From this observation it is easy to understand the shape of the $l = 5$ and $l = 8$ curves. At $x = 0.5$ the concentration poses no constraint on the number of fluctuations. On the other hand near the phase boundaries many fluctuations - and therefore many broken chains - will be present. The trend from the three curves shown can be extrapolated to all the other values of $l$: the higher the number of $l$, the more pronounced the spike at $x = 0.5$. Referring again to Eq. 52 we conclude that none of the possible linear combinations of the $L - 3$ curves will reproduce any of the generic features of the static $T_c$ versus x behaviour.

The most general treatment of the two dimensional case is in terms of a full cluster expansion. In this case we cannot allow every cluster-type imaginable (specified by area, shape, and intrinsic configuration) to be associated with its own freely varying contribution to the charge transfer, and take linear combinations of such contributions. Due to the number of degrees of freedom this would be meaningless. However it is possible to reduce the number of independent clusters severely by taking into account the intrinsic features of the ASYNNNI model, and assuming that nearly identical clusters may be attributed with the same average charge transfer. Actually we will argue that there exists only one physically relevant set of clusters to consider, and the occurrences for these clusters are determined by experiment.

First we note, that the ASYNNNI model at $T = 0$ contains only three types of domains: the Anti-Ortho-I type, the Ortho-II type and the Ortho-I type. Among these only the latter two have truly 2-D local coherence. At higher temperatures but still below the order/disorder transition temperature the main feature of the instantaneous oxygen configuration is the appearance of a percolating cluster of a majority type (e.g. the Ortho-II type) with dynamic fluctuations of a minority

type (either the Ortho-I type, $x > 0.5$ or the tetragonal type, $x > 0.5$) inside it. Thus also at finite temperature the ASYNNNI model contains only three types of extended domains: the tetragonal, the Ortho-II and the Ortho-I type. These domains tend to be well ordered intrinsically, especially at low temperatures, with few single site disorder points. Now as a boundary condition for the stoichiometric Ortho-I case we must have a charge transfer corresponding to $CT = T_c \cdot A = 93K \cdot A$. Similarly for the stoichiometric Ortho-II case we must have $CT = T_c \cdot A = 58K \cdot A$. Finally the tetragonal phase does not give rise to any charge transfer at all. Combining these informations we propose the following equation for determining $T_c$ given the oxygen configuration

$$T_c = \frac{1}{L^2}\left(93K \cdot \sum_{i}^{Ortho-I} A(i) + 58K \cdot \sum_{i}^{Ortho-II} A(i)\right). \tag{53}$$

Here $L^2$ is the total number of oxygen sites, while A(i) is the area of cluster number $i$. The areas are found by counting the number of oxygen sites involved (occupied or unoccupied)[12]. Thus $T_c$ is given as a weighted sum of the Ortho-I and the Ortho-II contributions, relative to the total number of oxygen sites.

Next, we define the size and shape of the clusters to be considered in Eq. 53. Here we emphasize that the clusters should be truly two-dimensional, including at least two oxygen chains. Implying isotropy we end up with *minimal size clusters equal to* $2 \times 2$ *the Ortho-I and Ortho-II unit-cells*. Hence any cluster, where all included sites belong to some square $4 \times 4$ Ortho-I sub-cluster will contribute to the charge transfer by an amount equivalent to 93 K times the number of sites in the cluster. Likewise, any cluster, where all included sites belong to some square $8 \times 8$ Ortho-II sub-cluster, will contribute to the charge transfer by an amount equivalent to 58 K times the number of sites in the cluster. All sites not included in any of these minimal size clusters will not contribute at all. To account for some thermal relaxation we permit one defect within each cluster. At the low temperatures considered, this relaxation has only a slight effect on the results.

The theoretical results for $T_c(x)$ obtained using the minimal size model and equilibrating at 300 K are shown in Fig. 30. The results for the 500 K simulation are very similar. The theoretical data are compared with two set of experimental results from Cava et al. [108], [7] in the figure. The experimental data relate to different annealing temperatures as indicated. Obviously the generic behaviour is reproduced.

We emphasize that this result does vary with the size of the minimal clusters. However for the present choice, more than 90 % of the sites belong to domains that gives rise to charge transfer, in the whole interval $0.45 < x < 1.0$. Hence, we have effectively managed to divide the oxygen configuration in two predominant classes: Ortho-I and Ortho-II, plus some minor disorder term. Using larger minimal size clusters leads to more disorder, and worse fit to the experimental data.

Finally, we mention that the lineshape of the simulated points in Fig. 30 are found to be independent of $L$ and reasonably robust towards variations of the interaction parameters.

### 4.2.3 Discussion

From the analysis above we conclude that no linear charge transfer models based on 0- or 1-dimensional clusters will be able to reproduce the generic $T_c$ vs. $x$ behaviour. For the remaining 2-dimensional case, we propose to look at the weighted

[12] It was later realized that a technically better as well as physical more intuitive way of defining the "area" of a cluster is to count the number of Cu(1) sites within the cluster. However, the results shown above are independent of this redefinition.

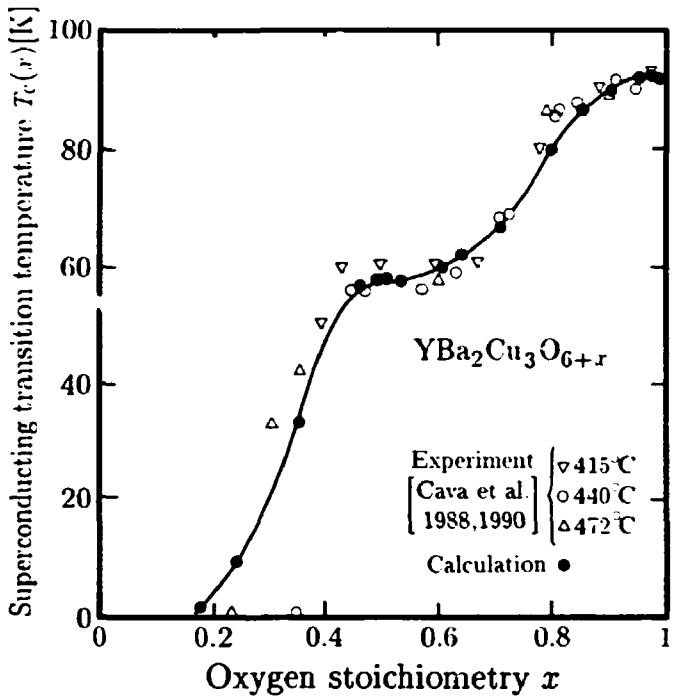


***Figure 30.*** *The variation of $T_c$ with oxygen stoichiometry, $x$. Simulations (solid circles) are performed according to the minimal size cluster model with only extended Ortho-I and Ortho-II type clusters giving rise to charge transfer. Eq. 53. Experimental data are from Cava et al. [108]. [7] (open symbols). The line is a guide to the eye.*

sum of Ortho-I and Ortho-II domains, cf. Eq. 53. This is a natural description because of the dynamic coexistence between the two structural phases. With isotropic cut-offs for the size of the clusters corresponding to a doubling 2x 2 of the unit-cells we achieve an excellent correlation with the experimental results.

The concept of minimal size clusters with a distinct cut-off between e.g. $7 \times 8$ Ortho-II clusters giving rise to no charge transfer contribution at all and $8 \times 8$ Ortho-II clusters giving rise to a full contribution should be considered a crude approximation to an unknown CT-function depending on size in a more continuous matter. Also every basal plane is sandwiched between two $CuO_2$ bilayers: the one-to-one approximation used here should be taken in an average sense. Hence, we do not wish to stress the exact agreement between theory and experiment exhibited in Fig. 30. Instead we repeat, that the emphasis in this context is on creating a minimal type model for the charge transfer based on the distinction between Ortho-I and Ortho-II domains, that comprises the thermodynamic fact of a dynamic coexistence between the two structural phases. The generics of the resulting $T_c$ vs. $x$ curve comes out successfully.

## 4.3 Monte Carlo Simulations of the Dynamic Variations of $T_c$

Few experiments have been performed to elucidate the dynamical properties of YBCO upon quenching below the order/disorder phase transition. In particular, no data exists for the time evolution of the structure factors of the oxygen ordering. Thus the magnetic susceptibility measurements by Jorgensen et al. [3], shown

in Fig. 25, is the major source of information. As previously mentioned the susceptibility data were analyzed by the Argonne group in terms of Avrami type fits. Trying to reevaluate their data within the concept of the ASYNNNI model, we note that the position $x = 0.41$ and $T = 300$ K is well within the Ortho-II phase of the phase diagram. Hence, following a fast quench nucleation and coarsening of the four degenerate types of Ortho-II domains should take place. The ASYNNNI model is nothing but an anisotropic 2D Ising model; we therefore *anticipate* the coarsening process (the growth of the domains) to behave according to the universal picture presented in the introduction to growth phenomena, section 2.5. Most notably, algebraic growth laws should apply in the late stage regime. In order to verify this and elucidate relevant growth exponentials a systematic study of the growth dynamics of ordering processes in both the Ortho-I and Ortho-II structural phases is performed. An adequate tool for such a study is again the Monte Carlo technique. Knowing the theoretical growth properties of the ASYNNNI model we may at the end try to relate this behaviour to the experimentally observed dynamical variation of $T_c$.

### 4.3.1 Technique

Quenches from infinite temperature to different temperatures well inside the Ortho-I and Ortho-II phases are simulated. In order to fix the oxygen concentration, Kawasaki dynamics is used. Simulations are performed assuming either oxygen hopping to NN sites only, or isotropic attempt-frequencies to all NN and NNN sites. The Sterne and Wille set of reduced interaction parameters $(V_1, V_2, V_3) = (-1, 0.36, -0.12)$ is used. The corresponding equilibrium phase diagram is given in Fig. 18. The simulations are carried out on a variety of different lattice sizes $L^2$. $L = 100, 180, 260$, and 400, in order to eliminate possible size effects. The results reported below are believed to be size independent. The time t is measured in Monte Carlo steps per site (MCS/site) as usual. To monitor the rate of growth we have calculated the temporal evolution of the excess energy, $\Delta E = E(t) - E(T)$, where $E(T)$ is the equilibrium energy. To check this relation we have in some cases also used a length-scale measure, $\overline{R}(t)$, derived from the full domain-size distribution function, cf. Eq. 30.

### 4.3.2 Results

The evolution of the excess energy as a function of time at $x = 0.5$ is shown in Fig. 31 for quench-temperatures $-k_B T/V_1 = 0.09, 0.07$ and 0.05. The value 0.07 corresponds to room temperature. The results relate to the case of isotropic attempt-frequencies for jumps to all NN and NNN sites. For this temperature we find an algebraic growth law behaviour with a growth exponent $n = 0.28(3)$. For the reduced temperature 0.05 the curve is initially rounded in the log-log plot. It finishes in a straight section with a slope corresponding to a growth exponent $n = 0.27(3)$. The corresponding results for $\overline{R}(t)$ are $n = 0.28(3)$ and $n = 0.27(3)$. For the higher temperature of 0.09 we find a transient of $n = 0.28(3)$ in the decade t=100 to 1000 followed by a cross-over to a value of $n = 0.37(4)$ over nearly two decades. To further elucidate the temperature dependence several simulations with low quenching temperatures are performed. For temperatures below 0.04 we find fairly low exponent values which we may attribute to crossover effects, since for $T = 0$ the system is known to freeze in and get trapped in a metastable state. For quenching temperatures above 0.09 we get too close to the structural phase transition and critical slowing down effects start to emerge.

At the stoichiometric concentration $x = 1.0$ and for intermediate temperatures, asymptotic exponent values of $n = 0.47(3)$ are observed over several decades. As

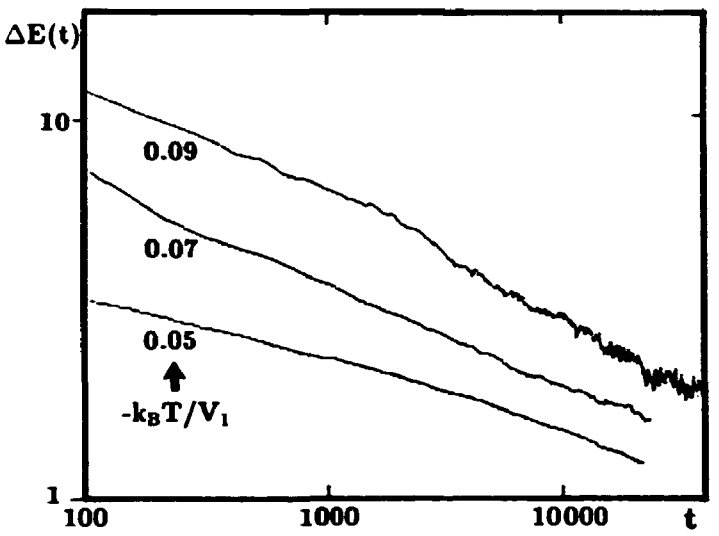


*Figure 31. Log-log plot of the excess energy $\Delta E(t)$ vs. time (given in units of MCS/site) for quenches into the Ortho-II phase at different temperatures. $k_BT/V_1$. The oxygen concentration is fixed at the stoichiometric value $x = 0.5$.*

an example, the relaxation of excess energy for the temperature $-k_BT/V_1 = 0.27$ is shown in Fig. 32 (lower curve). The growth exponent found for both $x = 0.5$ and $x = 1.0$ are robust to the specific values chosen for the reduced interaction parameters $V_2/V_1$ and $V_3/V_1$. This was tested using the "generic" values of $(-0.5, 0.5)$ introduced by Aukrust et al. [25]. The results reported above relate to NN plus NNN hopping. Analogous behaviour are found in all cases for the restricted case of NN hopping only.

To investigate the dependence on concentration of the growth dynamics we perform simulations at concentrations $x = 0.41, 0.56, 0.90, 0.96$ and 1.0. The corresponding relaxation of excess energy is shown in Fig. 32. Simulations into the Ortho-II phase are performed at a temperature close to room temperature $-k_BT/V_1 = 0.07$, while quenches into the Ortho-I phase are done at temperatures roughly corresponding to half of the pertinent orthorhombic-to-tetragonal phase transition temperature. In all cases the growth data conform to algebraic growth laws with asymptotic exponents of $n = 0.28(3), 0.29(3), 0.51(2), 0.45(3)$ and $0.47(2)$ for the series of concentrations listed above. These results all refer to the case of NN particle hopping only. Corresponding sets of data for both NN and NNN hopping are analogous for the non-stoichiometric Ortho-II series. On the contrary, for the Ortho-I series all concentrations gave rise to effective exponents of $n \approx 1/2$ for times up to $t = 1000$ MCS/site, with the stoichiometric $x = 1.0$ case as a notable exception. In the latter case $n = 0.47(3)$. We attribute the anomalously high exponent values in the non-stoichiometric Ortho-I case to transient coalescence effects[13]. We conclude that the ordering dynamics is little affected by concentration variations within $\Delta x = 0.1$ of the stoichiometric values $x = 1.0$ and $x = 0.5$.

[13] Similar transient effects are observed in the simple diluted lattice-gas model with purely NN repulsive interactions ($V_2 = V_3 = 0$).

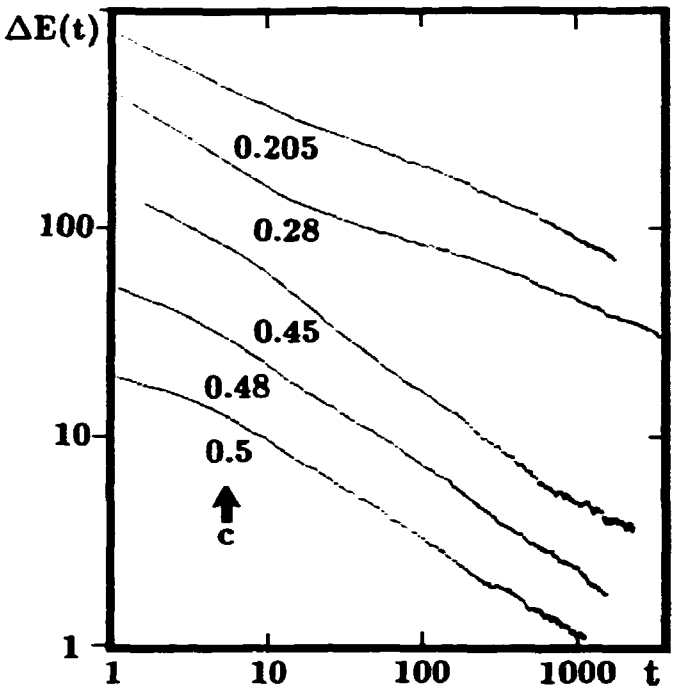


*Figure 32. Log-log plot of the excess energy $\Delta E(t)$ vs. time (in units of MCS/site) for quenches into the Ortho-II and Ortho-I phases at different oxygen concentrations $c = x/2$ as indicated in the figure.*

### 4.3.3 Discussion

The different algebraic growth laws and the associated exponents may be rationalized within the theoretical context of universality classes for late stage growth phenomena, introduced in chapter 2. Except for the well-known effect of freezing in at low temperatures caused by metastability and thermal activation [54], [60], the coherent picture which emerges from the above results is that the ordering dynamics in the Ortho-I phase is described asymptotically by an exponent $n = 0.5$ and in the Ortho-II phase by an intermediate time exponent $n = 0.25$ followed by a crossover to $n = 0.35$ at late times. The dynamics in both phases are characterized by a non-conserved order parameter. Hence one would expect the Lifshitz-Allen-Cahn growth law with $n = \frac{1}{2}$ to apply. This is consistent with our findings in the Ortho-I phase.

To understand the result for the Ortho-II case, let us look at the interface between the four types of Ortho-II domains. The interfaces can be classified according to the excess energy and excess mass per unit length, the curvature and the topology involved (whether the two domains in question are translated or rotated in relation to each other). In the late stage nearly all boundaries will be locally straight. In that case only five different types of interfaces exist; they are depicted in Fig. 33. In the late stage limit the ratio of abundance between any of these interfaces must be constant, but some types may become extinct during the initial coarsening. From an $x = 0.5$, $L = 64$ and $t = 500,000$ MCS/site simulation a limiting behaviour was found with all interface types present in non-vanishing ratios. Thus both interfaces with excess and deficit density will be present at all times. As first pointed out by Sadiq and Binder [60], the annealing of such a network with interfaces of excess and deficit densities will require transport of material over long distances. Thus the Lifshitz-Slyozov exponent $n = \frac{1}{3}$ should apply. This

is indeed consistent with our results for the asymptotic exponent. Furthermore, our finding of an intermediate time exponent value of $n \approx 0.25$ is in agreement with the exponent values observed during the transient behaviour in spinodal decomposition processes in a variety of model calculations [61]. ($n = \frac{1}{4}$ corresponds to a long-lived transient.) Finally, the effective temperature dependence of the growth exponent at $x = 0.5$, specifically with regard to the low temperature slowing down due to freezing in and the early crossover to Lifshitz-Slyozov behaviour at high temperatures, is in close analogy with the results reported by Sadiq and Binder [60] for four-fold degenerate Ising models with (2 x 1) structures which also produce domain walls with excess or deficit density.

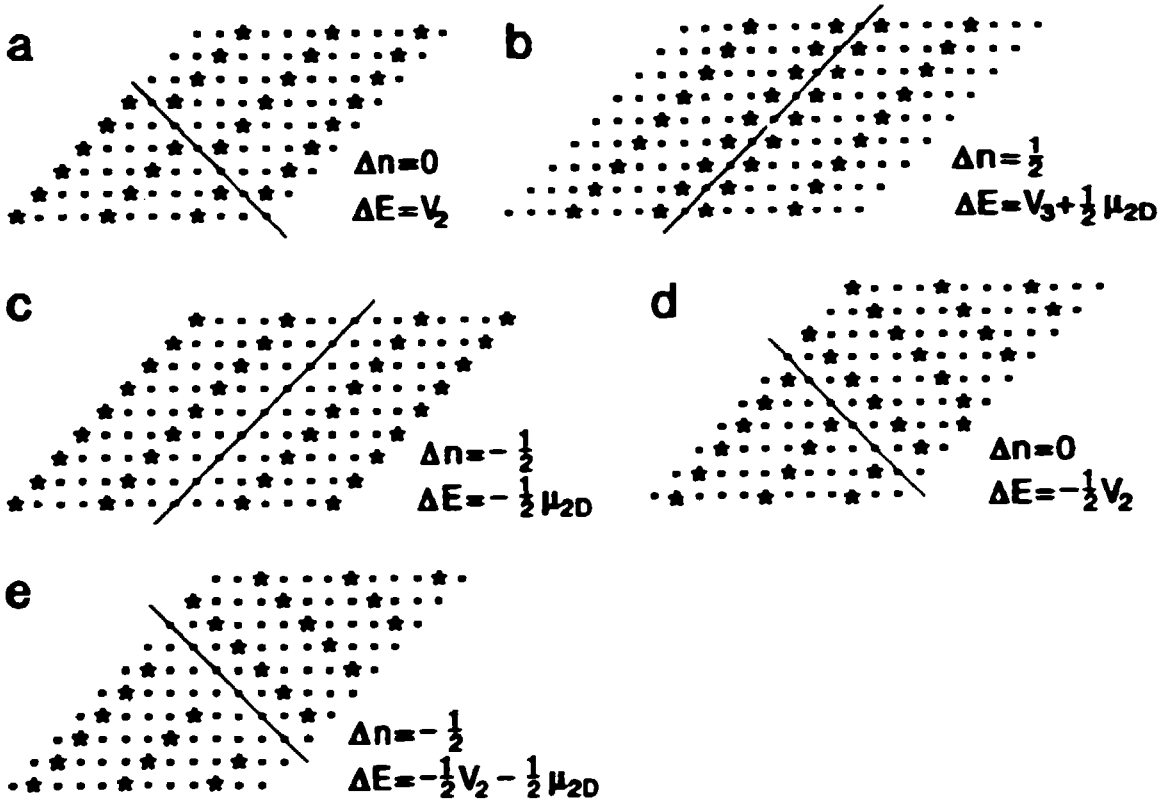


*Figure 33. The five generic types of interfaces between domains of the four degenerate Ortho-II ground-states. Only the oxygen sublattice in the basal plane is shown. The excess energy $\Delta E$ and excess number of particles $\Delta n$ per unit length of the interface are marked. Interfaces that do not conserve the density will propagate by long range diffusion mechanisms, changing the growth exponent from $\frac{1}{2}$ to $\frac{1}{3}$ in the late stage limit (see text).*

We will now return to a comparison with the experimental data of the Argonne group. In light of the findings of the model calculation above we are led to reanalyze the data in terms of an algebraic decay. Hence, we plot $\Delta T_c = T_c(t = \infty) - T_c(t)$ versus the oxygen concentration. The equilibrium transition temperature is found by simple extrapolation: $T_c(\infty) = 20.4$ K. The result of this reanalysis is shown in Fig. 34. The figure demonstrates that a power law fit with exponent $m \approx 0.54$, describes the entire set just as well as the Avrami type fits originally proposed. The experimental data in Fig. 34 should be compared with the simulation result for $x = 0.41$, the upper curve in Fig. 32. It is important to note that the exponent value pertinent to the experimental system in the Ortho-II phase is that of the transient regime of a Lifshitz-Slyozov process due to the inherent limitations of

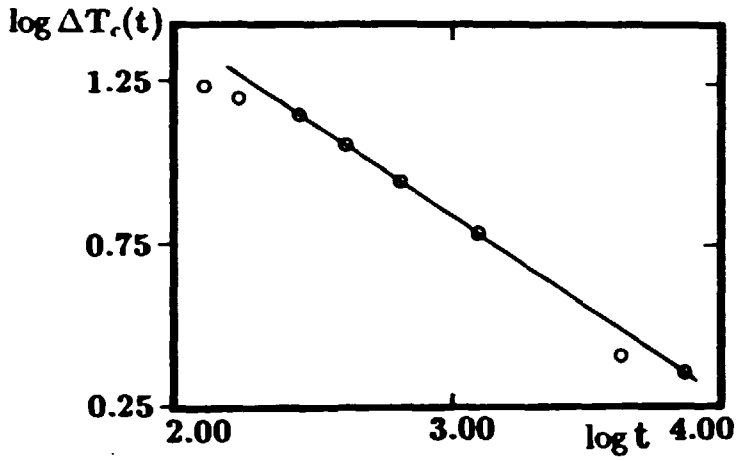


*Figure 34. Log-log plot of the relative variation, $\Delta T_c(t)$ of the superconducting transition temperature in $YBa_2Cu_3O_{6.41}$ as function of time shown as obtained from a reanalysis of the experimental data (o) due to Jorgensen et al., cf. Fig. 25. The solid line is the best power-law fit, $\Delta T_c \propto t^{-0.54}$.*

the orthorhombic crystallinity by the twin domains.

Comparing the exponents in Fig. 34 and Fig. 32 we conclude that $(\Delta T_c)^{-1}$ displays dynamical scaling with an exponent equal to the growth of the characteristic length scale $l$ squared:

$$(\Delta T_c(t))^{-1} \propto l^2(t). \tag{54}$$

This result is in excellent agreement with the linear charge transfer model based on a weighted sum of the area of the Ortho-I and Ortho-II domains, cf. Eq. 52, with $T_c$ simply growing in proportion to the growth of the area of the Ortho-II domains.[14] (There are no Ortho-I domains for $x < 0.5$.) The structural information [3] that the reordering effectively takes place within the O(1) sublattice is also reflected by the simulations. The actual site occupancy number for the O(5) site tend to be smaller then the one experimentally determined. We argue that this could be due to a systematic error in the Rietveld refinement or to the existence of "bad sectors" in the sample.

The combined experimental and theoretical study of the structural phenomena in YBCO reported in chapter 3 lead to some precautions in the present case. Firstly, the analysis strongly suggested NN hopping to be the correct description of the diffusion process. Accordingly, the simulations used for comparison with the experimental data included NN hopping only. Secondly, the effect of the formation of the twin domains are neglected in our simulations. However, we may argue on basis of universality that the same growth exponents should apply independently of the interaction of the internal strain. Notice, that this argument may not be valid for quenches *into* the Ortho-II from within the Ortho-I regime ($x > 0.5$). In that case the degree of degeneracy is effectively reduced to two, as argued in section 3.4.3, and the above analysis of the generic interfaces between degenerate domains will not hold. An effective $n = \frac{1}{2}$ growth exponent might be the result.

[14] The initial deviation from the straight line in the experimental data in Fig. 34 ($T_c(t) = 0$ for $t < 2$ hours) is not reflected in the simulation data for $\Delta E(t)$ in Fig. 32. This is due to the fact that early on the excess energy is not proportional to the total perimeter, and not a contradiction of the relationship in Eq. 54. Using a better length scale for the initial stage like $\bar{R}(t)$ the proportionality is apparent at all time scales.

## 4.4 Discussion

From the simulations of the dynamics of the ASYNNNI model we conclude that the oxygen ordering process in YBCO will conform to the universal picture of growth kinetics reviewed in section 2.5. This result is based on basic physical principles of scaling symmetries in non-equilibrium systems, and is unlikely to be influenced by perturbations of the structural phase diagram, including introduction of internal strain or phase separation. (Additional phases will have growth exponents according to the structure of the interfaces present). This theoretical prediction makes YBCO an ideal material for studying growth phenomena of low dimensional systems. Whereas the experimental study of time-dependent ordering processes in three-dimensional systems is well developed, only recently have detailed time-resolved studies been conducted for surface systems. These studies are so far limited to the late-stage ordering processes of oxygen chemisorbed on tungsten surfaces [90]. Experimentally such studies are not very error-prone, evaporation and stacking often destroys the two dimensionality of the systems, the LEEDS probes interact with the media, it is hard to make fast quenches and to start out with homogeneous configurations. Thus so far the derived "algebraic growth laws" have been based on at most a single decade in time resolution. Provided it is possible to find an experimental handle on the YBCO system these problems would all be absent.

The finding of the same scaling symmetry in two different material properties, oxygen ordering and superconductivity, is unlikely to be accidental. Thus the correlation strongly suggests a specific coupling between the coherent oxygen order and the superconducting state of the material. This conclusion is reached independent of whether or not a charge transfer model applies.

Next, the combined analysis of the equilibrium and dynamic properties of the ASYNNNI model provides evidence that within a linear charge transfer model the static and dynamic variations of $T_c$ can only be rationalized if the description is based on extended ordered domains, and if the coexistence between the Ortho-I and the Ortho-II type of domains is taken into account. A minimal model, based on minimal size clusters, gives a surprisingly good quantitative agreement with the experimental set of data.

We will propose an interpretation of the phenomenological minimal size cluster model in terms of a stress relaxation effect originating in the displacements of the apical oxygen. In the metallic state the "kinetics" of the holes in the $CuO_2$ plane corresponds to thousands of Kelvins. Hence it is clear that at ambient temperature the apical oxygen will only "see" the average charge in this plane. The optimal position of the apical oxygen will thus be determined by this constant term plus a site dependent term related to the oxygen cluster situated around the Cu(1) site just below the apical oxygen in question. Due to the effects of the internal strain the apical oxygens cannot move independently. The structural coherence needed for charge transfer is thus associated with the coherence in the lateral position of the apical oxygens.

Finally, we note that the minimal clusters proposed correspond to the transfer of roughly one electron per cluster. Thus, it is known from the work of Cava [7] and others, that the average charge transfer per oxygen site in the basal plane in fully oxidized samples is 0.08 $e$. Assuming a charge transfer of 1 hole per 16 sites, the area of a minimal Ortho-I cluster, the simulations give 0.06 $e$. Similarly for the 60 K plateau, the simulations give $\approx 0.02e$, to be compared with the experimental value of 0.05 $e$.

The most obvious candidates for an extension of the minimal size cluster model are the rare earth substituted compounds: $ReBa_2Cu_3O_{6+x}$. It is well known that the superconducting transition temperature for the fully oxidized compounds in

this series varies very little (The tetra-valent or mixed-valent ions like *Pr* make an exception: they are semiconductors for all $x$). Likewise, the differences of the lattice parameters can be accounted for simply on basis of the variations in ionic radia [91]. Hence, we might expect the ASYNNNI model to be valid, and the effect of Re-substitution to amount to a reparametrisation of the interaction parameters plus some internal strain effects. The plateaus in the $T_c$ vs. $x$ behaviour will maintain. If this picture turns out to be true, important information on both the relationship of $V_i$: $i = 1, 2, 3$, vs. strain and $T_c$ vs. strain may be obtained. However, there are some evidence in the literature of more pronounced variations. Thus, the *Nd*-compound exhibits a parabolic $T_c$ vs. $x$ behaviour [92], possibly connected to a disappearance of the Ortho-II phase. Provided careful experimental work on the structure of these compounds are[15] carried out, they will constitute a crucial test of the minimal size cluster model.

Another interesting extension is to consider $YBa_2Cu_{3-y}M_yO_{6+x}$, where $M$ substitutes for the Cu(1) site only. Fe, Co and Al are believed to have this property [93], [94], [95], [96]. Here Al is arguably the simpler compound to understand because it has a fixed valence $Al^{3+}$, while Fe and Co in general will be mixed-valent. Provided the dependence of $x$ on $y$, the question of whether the M-ions will tend to order or not, and the variation of the internal strain with $y$ are experimentally settled, comparisons may be performed to extended models for the oxygen ordering process, where the coordination around the M-ion is taken into account. (Because ambient temperature is the relevant temperature for such considerations, it is not necessary to estimate the size of any new interaction parameters related to the oxygen-oxygen interaction in the vicinity of the M-ion. Arguments based on the $T = 0$ variation of $\mu_{2D}$ with $y$ will apply.) Such models are in progress. If they become successfully established, it may again be relevant to discuss the nature of the charge transfer process.

The only other family of copper-oxide superconductors, where the oxygen ions play the role of dopants connected with the rock-salt layer (in contrast to defects in the $CuO_2$ layers) is represented by the compound $Pb_2Sr_2Y_{1-x}Ca_xO_{8+\delta}$ [97]. In this case the oxygen content is variable in the interval $0 < x < 1.6$. Simultaneously, the Ca-content is varaible: $0 < y < 1$. Here, the major changes upon doping are caused by the mixed-valency of Pb. As a consequence, both the structural and superconducting schemes are fundamentally different from the YBCO case, the superconducting transition temperature as an example is decreasing with increasing oxygen content.

There are several reasons that the charge transfer concept may ultimately fail. Most notably, the structure may couple directly to the pairing mechanism. However, a discussion of the various models for the normal or the superconducting state in the copper-oxides, and their specific relation to structural coherence is beyond the scope of this thesis. Still, we would like to comment on some recent theoretical work due to Kresin and coworkeres, that in rather general terms points to a possible effect of the anisotropy of the materials.

Kresin et al. [98] note that - within an Eliashberg formalism - the short superconducting coherence length along the $c$-axis may lead to a two gap structure in YBCO and other high $T_c$ materials. The $CuO_2$ bilayers in their model are characterized by intrinsic pairing, whereas the proposed superconducting state of the basal plane is induced by two different transfer channels for Cooper pairs (intrinsic proximity effect and phonon mediated transfer). This important observation has naturally attracted some interest lately, but the question remains whether there is experimental evidence for a gap associated with the basal plane. Here, Barett et

[15] Notice, the internal strain varies with the size of the RE-ion. Hence it is likely that the fully oxidized compounds correspond to different $x$-values for different RE-substitutions. This might lead to systematic errors, when comparing values in the literature.

al. [99], reports on NMR measurements on the $^{63}Cu$ Knight shift of $YBa_2Cu_3O_7$. The Knight shift was used to measure the electron-spin susceptibility $\chi^S(T)$ as a function of temperature in the superconducting state relative to the normal-state spin susceptibility. The component of $\chi^S(T)$ originating at the Cu(1) site apparently follows a conventional weak-coupling BCS form with a gap given by $2\Delta(T = 0) = 3.5k_BT_c$. (The other gap having a value ranging between 1.9 and 3.1 $k_BT_c$.) Also the tunneling data by Gurvitch et al. [100] suggests two gaps (not necessarily associated with planes and chains, but one possibly with the a-b plane and the other with the c-axis). Clearly more experimental work is needed, and it might be helpful to consider experiments like room temperature annealing in order to unambiguously identify the nature of e.g. the $^{63}Cu$ Knight shift.

Kresin et al. [98] further sets up a three parameter model, that for specific values of the parameters gives rise to a $T_c = T_c(x)$ dependency that mimics the 90 K "plateau". The parameters are not easily accessible to experiments. In order to explain the 60 K "plateau" the authors have to introduce a second ordered phase around $x = 0.7$ while the Ortho-II phase should be non-existent or negligible. Finally we note that the Kresin model still implies transfer of charge, cf. the dynamic experiments by Veal et al.

## 4.5 Conclusion

The dynamics of oxygen ordering in the ASYNNNI model is found to be characterized by algebraic growth laws with exponent values which depend on whether the evolving order is of the Ortho-I or the Ortho-II type. $YBa_2Cu_3O_{6+x}$ is therefore, by virtue of its extreme anisotropy with respect to oxygen diffusion, an unusually interesting candidate for studying aspects of dynamical scaling in low dimensional systems.

A reanalysis of the data by Jorgensen et al. [3] reveals that the same scaling symmetry applies to the time-evolution of the experimental $T_c$ values as to the evolution of the simulated areas of the Ortho-II domains in the ASYNNNI model. The simulated result is based on universal properties of domain growth, and the correlation between two very different materials properties is therefore unlikely to be accidental. Hence, our findings strongly suggest a specific coupling between the coherent oxygen order and the superconducting state of the material. This conclusion is reached independent of whether or not a charge transfer model applies.

Next, the combined analysis of the equilibrium and dynamic properties of the ASYNNNI model provides evidence that within a linear charge transfer model the static and dynamic variations of $T_c$ can only be rationalized if the description is based on extended ordered domains, and if the coexistence of the Ortho-I and the Ortho-II type of domains is taken into account. A minimal model is proposed, where the total charge transfer is found as a weighted sum over the areas of the Ortho-I and the Ortho-II domains, and the minimal size of the two types of domains are given by a doubling of the unit-cells. The minimal model gives a surprisingly good quantitative agreement with the experimental set of data. An explanation for the need of structural coherence in terms of relaxation effects related to the apical oxygens is offered.

# 5 Acknowledgements

It is a pleasure to take this opportunity to thank colleagues and friends who have been inspiring, supportive, helpful and sometimes overbearing during my time as a PhD student.

I am first of all grateful to my primary supervisors Niels Hessel Andersen and Mourits Nielsen, who have inspired and guided me throughout, always in a very kind and competent fashion. Whatever technical skills I may have picked up, I learned from them.

My sincere thanks to Ole Mouritsen, who has managed to build an extremely active and cross-disciplinary group. The open-minded and creative atmosphere I have witnessed during my stay at his department is pure gasoline for any young researcher. Also Ole Mouritsen have been most kind introducing me to the field of soft matter. I definitely wish to thank two other members of his group: Jørgen Vitting Andersen and Henrik Bohr for what I think has been a very pleasant and yet exciting collaboration.

I am grateful to my other supervisor Per Hedegård for his interest in my work and for arranging the formalities related to my PhD study.

I thank Bente Lebech for helping me in many practical matters, and teaching me a bit of crystallography. Further thanks to Per Anker Lindgård for his very competent explanations of theoretical issues, and for setting up a study group at Risø. The discussions with him, Thomas Fiig and Eduard Vives have been most rewarding. Especially I would like to thank Thomas for many interesting ideas and suggestions.

I am very grateful to Bob Cava who was my supervisor during my leave for AT&T Bell Laboratories. It is truly awesome to work with Bob, and although I am not a materials scientist, the techniques and methods he taught me will always be useful. More importantly though, I thank him for sharing part of his deep insight in physical chemistry with me.

The expert assistance of secretaries and technicians in the Physics Department at Risø is gratefully acknowledged. In particular I want to thank W. Kofoed, Mourits Lund, Allan Thuesen and Keld Theodor for helping me with various odd jobs. The secretaries Lajla Frederiksen and Margit Kloster have been most helpful and supportive throughout. For her skilled assistance in preparing figures of this thesis I am grateful to Tora Skov.

I thank a number of other people for advice, questions, comments and technical assistance: J. Jorgensen, J. Krajewski, W. Peck Jr., M. Altarelli, J. Als-Nielsen, and K. Clausen. Furthermore, I thank the Danish Research Academy for a grant and for financial support in connection with my stay at Bell Laboratories. Also, support from the Danish Ministry of Energy and the Materials Development Program for High Tc Superconductivity is gratefully acknowledged.

Finally I thank friends and family for their support and acceptance of my long working hours. Without it, this work would never have been made.

# 6 Appendix A: Theoretical Description of the In-diffusion Process

The object of this appendix is to derive an exact equation for the in-diffusing particle flux as function of time for the specific experimental set-up presented in section 3.3.4. Approximations will be given that lead to a simple exponential decay-rate, and a discussion on the validity of these approximations offered. In the end a comparison with the experimental results is given. We will focus on a the diffusion of a single twin-domain of YBCO, and assume that no absorption on the surface takes place. Similarly we will neglect the surface barriers, taking the intrinsic diffusivity to be smaller than or comparable to the surface diffusivity term.

The thermal relaxation process will be orders of magnitudes faster than the kinetics governed by the particle-vacancy exchanges in the interior. Thus the diffusion process is driven by the difference in chemical potential $\mu_{int}$ inside the sample. The coupling to the environment is in form of a constraint, that the chemical potential at the surface of the sample should be equal to the external chemical potential $\mu_{ext}$. Initially, at $t = 0$, $\mu_{ext}$ will be higher than the (constant) internal field $\mu^0_{int}$, leading to in-diffusion of particles. Due to the other constraint of mass conservation the following rise of the average $\mu_{int}$ with time will take place simultaneously with a lowering of $\mu_{ext}$. At any time after the quench, we will therefore have an anisotropic distribution of chemical potential and particle concentration, $c$, inside the sample, with maxima at the surface and minima at the center of the sample. In this context, both $\mu_{int}$ and $\mu_{ext}$ should be understood as three dimensional molar O entities. Comparing to Eq. 38

$$\mu_{ext} = \frac{1}{2}\mu(O_2) = \frac{1}{2}RT\ln(P/P_0) + \mu_{ext}(t=0); \tag{55}$$

$$\mu_{int} = N_A(\mu_{2D} + V_0 + \frac{\partial E_{ph}}{\partial N}). \tag{56}$$

$P_0$ is the pressure in the molecular gas immediately after the quench.

Fick's first law applied to the flow of particles of a substitutional alloy in an isothermal chemical gradient reads (cf. Flynn [101])

$$\bar{J} = -\bar{\bar{D}}^* rc\nabla\mu_{int} \tag{57}$$

$$= -\bar{\bar{D}}^* rc\frac{\partial\mu_{int}}{\partial c}\nabla c \tag{58}$$

$$= -\bar{\bar{D}}_m\nabla c, \tag{59}$$

where $\bar{J}$ is the net flux af particles (in mole/$cm^2$), $D^*$ the self diffusion matrix of a tracer (in units $cm^2$/s), $D_m$ the mutual diffusivity matrix and $r = r(c)$ the vacancy wind factor. Next, we choose a coordinate system (x,y,z) corresponding to the principal axes (a,b,c) of the crystal. The **local** symmetry will generally be orthorhombic, and Neumann's principle therefore imply, that the three diagonal elements in the diffusivity tensors will be different, while the off-diagonal elements are zero. The anisotropy ratio between diffusion along the c-axis and in the (a-b)-plane has been measured by Rothmann et al. [8], [67] to be $10^{-6}$. For all practical purposes we may therefore set $D^{zz}$ to 0, and operate with two-dimensional models only. In the following we will consider a single crystal of volume $V = L \times L \times H$ (the value of H is immaterial).

Applying mass conservation ($\frac{\partial c}{\partial t} = -\nabla \cdot \bar{J}$) we arrive at the following partial differential equation

$$\frac{\partial c}{\partial t} = D_m^{xx}(c)\frac{\partial^2 c}{\partial x^2} + D_m^{yy}(c)\frac{\partial^2 c}{\partial y^2}; \text{ in the bulk, } t > 0. \tag{60}$$

$$c(x,y,0) = c_0; \text{ in the bulk.} \tag{61}$$

$$\mu_{int} - \mu_{int}^0 = \frac{RT}{2}\ln\left(\frac{N - \bar{c}V}{N - c_0 V}\right); \text{ at the surface, } t > 0. \tag{62}$$

with $\bar{c}(t) = \int c(x,y,t)dxdy$, and N the total number of oxygen atoms in the sample as well as the environment. The bulk will be taken as the area $(x,y) \in [0,L] \times [0,L]$. To be able to solve the set of equations an additional relation specifying the equilibrium $\mu_{int} = \mu_{int}(c)$ dependency must be provided. The last boundary equation may then alternatively be formulated

$$\frac{dc}{dt} = -\frac{RTV}{2(N - \bar{c}V)}\left(\frac{d\mu_{int}}{dc}\right)^{-1}\frac{d\bar{c}}{dt}. \tag{63}$$

Having solved the differential equation for $c = c(x,y,t)$ we get the following expression for the relaxation of the pressure in the exterior:

$$P(t) = P_0 + (P_1 - P_0)\left(1 - \frac{c_1 - \bar{c}(t)}{c_1 - c_0}\right). \tag{64}$$

$P_1$ is the final pressure $P_1 = P(t = \infty)$. Similarly for the particle flux through a unit area of the surface at time $t$

$$J(t) = -L/4 \cdot \frac{d\bar{c}}{dt}. \tag{65}$$

It is not possible to solve the partial differential equation above in a closed form. Note, that the tracer diffusion coefficient itself, $D^*$, will be concentration dependent, in particular it will dependent on the nature of the structural phase(s) present. Thus, unless experiments are run under circumstances that allow for simplifications data analysis is at best a very tedious endeavor. To enable such simplifications we notice first, that the non-linearity may be suspended by performing the quenches in small temperature steps, effectively operating in a quasi-stationary mode. In that case the absolute variations in c will be small, and provided $\mu_{int} = \mu_{int}(c)$ is a smooth function, we may approximate by a partial differential equation with constant coefficients. If we for the time being consider the analogous one-dimensional case:

$$\frac{\partial c}{\partial t} = D_m\frac{\partial^2 c}{\partial x^2} \qquad 0 < x < L/2,\ t > 0. \tag{66}$$

$$c(x,0) = c_0; \qquad 0 < x < L/2. \tag{67}$$

$$\frac{dc}{dt}(0,t) = -A\frac{d\bar{c}}{dt}, \qquad t = 0. \tag{68}$$

$$\frac{\partial c}{\partial x}(L/2,t) = 0 \qquad t > 0. \tag{69}$$

When the relative number of moles of oxygen in the environment becomes much larger than the number of moles in the sample ($N \to \infty$ in Eq. 63) the environment will effectively behave as a particle-bath and we may substitute the boundary condition by simply

$$c(0,t) = c_1 \tag{70}$$

Obviously Eq. 69 then reduces to an equation, where we can separate the variables. The result for $x < L/2$

$$c(x,t) = c_1 + \sum_1^{\infty} b_n \exp(-(n-1/2)^2 4\pi^2 D_m t/L^2) \sin((n-1/2)2\pi x/L) \quad (71)$$

$$b_n = \frac{4}{L}\int_0^{L/2} (c_0 - c_1)\sin((n-1/2)2\pi x/L) \quad (72)$$

$$= \frac{2}{\pi}(c_0 - c_1)\frac{1}{(n-1/2)} \quad (73)$$

Inserting in Eq. 64

$$P(t) = P(0) + (P_1 - P_0)\left(1 - \frac{8}{\pi^2}\sum_{n=1}^{\infty}\frac{1}{(2n-1)^2}\exp(-4\pi^2(n-1/2)^2 D_m t/L^2)\right) \quad (74)$$

For late times all the higher harmonics will have died out and we end up with the expected exponential decay rate for the external pressure:

$$P(t) = P(0) + (P_1 - P_0)\left(1 - \frac{8}{\pi^2}\exp(-\pi^2 D_m t/L^2)\right). \quad (75)$$

In Fig. 35 the the difference between the time dependence of P(t) evaluated using Eq. 74 and the approximation Eq. 75 is illustrated. $4\pi^2 D_m/L^2$ as well as $P_1$ has been set to 1. and $P_0$ to 0. We observe that the approximation to a single exponential is excellent when $(P(t) - P(\infty))/(P(0) - P(\infty)) < 0.7$.

This limit on the validity of the first-harmonics approach and the above conclusions are easily generalized to two dimensions. Thus the equivalent of Eq. 74 is

$$P(t) = P(0) + (P_1 - P_0)(1 - \alpha) \quad (76)$$

$$\alpha = \frac{8^2}{\pi^4}\sum_{m=1}^{\infty}\sum_{n=1}^{\infty}\frac{1}{(2m-1)^2(2n-1)^2}\exp(-(D_m^x(m-1/2)^2 + D_n^x(n-1/2)^2)4\pi^2 t/L^2) \quad (77)$$

(78)

Likewise, the equivalent of Eq. 74 is

$$P(t) = P(0) + (P_1 - P_0)\left(1 - \frac{8^2}{\pi^4}\exp(-\pi^2(D_m^x + D_m^y)t/L^2)\right). \quad (79)$$

Next, we will determine a criteria for the validity of the approximation involved in setting $\mu_{ext}$ equal to a constant. We will demand that the total change in concentration at the surface between the final value (at $t = \infty$) and the value just after the quench (at $t = 0+$) should be much less than the similar change in the average bulk concentration, $\bar{c}$. Integrating Eq. 63 we get

$$\ln(\frac{P_1}{P_0})/(P_0 - P_1) << \frac{2}{(RT)^2}\frac{V_{ext}}{V}\cdot\frac{d\mu_{int}}{dc} \quad (80)$$

$V_{ext}$ is the exterior volume of the ideal gas.

Finally, we perform a comparison with the experimental set of in-diffusion data presented in section 3.3.4. $\frac{d\mu_{int}}{dc}$ can be estimated from the equilibrium partial pressure measurements, because $\mu_{int} = \frac{1}{2}\mu(O_2)$. For the experiment $V_{ext} = 392cm^3$ and $V = 8.1cm^3$. Inserting, we obtain

$$\ln(\frac{P_1}{P_0})/(P_0 - P_1) << \frac{189}{T^2}\cdot\frac{\partial\mu_{int}}{\partial c} \quad (81)$$

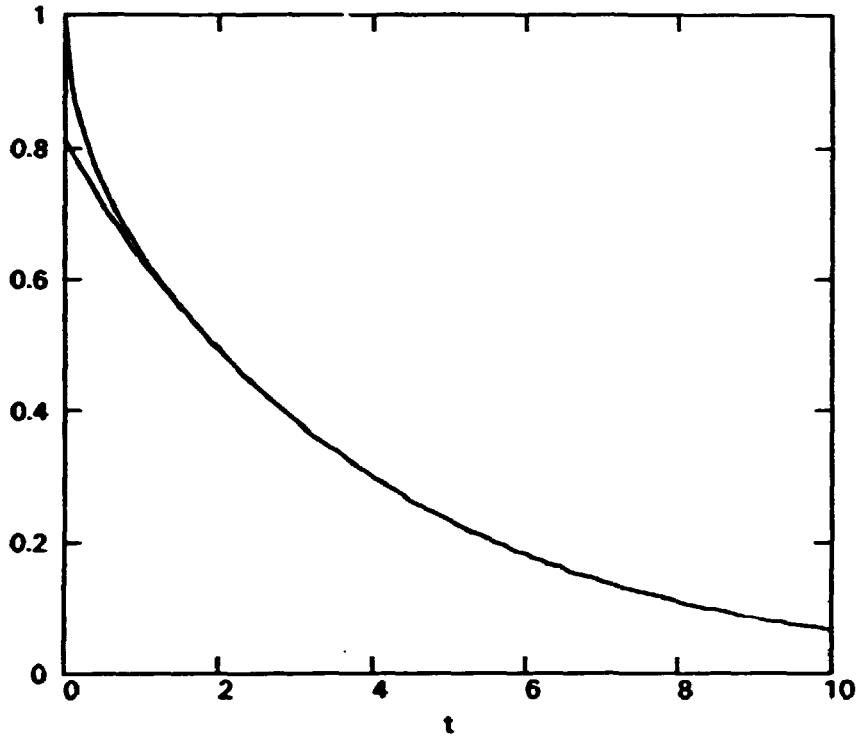


*Figure 35. Comparison between the time dependence of the external pressure evaluated according to Eq. 74 and Eq. 75 with* $4\pi^2 D_m/L^2 = P_1 = 1$ *and* $P_0 = 0$.

with P in Torr, T in Kelvin, and the derivative of the chemical potential in units of $Jcm^3/mol$. For a typical example (from trace no. 13) of $T = 517°C$, $P_0 = 80.5$ Torr, and $P_1 = 65.8$ Torr, we have $\frac{d\mu_{tot}}{dc} =$.

The prominent kinks in all the Arrhenius plots for $\tau$, c· Fig. 17, are analyzed and found to coincide with a very good resolution to the temperature where the pressure relaxation achieved at the beginning of the pressure monitoring (17 min after the quench) P(17 min) is related the (fitted) total pressure relaxation by $(P(17min) - P(\infty))/(P^{\prime} \cdot P(\infty)) \simeq 0.75(5)$. Comparing with Fig. 35 this is a strong argument that the deviations from a straight line in the Arrhenius plots are due to the fact, that higher harmonics should be included in the analyses.

# References


[1] J.G. Bednorz and K.A. Muller. Z. Phys B **64** (1986), 189.

[2] J. Ranninger. Z. Phys. B **84** (1991), 167.

[3] J.D. Jorgensen, S. Pei, P. Lightfoot, H. Shi, A.P. Paulikas and B. W. Veal. Physica C **167** (1990), 571.

[4] B.W. Veal, H. You, A . Paulikas, H. Shi, Y. Fang and J.W. Downey. Phys. Rev. B **42**, 10 (1990), 6305.

[5] J.D. Jorgensen, M.A. Beno, D.G. Hinks, L.Soderholm, K.J. Volin, R.L. Hitterman, J.D. Grace, I.K. Schuller, C.U. Segre, K. Zhang, and M.S. Kleefisch. Phys. Rev. B **36** (1987), 3608.

[6] B. Batlogg. Preprint.

[7] R.J. Cava, A.W. Hewatt, E.A. Hewatt, B. Batlogg, M. Marezio, K.M. Rabe, J.J. Krajewski, W.F. Peck Jr. and L.W. Rupp Jr. Physica C **165** (1990), 419.

[8] S.J. Rothman, J.L. Routbort and J.E Baker. Phys. Rev. **B40** (1989), 8852.

[9] J.D. Jorgensen, B.W. Veal, A.P. Paulikas, L.J. Nowicki, G.W. Crabtree, H. Claus and W.K. Kwok. Phys. Rev. B **41**,4 (1990), 1863.

[10] J. Karpinski, S. Ruseicki, E. Kaldis and E. Jilek. In: Proceedings of E-MRS Spring Conference, Symposium A: High Tc Superconductor Materials. Ed: H.-U. Habermeier, E. Kaldis and J. Schoenes. Strassburg, 1990.

[11] R. Bormann and J. Nolting. Appl. Phys. Lett. 54 (1989), 2148.

[12] P.K. Gallagher, H.M. O'Bryan, S.A. Sunshine, and D.W. Murphy. Mat. Res. Bull. **22** (1987), 995. A. Manthiram, J.S. Swinnea, Z.T. Sui, H. Steinfink, and J.B. Goodenough. J. Am. Chem. Soc. **109** (1987), 6667. I.K. Schuller, D.G. Hinks, M.A. Beno, D.W. Cappone II, L. Soderholm, J.-P. Locquet, Y. Bruynseraede, C.U. Segre, and K. Zhang, Solid St. Comm. **63** (1987), 385.

[13] J.A. Gardner, H.T. Su, A.G. McKale, S.S. Kao, L.L. Peng, W.H. Warnes, J.A. Sommers, K. Athreya, H. Franzen, and S.-J. Kim. Phys. Rev. B **38** (1988), 11317.

[14] R.M. Flemming et al. Phys. Rev. B **41** (1988), 7920.

[15] T. Zeiske, R. Sonntag, D. Hohlwein, N.H. Andersen and T. Wolf. Nature **353** (1991), 542.

[16] R. Sonntag, D. Hohlwein, T. Bruckel and G. Collin. Phys. Rev. Lett. **66** (1991), 1497.

[17] A.A. Aligia and C. Ventura. Phys. Rev. Lett. **65** (1990), 2475.

[18] R. Beyers, B.T. Ahn, G. Gorman, V.Y. Lee, S.S.P. Parkin, M.L. Ramirez, K.P. Roche, J.E. Vasquez, T.M. Gur, and R.A. Higgins. Nature **340** (1989), 619.

[19] J. Reyes-Gasga, T. Krenkels, G. Van Tendeloo, J. Van Landuyt, W.H.M. Bruggink, M. Verweij and S. Amelinckx. Solid St. Commun. **70** (1989), 269.

[20] J. Reyes-Gasga, T. Krenkels, G. Van Tendeloo, J. Van Landuyt, W.H.M. Bruggink, M. Verweij and S. Amelinckx. Physica C **159** (1989), 831.

[21] D. de Fontaine, L.T. Wille, and S.C. Moss. Phys. Rev. B **36** (1987), 5709.

[22] L.T. Wille and D. de Fontaine. Phys. Rev. B **37** (1988), 2227.

[23] J. Stoltze. Phys. Rev. Lett. **64** (1990), 970.

[24] M. Inoue, T. Takenori, and T. Sakuda. Jap. J. Appl. Phys. **26** (1987) L2015.

[25] T. Aukrust, M.A. Novotny, P.A. Rikvold, and D.P. Landau. Phys. Rev B **41** (1990), 8772.

[26] L.T. Wille, A. Berera, and D. de Fontaine, Phys.Rev.Lett. **60** (1988), 1065.

[27] Bortz, Kalos and Lebowitz. J. Comp. Physics **17** (1975), 10.

[28] R.H. Swendsen and J.S. Wang Phys. Rev. Lett. **58**, 86.

[29] A.M. Ferrenberg and R. Swendsen. Phys. Rev. Lett. **23** (1988), 2635.

[30] J. Lee and J.M. Kosterlitz. Phys. Rev. B **43** (1991), 3265.

[31] J.W.D. Connolly and A.R. Williams. Phys. Rev. B **27** (1983), 5169.

[32] P. Sterne and L.T. Wille. Physica C **162-164** (1989), 223.

[33] G. Ceder, M. Asta, W.C. Carter, M. Kraitchmann, D. de Fontaine, M.E. Mann and M. Sluiter. Phys. Rev **B41** (1990), 8698.

[34] N.C. Bartlett, T.L. Einstein and L.T. Wille. Bull. Am. Phys. Soc. **34** (1989), 598.

[35] D. de Fontaine, G. Ceder, and M. Asta. Nature **343** (1990), 544.

[36] J. Hubbard. Phys. Rev. B **17** (1978), 494. V.L. Pokrovsky and G.V. Uimin. J. Phys. C. Solid St. Phys. **11** (1978), 3535.

[37] D. de Fontaine. J. Phys. A: Math Gen. **17** (1984), L713.

[38] Ceder, M. Asta, and D. de Fontaine. Preprint.

[39] C.P. Burmeister and L.T. Wille. Phys. Rev. B **40** (1989), 8795.

[40] C.P. Burmeister, M.E. Mann, G. Ceder, L.T. Wille, and D. de Fontaine. Physica C **162-164** (1989), 225.

[41] A.A. Aligia, A.G. Rojo, and B.R. Alascio. Phys. Rev. B 38 (1988), 6604.

[42] A.A. Aligia, H. Bonadeo and J. Garces. Phys. Rev. B 43 (1991), 542.

[43] A.A. Aligia. Solid St. Commun. 78 (1991), 739.

[44] A.A. Aligia, J. Garces, and H. Bonadeo. Preprint.

[45] K. Binder and D.W. Heerman: "Monte Carlo simulation in Statistical Physics", Springer Series in Solid-state Sciences. Vol. 80 (Springer Verlag, Berlin 1988).

[46] "Topics in Current Physics 36. Applications of the Monte Carlo Method in Statisical Physics". Ed: K. Binder. Springer-Verlag. New York 1984.

[47] D.R. Cox and H.D. Miller. The theory of stochastic processes. Chapmann and Hall. London 1965.

[48] N. Metropolis, A.W. Rosenbluth, M.N. Rosenbluth, A.H.Teller, E. Teller. J. Chem. Phys. 21 (1953), 1087.

[49] D.P. Landau. Phys. Rev. B 13 (1976), 2997, D.P. Landau. Phys. Rev. B 14 (1976). 255, D.P. Landau. Phys. Rev. B 16 (1977), 4164.

[50] M.E. Fisher, M.N. Barber. Phys. Rev. Lett 28 (1972), 1516.

[51] K. Binder. Z. Phys. B 43 (1981), 119. K. Binder. Phys. Rev. Lett. 47 (1981), 693.

[52] K.W. Kehr, R. Kutner and K. Binder. Phys. Rev. B 23 (1981), 4931. R. Kutner, K. Binder and K.W. Kehr. Phys. Rev. B 26 (1982), 2967.

[53] K. Kawasaki in "Phase Transitions and Critical Phenomena", ed. by C. Domb and M.S. Green, Vol. 2 (Academic. New York 1972) p. 443.

[54] O.G. Mouritsen in "Kinetics of Ordering and Growth at Surfaces", edited by M.G. Lagally (Plenum, New York, 1990). page 1.

[55] J.D. Gunton, M. San Miguel and P.S. Sahni. in Phase Transitions and Critical Phenomena, edited by C. Domb and J L. Lebowitz, Vol. 8 (Academic Press, New York, 1983) p. 267.

[56] I.M. Lifshitz. Sov. Phys. JETP 15 (1962), 939.

[57] S. M. Allen and J.W. Cahn. Acta. Metall. 27 (1979), 1085.

[58] I.M. Lifshitz and V.V. Slyozov. J. Phys. Chem. Solids 19 (1961). 35.

[59] W.W. Mullins and J. Vinals. Acta. Metall. 37 (1989), 991.

[60] A. Sadiq and K. Binder. J. Stat. Physics 35, 5/6 (1984), 517.

[61] C. Roland and M. Grant. Phys Rev. B39 (1989), 11971. D. Huse. Phys Rev. B34 (1986), 7845. J.G. Amar, F.E. Sullivan and R.D. Mountain. Phys Rev. B37 (1988), 196. G.F. Mazenko, O.T. Walls and M. Zannetti. Phys Rev. B38 (1988), 520.

[62] O.G. Mouritsen. Phys. Rev. Lett. 56 (1986). 850.

[63] N.H. Andersen, B. Lebech and H.F. Poulsen, Physica C 172 (1991), 31.

[64] H.F. Poulsen, N. H. Andersen and B. Lebech, Physica C 173 (1991), 387.

[65] G.S. Pawley. J. Appl. Cryst. 13 (1980). 630.

[66] I. Barin and O. Knacke, in: Thermochemical properties of inorganic substances (Springer, Berlin, 1973).

[67] S.J. Rothman, J.Z. Liu, J.W. Downey, L.J. Thompson, Y. Fang, D. Shi, J.E. Baker, J.P. Rice, D.M. Ginsberg, P.D. Han and D.A. Payne, in: Proc. Metall. Soc. Fall Meeting, 1-5 October, 1989, Indianapolis.

[68] E. Salomons and D. de Fontaine. Phys. Rev. B 41 (1990). 11159.

[69] D. Hilton, B. Gorman, P.A. Rikvold, and M.A. Novotny. Preprint.

[70] J. Stephenson. J. Math. Phys. 11 (1970). 420. J. Stephenson. Phys. Rev. B1 (1970). 4405.

[71] P.A. Rikvold, M.A. Novotny, and T. Aukrust. Phys. Rev B43 (1991), 202.

[72] W.R. McKinnon, M.L. Post, L.S. Selwyn, G. Pleizier, J.M. Tarascon, P. Barboux, L.H. Greene, and C.W. Hu[illegible] Rev. B38 (1988), 6543.

[73] I.D. Brown. J. Solid St. Chem. 82 (1989). 122.

[74] Y.J. Uemura et al. Phys. Rev. Lett. 62, 19 (1989). 2317.

[75] S. Rusiecki, B. Bucher, E. Kaldis, E. Jilek, J. Karpinski, C. Rossel, B. Pumpin, H. Keller, W. Kundig, T. Krekels and G. Van Tendeloo. J. Less-Comm. Met. 164-165 (1990). 31.

[76] H. Shaked, J.D. Jorgensen, J. Faber, Jr., D.G. Hinks, and B. Dabrowski. Phys. Rev. B 39 (1989). 7363.

[77] A.G. Khachaturyan and J.W. Morris, Jr. Phys. Rev. Lett. 64 (1989), 76.

[78] J. Als-Nielsen, N.H. Andersen, C. Broholm, K.N. Clausen, B. Lebech, M. Nielsen, and H.F. Poulsen, IEEE Transactions on Magnetics 25 (1989), 2254.

[79] J.V. Andersen, H. Bohr, and O.G. Mouritsen, Phys.Rev. B42 (1990), 283.

[80] Y. Nakazawa and M. Ishikawa. Physica C 158 (1989), 381.

[81] T.B. Lindener, J.F. Hunley, J.E. Gates, A.L. Sutton Jr., J. Brynestaf, and C.R. hubbard. J. Am. Ceram. Soc. 72 (1989), 1775.

[82] E.D. Specht, C.J. Sparks, A.G. Dhere, J. Brynestad, O.B. Cavin, D.M. Kroeger, and H.A. Oye. Phys. Rev. B 37 (1988). 7426.

[83] P. Schleger, W.N Hardy, and B.X. Yang. Physica C 176 (1991), 261.

[84] H. Claus, S. Yang, A.P. Paulikas, J.W. Downey and B.W Veal. Physica C 171 (1990), 205.

[85] N.H. Andersen, L. Borjesson, R.A. Hatfield, B. Lebech, R McGreevy, and J. Wicks. Private communication.

[86] I.D. Brown and D. Altermatt. Acta Cryst. B41 (1985), 244.

[87] J. Fink, J. Pfluger, T. Muller-Heinzerling, N. Nucker, B. Scheerer, H. Romberg, M. Alexander, R. Manzke, T. Buslaps, R. Claessen and M. Skibowski. In: *Earlier and Recent aspects of Superconductivity*, Springer Series in Solid State Sciences 90, ed: J.G. Bednorz and K.A. Muller (Springer Verlag, Berlin, 1990).

[88] L. Jansen and R. Block. Physica C 181 (1991), 149.

[89] A. Furrer. In: Proceedings of ICMAS 1991.

[90] G.-C. Wang and T.-M. Lu. Phys Rev. Lett. 50 (1983), 2014. P.K. Wu, J.H. Perepezko, J.T. McKinney and M.G. Lagally. Phys Rev. Lett. 51 (1983), 1577. M.C. Tringides, P.K. Wu and M.G. Lagally. Phys Rev. Lett. 59 (1987), 315. J.-K. Zuo, G.-C. Wang and T.-M. Lu. Phys Rev. Lett. 60 (1988), 1053. J.-K. Zuo, G.-C. Wang and T.-M. Lu. Phys Rev. B39 (1989), 9432. P.K. Wu, M.C. Tringides, and M.G. Lagally. Phys Rev. B39 (1989), 7595.

[91] T.J. Kistenmacher. Solid St. Comm. 65 (1988), 981.

[92] G. van Tendeloo, private communication.

[93] J.M. Tarascon, P. Barboux, P.F. Miceli, L.H. Greene, G.W. Hull, M. Eibschutz, and S.A. Sunshine. Phys. Rev. B37 (1988), 7458.

[94] T. Kajitani, K. Kusaba, M. Kikuchi, Y. Syono, and M. Hirabayashi. Jpn. J. Appl. Phys. 26 (1987), L1727. P.F. Miceli, J.M. Tarascon, L.H. Greene, P. Barboux, F.J. Rotella, and J.D. Jorgensen. Phys. Rev 37 (1988), 5932. G. Roth, G. Heger, B. Renker, J. Pannetier, V. Caignaert, M. Hervieu, and B. Raveau. Z. Phys B 71 (1988), 43.

[95] T. Tamaki, K.Komai, A.Ito, Y. Maeno, and T. Fujita. Solid St. Comm. 67 (1988), 43. S. Nasu, H. Kitigawa, Y. Oda, T. Kohora, T. Shinjo, K. Assayama, and F.E. Fujita. Physica 148B (1987), 484.

[96] F. Bridges, J.B. Boyce, T. Claeson, T.H. Geballe, and J.M. Tarascon. Phys. Rev. B39 (1989), 11603.

[97] R.J. Cava, B. Batlogg, J.J. Krajewski, I.W. Rupp, Jr., L.F. Schneemeyer, T. Siegrist, R.B. vanDover, P. Marsh, W.W. Peck, Jr., P.K. Gallagher, S.H. Glarum, J.H. Marshall, R.C. Farrow, J.V. Waszczak, R. Hull, and P. Trevor. Nature 336 (1988), 211.

[98] V.A. Kresin, S.A. Wolf, M.E. Reeves and G. Deutscher. In: Proceedings of ICMAS 91.

[99] S.D. Barett, D.J. Durand, C. H. Pennington, C.P. Slichter, T.A. Friedmann, J.P. Rice, and D.M. Ginsberg. Phys. Rev. **B41**, 10 (1990), 6283.

[100] M. Gurvitch, J.M. Valles, Jr., A.M. Cucolo, R.C. Dynes, J.P. Garno, L.F. Schneemeyer, and J.V. Waszczak. Phys. Rev. Lett. **63** (1989), 1008.

[101] C.P. Flynn. "Point Defects and Diffusion". Clarendon Press, Oxford. 1972.

[102] S.J. Rothman and J.L. Routbort. In: Diffusion and Materials. NATO Advanced Study Institute, Series E: Engineering and Materials Science. Edited by G. Brebec, A.L. Laskar, and C. Monty. (Kluwer Academic, Dordrecht, in press).

[103] L.E. Levine and M. Daeumling. Submitted to Phys. Rev. Lett.

[104] H.F. Poulsen, N. H. Andersen, J.V. Andersen, H. Bohr and O.G. Mouritsen, Phys. Rev. Lett. **66** (1991), 465.

[105] H.F. Poulsen, N.H. Andersen, J.V. Andersen, H. Bohr and O.G. Mouritsen, Nature **349** (1991), 594.

[106] H.F. Poulsen, N. H. Andersen, J.V. Andersen, H. Bohr and O.G. Mouritsen, Modern Physics Lett. B **5** (1991), 827.

[107] R.J. Cava, B. Batlogg, C.H. Chen, E.A. Rietman, S.M. Zahurak and D. Werder. Phys. Rev. **36**.10 (1987), 5719.

[108] R.J. Cava, B. Batlogg, K.M. Rabe, E.A. Rietman, P.K. gallagher and L.W. Rupp Jr. Physica C **156** (1988), 523.

**Bibliographic Data Sheet** **Riso R 608(EN)**

Title and author(s)

Oxygen Ordering and Superconductivity in the High $T_c$ Superconductor $YBa_2Cu_3O_{6+x}$

H. F. Poulsen

| ISBN | ISSN |
|---|---|
| 87-550-1787-8 | 0106-2840 |

| Dept. or group | Date |
|---|---|
| Department of Solid State Physics | December 1991 |

| Groups own reg. number(s) | Project/contract No. |
|---|---|
| | |

| Pages | Tables | Illustrations | References |
|---|---|---|---|
| 94 | 5 | 35 | 108 |

Abstract (Max. 2000 char.)

This report contains the result of an experimental and theoretical investigation of the oxygen ordering process in the High $T_c$ superconductor $YBa_2Cu_3O_{6+x}$. For the experimental part, neutron scattering is used in connection with *in situ* monitoring of the oxygen in-diffusion in a gas-volumetric equipment. Information on the variations of the structural phases, the twin domain sizes, the elastic forces, the chemical potential of oxygen as well as diffusion are provided. Using Monte Carlo simulations we find that a simple two-dimensional lattice gas model of the oxygen ordering process, the ASYNNNI model, gives an excellent description of the vast majority of these data. Secondly, a systematic study of the relationship between the static and dynamic variations of the superconducting transition temperature, $T_c$, and the corresponding variations of the low temperature oxygen ordering process is performed. Statistics from Monte Carlo simulations based on the ASYNNNI model are combined with experimental data from the literature. The combined static and dynamic analysis makes it evident that within a charge transfer model, a linear $T_c$ versus charge transfer relationship can only be rationalized if the description is based on extended coherent ordered domains and if the dynamic co-existence between the Ortho-I and the Ortho-II type of domains inherent to the ASYNNNI model is taken into account. A minimal model is proposed, where the total charge transfer is found as a weighted sum over the areas of the Ortho-I and the Ortho-II domains, and the minimal size of the two types of domains are given by a doubling of their unit cells in both directions. Good agreement with the experimental set of data is achieved.

Descriptors INIS/EDB

Computerized Simulation; Copper Oxides; Experimental Data; High-Tc Superconductors; Monte Carlo Method; Neutron Diffraction; Phase Diagrams; Theoretical Data; Thermal Diffusion; Transition Temperatures.

Available on request from:
*Risø Library, Risø National Laboratory (Risø Bibliotek, Forskningscenter Risø)*
P.O. Box 49, DK-4000 Roskilde, Denmark
Phone (+45) 42 37 12 12, ext. 2268/2269 · Telex 43 116 · Telefax (+45) 46 75 56 27

Available on request from:
Risø Library
Risø National Laboratory,
P.O. Box 49, DK-4000 Roskilde, Denmark
Phone +45 42 37 12 12, ext. 2268/2269
Telex 43116, Telefax +45 46 75 56 27

ISBN 87-550-1787-8
ISSN 0106-2840